ELECTRONIC STRUCTURE CALCULATIONS AT MACROSCOPIC SCALES

Thesis by

Vikram Gavini

In Partial Fulfillment of the Requirements

for the Degree of

Doctor of Philosophy

California Institute of Technology

Pasadena, California

2007

(Defended May 2, 2007)

Dedicated to Paul Adrien Maurice Dirac

"The underlying physical laws necessary for the mathematical theory of a large part of physics and the whole of chemistry are completely known, and the difficulty is only that the exact application of these laws leads to equations much too complicated to be soluble. It therefore becomes desirable that approximate practical methods of quantum mechanics should be developed, which can lead to an explanation of the main features of the complex atomic systems without too much computation" – Dirac, P.A.M., 1929

Acknowledgements

I would like to take this opportunity to thank all the people who made my stay at Caltech a memorable and unique experience. First and foremost, my interactions with Prof. Michael Ortiz and Prof. Kaushik Bhattacharya have been an enriching experience. I am very grateful to them for suggesting an exciting problem for my thesis, and advising me on various research and academic issues. They have played a very important role in my growth as a researcher, and I fall short of words to express my gratitude. I hope to make every effort to grow as a researcher, and contribute to the scientific world through research, teaching, and mentoring, which in my opinion is the best way I can thank them.

I want to thank Prof. Guruswami Ravichandran for providing valuable advice over various issues—academic and non-academic—during the last four years, and for serving on my research committee. I have benefitted a great deal from our interactions, and I have always looked up to him for his advice before making important decisions. I am also very grateful to him for providing me the opportunity to gain invaluable teaching experience. I want to thank Prof. Nadia Lapusta for the long, insightful discussions we had in my first year, and her valuable advice over the years. I also want to thank her for kindly agreeing to serve on my thesis committee.

Dr. Jaroslaw Knap played a crucial role in the computational aspects of this work. He not only helped me to get started, but was always available to extend his help and advice in

resolving many computational issues. His advice on many aspects of academic life was very useful. I want to thank Dr. Jaroslaw Knap for his help, advice, support, and for kindly agreeing to serve on my thesis committee.

I want to thank Lydia Saurez, Marta Kahl, and Sylvie Gertmenian for helping me with administrative work, and providing me with all the resources to carry out my research smoothly. I also want to thank Lydia for the wonderful conversations we had on various aspects. I also want to thank Dr. Patrice Hauret for the many interesting discussions on the subject of Functional Analysis, and for verifying the analysis aspects of this work. I also want to thank all the members from my research group for their interaction and support. My special thanks to Alex, Luigi, Phanish, Samantha, Tamer, Thomas, and Yashashree.

I had a great set of friends at Caltech who not only made my transition from undergraduate to graduate life a smooth one, but were also a great source of inspiration. My special thanks to Mandar, Meher, Kaushik Dayal, Sundeep, Swami, and Vaibhav in this regard. My interactions with Abhishek Tiwari, Abhishek Saha, Amrit, Mayank, Pinkesh, Prabha, Shaunak, Subash, Sukhada, Shankar, and Uday will be memorable ones. My special thanks to Nachiket, Sonali, and Tejaswi for the great time I spent with them. I also want to thank my best friends Baskar, Pavithra, and Santi Swaroop for their help and support in various aspects of my life.

Last, but not the least, the support and encouragement I received (and will always receive) from my parents is an important part of my development as a person and a researcher. The blessing from my parents and Nannagaru are a great source of strength. I want to thank my grandparents, my uncles Dinakar and Srinivas, and my aunts Neeraja and Anu for their support.

Abstract

Electronic structure calculations, especially those using density-functional theory have provided many insights into various materials properties in the recent decade. However, the computational complexity associated with electronic structure calculations has restricted these investigations to periodic geometries with small cell-sizes (computational domains) consisting of few atoms ($\sim$ 200 atoms). But material properties are influenced by defects—vacancies, dopants, dislocations, cracks, free surfaces—in small concentrations (parts per million). A complete description of such defects must include both the electronic structure of the core at the fine (sub-nanometer) scale and also elastic and electrostatic interactions at the coarse (micrometer and beyond) scale. This in turn requires electronic structure calculations at macroscopic scales, involving millions of atoms, well beyond the current capability. This thesis presents the development of a *seamless* multi-scale scheme, *Quasi-Continuum Orbital-Free Density-Functional Theory* (QC-OFDFT) to address this significant issue. This multi-scale scheme has enabled for the first time a calculation of the electronic structure of multi-million atom systems using orbital-free density-functional theory, thus, paving the way to an accurate electronic structure study of defects in materials.

The key ideas in the development of QC-OFDFT are (i) a real-space variational formulation of orbital-free density-functional theory, (ii) a nested finite-element discretization of the formulation, and (iii) a systematic means of adaptive coarse-graining retaining full resolution

where necessary, and coarsening elsewhere with no patches, assumptions, or structure. The real-space formulation and the finite-element discretization gives *freedom from periodicity*, which is important in the study of defects in materials. More importantly, the real-space formulation and its finite-element discretization support *unstructured coarse-graining* of the basis functions, which is exploited to advantage in developing the QC-OFDFT method. This method has enabled for the first time a calculation of the electronic structure of samples with millions of atoms subjected to arbitrary boundary conditions. Importantly, the method is completely seamless, does not require any *ad hoc* assumptions, uses orbital-free density-functional theory as its only input, and enables convergence studies of its accuracy. From the viewpoint of mathematical analysis, the convergence of the finite-element approximation is established rigorously using $\Gamma-$convergence, thus adding strength and validity to the formulation.

The accuracy of the proposed multi-scale method under modest computational cost, and the physical insights it offers into properties of materials with defects, have been demonstrated by the study of vacancies in aluminum. One of the important results of this study is the strong cell-size effect observed on the formation energies of vacancies, where cells as large as tens of thousands of atoms were required to obtain convergence. This indicates the prevalence of long-range physics in materials with defects, and the need to calculate the electronic structure of materials at macroscopic scales, thus underscoring the importance of QC-OFDFT.

Finally, QC-OFDFT was used to study a problem of great practical importance: the embrittlement of metals subjected to radiation. The brittle nature of metals exposed to radiation is associated with the formation of prismatic dislocation loops—dislocation loops whose Burgers vector has a component normal to their plane. QC-OFDFT provides an

insight into the mechanism of prismatic dislocation loop nucleation, which has remained unclear to date. This study, for the first time using electronic structure calculations, establishes vacancy clustering as an energetically favorable process. Also, from direct numerical simulations, it is demonstrated that vacancy clusters collapse to form stable prismatic dislocation loops. This establishes vacancy clustering and collapse of these clusters as a possible mechanism for prismatic dislocation loop nucleation. The study also suggests that prismatic loops as small as those formed from a 7-vacancy cluster are stable, thus shedding new light on the nucleation size of these defects which was hitherto unknown.

Contents

List of Figures

List of Tables

Chapter 1

Introduction

Electronic structure calculations (Martin, 2004) have provided great insights into various aspects of materials properties in the last decade. Derived from first-principles (quantum mechanics), electronic structure theories incorporate significant fundamental physics with little empiricism. Therefore, these theories are transferable, and capable of predicting a wide range of properties across various materials and external conditions. Studies on the electronic structure of materials date back to the early 1940s and received a major boost with the development of density-functional theory (Finnis, 2003; Parr & Yang, 1989) in the 1960s. However, the growing computational power has brought these techniques to the forefront in the last decade. Successes of electronic structure calculations include the accurate prediction of phase transformations in a wide range of materials, and insights into the mechanical, electronic, magnetic, and optical properties of materials and compounds.

Despite the success of electronic structure theories, the enormous computational effort involved in these calculations essentially limits these theories to bulk properties of perfect materials. However, defects play a critical role in determining the properties of materials. These include dopants in semi-conductors to dislocations in mechanics to surfaces in nano-structures. These defects occur at very small concentrations and have long-ranged interactions. Therefore a complete and accurate description of such defects must include

the electronic structure of the core of the defect at the fine (sub-nanometer) scale and the elastic, electrostatic, and other effects on the coarse (micrometer and beyond) scale. This in turn requires electronic structure calculations on systems containing millions of atoms, or in other words electronic structure calculations at macroscopic scales. This has remained an open challenge, and is the subject of this thesis.

To be precise, first-principle (quantum mechanics) calculations require a computational effort that grows as N^{3n} for a $n-$electron system. A full quantum mechanical description of a system with just 4 electrons using a space discretization of just 100 points requires the computation of eigenvalues and eigenfunctions of a $100^{12} \times 100^{12}$ matrix, which is intractable. This motivated electronic structure calculations (which are often also referred as *ab intio*), of which density-functional theory (DFT) is the most popular. Though, electronic structure calculations are relatively less expensive than first-principle quantum mechanical calculations, the computational effort involved is large enough to restrict these investigations to small cell-sizes (computational domains) on the order of hundreds of atoms. Thus, the computational domains which are accessible to electronic structure calculations are orders of magnitude smaller than those needed to compute materials properties with defects.

Various multi-scale schemes have been proposed to address this significant challenge, among which upscaling methods (Rappe' et al., 1992; Goddard et al., 2002) and embedding schemes (Fago et al., 2004; Govind et al., 1999; Choly et al., 2005; Lu et al., 2006) are the most popular. Multi-scale schemes where information is transferred from smaller to larger length scales are referred to as upscaling methods. In such methods, electronic structure calculations are used to fit interatomic potentials/force-fields and these potentials are then used to compute materials properties on the macroscopic scale. On the other hand, the philosophy behind embedding schemes is to embed a refined electronic structure calculation

in a coarser molecular dynamic simulation, which in turn is embedded in a continuum theory. Valuable as these schemes are, they suffer from a number of notable shortcomings. In some cases, uncontrolled approximations are made such as the assumption of linear response theory or the Cauchy-Born hypothesis. Others assume separation of scales, the validity of which can not be asserted. Moreover, these schemes are not seamless and are not solely based on a single electronic structure theory. In particular, they introduce undesirable overlaps between regions of the model governed by heterogeneous and mathematically unrelated theories. Finally, no clear notion of convergence to the full electronic structure solution is afforded by the existing methods.

For all the above reasons, there is need for a seamless, multi-scale scheme to perform electronic structure calculations at macroscopic scales with no *ad hoc* assumptions.

This thesis develops a *seamless* coarse-graining scheme that effectively overcomes the present limitations of electronic structure calculations, without the introduction of spurious physics and at no significant loss of accuracy. We refer to the proposed approximation scheme as *Quasi-Continuum Orbital-Free Density-Functional Theory* (QC-OFDFT), and this paves the way to electronic structure calculations at macroscopic scales. The basic building blocks of the scheme are: a real-space formulation of *Orbital-Free Density-Functional Theory* (OFDFT), based on finite-element bases; and a novel quasi-continuum reduction of the resulting equations that resolves detailed information in regions where it is necessary (such as in the immediate vicinity of the defect), but adaptively samples over details where it is not (such as in regions far away from the defect), without significant loss of accuracy. The use of finite-element basis enables consideration of complex geometries, general boundary conditions and locally adapted grids. The quasi-continuum (QC) approach effects a seamless coarse-graining adapted to the local structure of the solution.

The QC reduction proposed here is novel in that it allows for subatomic oscillations in the electron-density and electrostatic potential.

The proposed approximation scheme has the following defining properties: It adapts the level of spatial resolution to the local structure of the solution, e. g., supplying higher resolution near lattice defects and rapidly coarsening the resolution away from the defects; in particular, the coarse-graining is completely unstructured and does not rely on periodicity. Fully-resolved OFDFT and finite lattice-elasticity are obtained as special limits. The coarse-graining is entirely seamless—as opposed to a patchwork of disparate and heterogeneous models—and based solely on approximation theory; in particular, OFDFT is the sole physics input to the calculations, and no spurious physics or *ansatz* regarding the behavior of the system is introduced as a basis for—or as a result of—the coarse-graining. The nature of the systems of interest is such that vast reductions in the size of the problem can be achieved without appreciable loss of accuracy, thus effectively permitting consideration of systems much larger than heretofore possible.

We present examples of electronic structure calculations on multi-million atom systems and show, by a convergence analysis, that the full electron-density field can be obtained everywhere with negligible error and through modest computational means. We also demonstrate through cell-size studies of defect properties in materials, the importance of QC-OFDFT and electronic structure calculations at macroscopic scales. For instance, the mono-vacancy calculations in aluminum have determined scaling relations that are indicative of slow convergence with respect to cell-size. More telling still is the case of di-vacancies. Whereas some di-vacancy systems are found to be repulsive for small cell sizes, in agreement with previous calculations (Carling & Wahnström, 2000; Uesugi et al., 2003), the same di-vacancy systems are found to be attractive for larger cell-sizes, in keeping with experi-

mental observation (Ehrhart et al., 1991; Hehenkamp, 1994). Thus, in this case access to large cell sizes changes the predicted physics not only *quantitatively* but also *qualitatively.*

Furthermore, as an application of the theory, we study the problem of radiation damage in aluminum. Exposure to radiation leads to a rapid deterioration of the fracture toughness in metals, and thus is a problem of great practical significance. This loss of fracture toughness is associated with an increase in the density of prismatic dislocation loops—dislocation loops with an out-of-plane component of Burgers vector—which are experimentally observed to arise as the irradiation dose increases (Masters, 1965; Eyre & Bartlett, 1965, 1973; Bullough et al., 1991; Kawanishi & Kuramoto, 1986; Horton & Farrell, 1984). The mechanism through which these prismatic dislocation loops nucleate has remained unclear to date and is a problem of active research.

QC-OFDFT has provided new insights into the phenomenon of vacancy clustering in aluminum, and the mechanism of prismatic dislocation loop nucleation. We show for the first time using electronic structure calculations that vacancy clustering is an energetically favorable process. Moreover, through direct numerical simulations we observed that these vacancy clusters collapse to form stable prismatic loops. These results suggest that vacancies conglomerate to form vacancy clusters, which then collapse leaving behind a prismatic dislocation loop. The results presented in this work are the first numerical confirmation, using electronic structure calculations, of this mechanism of prismatic dislocation loop nucleation. Also, we show that prismatic loops as small as those formed from 7-vacancy clusters are stable, thus shedding new light on the nucleation size of these defects which was hitherto unknown.

The thesis is organized as follows. Chapter 2 provides a brief overview of the electronic structure theories. Chapter 3 describes the real-space finite-element formulation of orbital-

free density-functional theory. Chapter 4 describes existence results for the real-space formulation of OFDFT, and provides rigorous proofs of convergence for the finite-element discretization of the formulation using the mathematical technique of $\Gamma-$convergence. Chapter 5 develops the quasi-continuum orbital-free density-functional theory. This chapter describes the key ideas of quasi-continuum reduction, and demonstrates the accuracy and importance of QC-OFDFT through studies on a mono-vacancy in aluminum. Chapter 6 reports studies on the phenomenon of vacancy clustering in aluminum, and the mechanism of prismatic dislocation loop nucleation. Finally, we conclude in Chapter 7 with a short discussion and consider the scope for future work.

Chapter 2

Overview of electronic structure theories

A first-principle computation of materials properties using quantum mechanics under the Born-Oppenheimer approximation (Finnis, 2003) involves the estimation of the electronic wave-functions by solving the time-independent Schrödinger's equation. This is an eigenvalue problem given by

$$H\psi_i = \epsilon_i \psi_i \,, \tag{2.1a}$$

$$H = \sum_{i=1}^{N} -\frac{1}{2}{\nabla_i}^2 + \frac{1}{2}\sum_{i=1}^{N}\sum_{\substack{j=1 \\ j\neq i}}^{N} \frac{1}{|\mathbf{r}_i - \mathbf{r}_j|} + \sum_{i=1}^{N}\sum_{I=1}^{M} \frac{-Z_I}{|\mathbf{r}_i - \mathbf{R}_I|} \,, \tag{2.1b}$$

$$\psi = \psi(\mathbf{x}_1, \mathbf{x}_2, ...\mathbf{x}_N) \,, \tag{2.1c}$$

where H is the Hamiltonian of the system which is comprised of the kinetic energy of electrons and electrostatic interaction energy between electrons and nuclei; ψ_i denote normalized, anti-symmetric electronic wave-functions, i.e., eigenfunctions of the Hamiltonian; and ϵ_i denote the energy levels or eigenvalues of the Hamiltonian. Here, $\mathbf{x}_i = (\mathbf{r}_i, s_i)$, $\mathbf{r}_i \in \mathbb{R}^3$ denotes the spatial coordinates and s_i the spin of the i^{th} electron in the system; $\mathbf{R}_I \in \mathbb{R}^3$ represent the nuclear positions of the I^{th} nuclei in the system with a charge of Z_I; and N

and M denote the total number of electrons and nuclei in the system.

Equation (2.1) suggests that the electronic wave-functions belong to a $3N$ dimensional space, i.e, $\psi \in \mathbb{R}^{3N}$. This translates into a computational complexity that is so huge, that it makes the computation of materials properties using quantum mechanics infeasible. To get an order of magnitude estimate of this complexity, consider a material system with 100 electrons and consider a discretization of the real line, $\mathbb{R}$, with just 100 points. A first-principle calculation of this system, which involves solving the eigenvalue problem given by equation (2.1), requires the computation of eigenvalues and eigenfunctions of an astronomical $100^{300} \times 100^{300}$ matrix. This problem is computationally intractable. In a landmark paper in 1929 (Dirac, 1929), Paul Dirac had remarked that "The underlying physical laws necessary for the mathematical theory of a large part of physics and the whole of chemistry are completely known, and the difficulty is only that the exact application of these laws leads to equations much too complicated to be soluble. It therefore becomes desirable that approximate practical methods of quantum mechanics should be developed, which can lead to an explanation of the main features of the complex atomic systems without too much computation". These various approximate methods developed over more than 5 decades constitute the theories of electronic structure. The most popular among them are the Hartree-Fock method and density-functional theory, which are discussed below.

2.1 Hartree-Fock method

The Hartree-Fock method (Szabo & Ostlund, 1982) results from approximating the electronic wave-function with a Slater determinant, which respects the anti-symmetric nature of the electronic wave-function. This approximation is given by,

$$\psi(\mathbf{x}_1, \mathbf{x}_2, ...\mathbf{x}_N) = det \begin{pmatrix} \psi_1(\mathbf{x}_1) & \psi_1(\mathbf{x}_2) & ... & \psi_1(\mathbf{x}_n) \\ \psi_2(\mathbf{x}_1) & \psi_2(\mathbf{x}_2) & ... & \psi_2(\mathbf{x}_n) \\ . & . & . & . \\ . & . & . & . \\ \psi_n(\mathbf{x}_1) & \psi_n(\mathbf{x}_2) & ... & \psi_n(\mathbf{x}_n) \end{pmatrix}.$$

This approximation reduces a wave-function in $3N$ dimensional space to N wave-functions in 3 dimensional space which are computationally tractable. The approximation of the electronic wave-function by a Slater determinant is equivalent to the assumption that the electrons in the system interact with each other only through a mean field, thus effectively ignoring the electron correlations.

The ground-state energy of a material system computed from the Hartree-Fock method provides an upper bound to the actual ground-state energy of the system. In this regard, the Hartree-Fock method has a useful variational structure associated with it. Exploiting this variational structure, the Hartree-Fock method is extended to obtain a more refined electronic structure theory, which is described by multi-configuration equations. Multi-configuration equations are a generalization of the Hartree-Fock method, where a linear combination of a number of Slater determinants is used to approximate the wave-function, as against a single Slater determinant in the case of Hartree-Fock approximation. It can be shown that as the basis of the single electron wave functions is increased to span the complete Hilbert space, the multi-configuration equations reproduce the exact quantum mechanical equations (Friesecke, 2003; Lewin, 2004).

Though the Hartree-Fock approach has been used quite extensively, over the course of last

few decades the density-functional theory (DFT) of Hohenberg, Kohn, and Sham (Parr & Yang, 1989; Finnis, 2003), which expresses the ground-state energy of the material system in terms of the electron-density, has gained popularity for its accuracy, reliability, and feasibility of electronic structure calculations on a wide range of materials.

2.2 Density-functional theory

Density-functional theory provides us with a framework to reformulate the problem of solving the Schrödinger's equation of a N-electron system into a problem of estimating the wave-functions and corresponding energies of an effective single-electron system. Density-functional theory is based on a variational formulation, and is therefore very suitable for ground-state calculations, though extensions to excited states are possible (Parr & Yang, 1989). The heart of density-functional theory lies in the work by Hohenberg, Kohn, and Sham (Hohenberg & Kohn, 1964; Kohn & Sham, 1965) who prove that "*electron-density* as a basic variable is sufficient to describe the properties of a material system in its ground state". This is a remarkable and powerful statement, as it reduces the problem of solving for a quantity (electronic wave-function) in $3N$ dimensional space to solving for a quantity (electron-density) in 3 dimensional space. This very statement has revolutionized electronic structure calculations, and has put density-functional theory in the forefront of electronic structure theories. The fact that the ground-state properties of materials depend only on electron-density is not difficult to verify. We start from a variational statement: The energy of any system is always greater than or equal to its ground-state energy. Denoting the ground-state energy by E_0,

$$\langle \psi | H | \psi \rangle \geq E_0 \,. \tag{2.2}$$

Combining equations (2.2) and (2.1), and representing the kinetic energy of electrons by T and the interaction between nuclei and electrons by $V_{ext}(\mathbf{r}_i)$, the variational statement reads as

$$\langle\psi|T + \frac{1}{2}\sum_{i=1}^{N}\sum_{\substack{j=1\\j\neq i}}^{N}\frac{1}{|\mathbf{r}_i - \mathbf{r}_j|} + \sum_{i=1}^{N} V_{ext}(\mathbf{r}_i)|\psi\rangle \geq E_0\,. \tag{2.3}$$

As $\psi(\mathbf{x}_1, \mathbf{x}_2, ...\mathbf{x}_N)$ is normalized, the electron-density or the probability density of finding any of the N electrons with arbitrary spin is given by,

$$\rho(\mathbf{r}_1) = N\int ...\int |\psi(\mathbf{x}_1, \mathbf{x}_2, ...\mathbf{x}_N)|^2 ds_1 d\mathbf{x}_2..d\mathbf{x}_N\,. \tag{2.4}$$

Combining equations (2.2) and (2.4), and noting that $V_{ext}(\mathbf{r}_i)$ is a local operator, we get

$$\langle\psi|T + \frac{1}{2}\sum_{i=1}^{N}\sum_{\substack{j=1\\j\neq i}}^{N}\frac{1}{|\mathbf{r}_i - \mathbf{r}_j|}|\psi\rangle + \int \rho(\mathbf{r})V_{ext}(\mathbf{r})d\mathbf{r} \geq E_0\,. \tag{2.5}$$

The last term in equation (2.5), which is the interaction of the external field with the electrons in the system, is independent of the electronic wave-function and depends only on the electron-density. However, the first term, which includes the kinetic energy of electrons and the electron-electron interactions, depends on the wave-function. This dependence is dropped by defining a new functional $F(\rho)$, given by

$$F(\rho) = \min_{\psi\to\rho}\langle\psi|T + \frac{1}{2}\sum_{i=1}^{N}\sum_{\substack{j=1\\j\neq i}}^{N}\frac{1}{|\mathbf{r}_i - \mathbf{r}_j|}|\psi\rangle\,, \tag{2.6}$$

where $\psi \to \rho$ denotes the minimization over all possible antisymmetric ψ which give rise to a particular ρ. Thus the ground-state energy, and consequently the ground-state materials

properties depend only on the electron-density. The ground-state energy is given by

$$E(\rho) = F(\rho) + \int \rho(\mathbf{r}) V_{ext}(\mathbf{r}) d\mathbf{r} + \frac{1}{2} \sum_{I=1}^{M} \sum_{\substack{J=1 \\ J \neq I}}^{M} \frac{Z_I Z_J}{|\mathbf{R}_I - \mathbf{R}_J|}\,, \tag{2.7}$$

where the last term in equation (2.7) is the electrostatic repulsive energy between the nuclei.

Though it has been established that ground-state material properties depend only on electron-density, the explicit functional form of $F(\rho)$ defined in equation (2.6) is not known. Density-functional theory is exact in principle, but the exact evaluation of $F(\rho)$ is tantamount to solving the Schrödinger's equation. Hence, the functional $F(\rho)$ is evaluated approximately. An important step in this direction was taken by Kohn and Sham (Kohn & Sham, 1965) by using the properties of a reference system of non-interacting electrons with density ρ to write

$$F(\rho) = T_s(\rho) + E_H(\rho) + E_{xc}(\rho)\,, \tag{2.8}$$

where T_s is the kinetic energy of non-interacting electrons, E_H is the classical electrostatic interaction energy (also referred to as Hartree energy), and E_{xc} denotes the exchange and correlation energy. Though the exact form of E_{xc} is not known, good approximations of the exchange and correlation functionals are available using local density approximations (LDA) and generalized gradient approximations (GGA) (Koch & Holthausen, 2001; Ceperley & Alder, 1980; Perdew & Zunger, 1981). In the Kohn-Sham scheme of things (KS-DFT), $T_s(\rho)$ is computed in an indirect approach by observing that the the Euler-Lagrange equations corresponding to $E(\rho)$ under the constraint $\int \rho(\mathbf{r}) d\mathbf{r} = N$ are identical to that of a single-electron Schrödinger's equation in an effective mean-field. However, in this scheme of things,

one would have to go through the computationally intensive calculation of estimating the single-electron wave-functions in a self-consistent manner. This poses a serious limitation in the attempt to solve systems of larger size and complexity. This limitation has inspired studies on orbital-free forms of kinetic energy functionals, where $T_s(\rho)$ is modelled.

Numerous efforts have been made to come up with explicit forms of $T_s(\rho)$ without the need to compute electronic wave functions; these are called *orbital-free* kinetic energy functionals. The version of density-functional theory where $T_s(\rho)$ is modelled using orbital-free kinetic energy functionals is commonly referred to as *Orbital-Free Density-Functional Theory* (OFDFT). The earliest of the works in this direction date back to the Thomas-Fermi model proposed in 1927 (Thomas, 1927; Fermi, 1927). Thomas and Fermi derived an explicit representation of the kinetic energy using a local density approximation. The Thomas-Fermi model approximates the kinetic energy of a system of non-interacting electrons with that of a homogeneous electron gas and is given by

$$T_s(\rho) = C_F \int \rho^{5/3}(\mathbf{r}) d\mathbf{r}\,, \tag{2.9}$$

where $C_F = \frac{3}{10}(3\pi^2)^{2/3}$. A major setback to the Thomas-Fermi approach was the Teller non-bonding theorem for this class of functionals (Parr & Yang, 1989), which showed that the Thomas-Fermi model does not predict binding in materials. This deficiency was corrected by including in the kinetic energy functionals a term depending on the gradient of the electron density. This correction led to a family of kinetic energy functionals called the Thomas-Fermi-Weizsacker functionals (Parr & Yang, 1989), which are given by the expression

$$T_s(\rho) = C_F \int \rho^{5/3}(\mathbf{r}) d\mathbf{r} + \frac{\lambda}{8} \int \frac{|\nabla\rho(\mathbf{r})|^2}{\rho(\mathbf{r})} d\mathbf{r}\,, \tag{2.10}$$

where λ is a parameter. Different values of λ are found to work better in different cases (Parr & Yang, 1989); $\lambda = 1$ and $\lambda = 1/9$ are the most commonly used values. There have been considerable efforts (Wang et al., 1998, 1999; Choly & Kaxiras, 2002; Smargiassi & Madden, 1994; Wang & Teter, 1992) to improve these orbital-free kinetic energy functionals by introducing an additional non-local term called the kernel energy. These kinetic energy functionals have a functional form given by

$$T_s(\rho) = C_F \int \rho^{5/3}(\mathbf{r}) d\mathbf{r} + \frac{1}{8} \int \frac{|\nabla \rho(\mathbf{r})|^2}{\rho(\mathbf{r})} d\mathbf{r} + \int \int f(\rho(\mathbf{r})) K(|\mathbf{r} - \mathbf{r}'|) g(\rho(\mathbf{r}')) d\mathbf{r} d\mathbf{r}', \quad (2.11)$$

where f, g, and K are chosen to satisfy known limits of exact $T_s(\rho)$, and such that the total kinetic energy functional exhibits correct linear response.

In the present work, we restrict ourselves to the Thomas-Fermi-Weizsacker functionals for the purpose of demonstration, and would like to remark that the theory developed in this thesis can be extended to include the non-local kernel energies by solving a Helmholtz equation, as suggested by Choly & Kaxiras (2002). In the limit of slowly varying electron densities and rapidly varying electron densities, the more sophisticated kinetic energy functionals with kernel energy are found to reduce to the Thomas-Fermi-Weizsacker family of functionals. Thus, the Thomas-Fermi-Weizsacker kinetic energy functionals are good models for systems whose electronic structure is close to that of a free electron gas, namely, aluminum and simple metals.

Chapter 3

Real-space finite-element formulation of orbital-free density-functional theory

Traditionally, density-functional theory calculations have been performed in Fourier-space using plane-wave basis functions (Finnis, 2003). The choice of a plane-wave basis for electronic structure calculations has been the most popular one, as it lends itself to a computation of the electrostatic interactions naturally using Fourier transforms. However, the plane-wave basis has some very notable disadvantages: Most importantly, it requires periodic boundary conditions and this is not appropriate for various problems of interest in materials science, especially defects. Second, a plane-wave basis requires the evaluation of Fourier transforms which affect the scalability of parallel computation. Third, the plane-wave basis functions are non-local in the real space, thus resulting in a dense matrix which limits the effectiveness of iterative solutions; this in turn makes it very tricky to use these calculations in multi-scale approaches, which often use real-space formulations to deal with realistic boundary conditions. Although plane-wave basis has been the preferred choice in this area, recently there have been efforts at performing density-functional calculations using a finite-element basis in a periodic setting (Pask et al., 1999). Other real-space approaches include GAUSSIAN (Hehre et al., 1969), FPLMTO (Wills & Cooper, 1987), SIESTA (Soler

et al., 2002), ONETEP (Skylaris et al., 2005), and CONQUEST (Bowler et al., 2006) based on specific orbital ansatz or tight-binding.

In this chapter, a real-space formulation for orbital-free density-functional theory is presented and a finite-element method for computing this formulation is developed. Here, the treatment is confined to the Thomas-Fermi-Weizsacker family of kinetic energy functionals (Parr & Yang, 1989; Thomas, 1927; Fermi, 1927) for clarity; however, we show in the Appendix how the present approach can be extended to the more recent and accurate kernel kinetic energy functionals (Wang et al., 1998, 1999; Smargiassi & Madden, 1994; Wang & Teter, 1992).

An important difficulty in using a real-space formulation is that electrostatic interactions are extended in real-space. To this end, we reformulate the electrostatics as a local variational principle. This converts the problem of computing the ground state energy to a saddle-point variational problem with a local functional in real-space. We show that this problem is mathematically well-posed by proving existence of solutions in a subsequent chapter.

Since our formulation is local and variational, it is natural to discretize it using the finite-element method. In doing so, we exploit an advantage of the saddle-point formulation and use the same mesh to resolve both the electron-density and the electrostatic potential. The convergence of the finite-element discretization is rigorously established using the mathematical technique of $\Gamma-$convergence in Chapter 4.

Numerical implementation of the formulation requires care, since the electron densities and electrostatic potential are localized near the atomic cores and are convected as the atomic positions change. Consequently, a fixed spatial mesh would be extremely inefficient as we alternate between relaxing the electron-density and atomic positions. Therefore, we

design a mesh which convects with the atomic position and obtain efficient convergence.

Further, the approach is demonstrated using three sets of examples: The first set of examples are atoms. We begin with a hydrogen atom for which an analytic solution of Schrödinger's equation is known, but also consider other, heavier atoms. The second set of examples are nitrogen and carbon-monoxide molecules, for which there are numerous careful calculations. Our results show reasonable agreement for binding energies with experiments and other calculations; however the computed bond lengths are rather poor. These errors are the well-recognized consequence of the use of orbital-free kinetic energy functionals in these covalent dimers, rather than our formulation and numerical method. The third set of examples is a series of aluminum clusters ranging from 1 unit (face-centered-cubic) cell to $9 \times 9 \times 9$ unit cells (3730 atoms), and these demonstrate the efficacy and advantages of our approach. First, being clusters, they possess no natural periodicity and thus are not amenable to plane-wave basis. Second, since the boundaries of the clusters satisfy physically meaningful boundary conditions, it is possible to extract information regarding the scaling of the ground-state energy with size. Third, the finite-element method allows one to use unstructured discretization, concentrating numerical effort in regions where and only where it is necessary with ease and little loss of accuracy. Further, it allows us to adapt the discretization to each atomic position.

The remainder of the chapter is organized as follows. Section 3.1 describes the real-space variational formulation of orbital-free density-functional theory. Section 3.2 describes the finite-element discretization of the formulation. Section 3.3 describes the details of numerical implementation and Section 3.4 the examples. Section 3.5 summarizes the chapter with a short discussion.

3.1 Formulation

The ground state energy in density-functional theory is given by (cf, e. g., Finnis (2003); Parr & Yang (1989))

$$E(\rho, \mathbf{R}) = T_s(\rho) + E_{xc}(\rho) + E_H(\rho) + E_{ext}(\rho, \mathbf{R}) + E_{zz}(\mathbf{R}), \tag{3.1}$$

where ρ is the electron-density, $\mathbf{R} = \{\mathbf{R}_1, \ldots, \mathbf{R}_M\}$ collects the nuclear positions in the system, and the different terms are explained presently.

T_s is the kinetic energy of non-interacting electrons. A common choice of this in orbital-free density-functional theory is the Thomas-Fermi-Weizsacker family of functionals (Parr & Yang, 1989), which have the form

$$T_s(\rho) = C_F \int_\Omega \rho^{5/3}(\mathbf{r}) d\mathbf{r} + \frac{\lambda}{8} \int_\Omega \frac{|\nabla \rho(\mathbf{r})|^2}{\rho(\mathbf{r})} d\mathbf{r}, \tag{3.2}$$

where $C_F = \frac{3}{10}(3\pi^2)^{2/3}$, λ is a parameter, and Ω contains the support of ρ (crudely the region where ρ is non-zero). Different values of λ are found to work better in different cases (Parr & Yang, 1989). $\lambda = 1$ is the Weizsacker correction and is suitable for rapidly varying electron densities, $\lambda = 1/9$ gives the conventional gradient approximation and is suitable for slowly varying electron densities, $\lambda = 1/6$ effectively includes the 4th-order effects, and $\lambda = 0.186$ was determined from analysis of large atomic-number limit of atoms. This class of functionals makes computations of large and complex systems tractable, though it does have limitations and improvements have been proposed (Wang et al., 1998, 1999; Smargiassi & Madden, 1994; Wang & Teter, 1992). We confine our attention to the Thomas-Fermi-Weizsacker family of functionals (3.2) for now for clarity. However, we explain in the

Appendix that our approach can be extended to include the improved functionals.

E_{xc} is the exchange-correlation energy. We use the Local Density Approximation (LDA) (Ceperley & Alder, 1980; Perdew & Zunger, 1981) given by

$$E_{xc}(\rho) = \int_{\Omega} \epsilon_{xc}(\rho(\mathbf{r}))\rho(\mathbf{r})d\mathbf{r}, \tag{3.3}$$

where $\epsilon_{xc} = \epsilon_x + \epsilon_c$ is the exchange and correlation energy per electron given by,

$$\epsilon_x(\rho) = -\frac{3}{4}(\frac{3}{\pi})^{1/3}\rho^{1/3} \tag{3.4}$$

$$\epsilon_c(\rho) = \begin{cases} \frac{\gamma}{1+\beta_1\sqrt{r_s}+\beta_2 r_s} & r_s \geq 1 \\ A\log r_s + B + Cr_s\log r_s + Dr_s & r_s < 1 \end{cases} \tag{3.5}$$

where $r_s = (\frac{3}{4\pi\rho})^{1/3}$. The values of the constants are different depending on whether the medium is polarized or unpolarized. The values of the constants are: $\gamma_u = -0.1471$, $\beta_{1u} = 1.1581$, $\beta_{2u} = 0.3446$, $A_u = 0.0311$, $B_u = -0.048$, $C_u = 0.0014$, $D_u = -0.0108$, $\gamma_p = -0.079$, $\beta_{1p} = 1.2520$, $\beta_{2p} = 0.2567$, $A_p = 0.01555$, $B_p = -0.0269$, $C_p = 0.0001$, $D_p = -0.0046$.

The last three terms in the functional (3.1) are electrostatic:

$$E_H(\rho) = \frac{1}{2}\int_{\Omega}\int_{\Omega} \frac{\rho(\mathbf{r})\rho(\mathbf{r}')}{|\mathbf{r}-\mathbf{r}'|}d\mathbf{r}d\mathbf{r}', \tag{3.6}$$

$$E_{ext}(\rho, \mathbf{R}) = \int_{\Omega} \rho(\mathbf{r})V_{ext}(\mathbf{r})d\mathbf{r}, \tag{3.7}$$

$$E_{zz}(\mathbf{R}) = \frac{1}{2}\sum_{I=1}^{M}\sum_{\substack{J=1 \\ J\neq I}}^{M} \frac{Z_I Z_J}{|\mathbf{R}_I - \mathbf{R}_J|}. \tag{3.8}$$

E_H is the classical electrostatic interaction energy of the electron-density, also referred to as

Hartree energy; E_{ext} is the interaction energy with external field, V_{ext}, induced by nuclear charges; and E_{zz} denotes the repulsive energy between nuclei.

The energy functional (3.1) is local except for two terms: the electrostatic interaction energy of the electrons and the repulsive energy of the nuclei. For this reason, evaluation of the electrostatic interaction energy is the most computationally intensive part of the calculation of the energy functional. Therefore, we seek to write it in a local form. To this end, we first regularize the point nuclear charge Z_I at $\mathbf{R}_I$ with a smooth function $Z_I\delta_{\mathbf{R}_I}(\mathbf{r})$, which has support in a small ball around $\mathbf{R}_I$ and total charge Z_I. We then rewrite the electrostatic nuclear energy as

$$E_{zz}(\mathbf{R}) = \frac{1}{2}\int_\Omega\int_\Omega \frac{b(\mathbf{r})b(\mathbf{r}')}{|\mathbf{r}-\mathbf{r}'|}d\mathbf{r}d\mathbf{r}', \tag{3.9}$$

where $b(\mathbf{r}) = \sum_{I=1}^M Z_I\delta_{\mathbf{R}_I}(\mathbf{r})$. Notice that this differs from the earlier formulation by the self-energy of the nuclei, but this is an inconsequential constant depending only on the nuclear charges. Second, we replace the direct Coulomb formula for evaluating the electrostatic energies with the following identity:

$$\begin{aligned}&\frac{1}{2}\int_\Omega\int_\Omega \frac{\rho(\mathbf{r})\rho(\mathbf{r}')}{|\mathbf{r}-\mathbf{r}'|}d\mathbf{r}d\mathbf{r}' + \int_\Omega \rho(\mathbf{r})V_{ext}(\mathbf{r})d\mathbf{r} + \frac{1}{2}\int_\Omega\int_\Omega \frac{b(\mathbf{r})b(\mathbf{r}')}{|\mathbf{r}-\mathbf{r}'|}d\mathbf{r}d\mathbf{r}' \\ &= -\inf_{\phi\in H^1(\mathbb{R}^3)}\left\{\frac{1}{8\pi}\int_{\mathbb{R}^3}|\nabla\phi(\mathbf{r})|^2d\mathbf{r} - \int_{\mathbb{R}^3}(\rho(\mathbf{r})+b(\mathbf{r}))\phi(\mathbf{r})d\mathbf{r}\right\}\end{aligned} \tag{3.10}$$

where we assume that $\rho \in H^{-1}(\mathbb{R}^3)$. Briefly, note that the Euler-Lagrange equation associated with the variational problem above is

$$\frac{-1}{4\pi}\Delta\phi = \rho + b. \tag{3.11}$$

These have an unique solution:

$$\phi(\mathbf{r}) = \int_\Omega \frac{\rho(\mathbf{r}')}{|\mathbf{r}-\mathbf{r}'|}d\mathbf{r}' + \int_\Omega \frac{b(\mathbf{r}')}{|\mathbf{r}-\mathbf{r}'|}d\mathbf{r}' = \int_\Omega \frac{\rho(\mathbf{r}')}{|\mathbf{r}-\mathbf{r}'|}d\mathbf{r}' + V_{ext}. \tag{3.12}$$

Substituting this into the variational problem and integrating by parts gives us the desired identity.

This identity (3.10) allows us to write the energy functional in the local form,

$$E(\rho, \mathbf{R}) = \sup_{\phi \in H^1(\mathbb{R}^3)} L(\rho, \mathbf{R}, \phi) \tag{3.13}$$

where we introduce the Lagrangian

$$\begin{aligned} L(\rho, \mathbf{R}, \phi) = C_F \int_\Omega \rho^{5/3}(\mathbf{r})d\mathbf{r} + \frac{\lambda}{8}\int_\Omega \frac{|\nabla\rho(\mathbf{r})|^2}{\rho(\mathbf{r})}d\mathbf{r} + \int_\Omega \epsilon_{xc}(\rho(\mathbf{r}))\rho(\mathbf{r})d\mathbf{r} \\ - \frac{1}{8\pi}\int_{\mathbb{R}^3} |\nabla\phi(\mathbf{r})|^2 d\mathbf{r} + \int_{\mathbb{R}^3} (\rho(\mathbf{r}) + b(\mathbf{r}))\phi(\mathbf{r})d\mathbf{r}. \end{aligned} \tag{3.14}$$

The problem of determining the ground-state electron-density and the equilibrium positions of the nuclei can now be expressed as the minimum problem

$$\inf_{\rho \in Y,\ \mathbf{R}\in\mathbb{R}^{3M}} E(\rho, \mathbf{R}) \tag{3.15a}$$

$$\text{subject to:} \qquad \rho(\mathbf{r}) \geq 0 \tag{3.15b}$$

$$\int_\Omega \rho(\mathbf{r})d\mathbf{r} = N, \tag{3.15c}$$

where N is the number of electrons in the system and Y is an appropriate space of electron-

densities. Equivalently, the problem can be formulated in the saddle-point form

$$\inf_{\rho\in Y,\ \mathbf{R}\in\mathbb{R}^{3M}} \sup_{\phi\in H^1(\mathbb{R}^3)} L(\rho,\mathbf{R},\phi) \tag{3.16a}$$

$$\text{subject to:} \qquad \rho(\mathbf{r}) \geq 0 \tag{3.16b}$$

$$\int_\Omega \rho(\mathbf{r})d\mathbf{r} = N. \tag{3.16c}$$

The constraint of $\rho \geq 0$ can be imposed by making the substitution

$$\rho = u^2, \tag{3.17}$$

which results in the Lagrangian

$$\begin{aligned} L(u,\mathbf{R},\phi) = C_F \int_\Omega u^{10/3}(\mathbf{r})d\mathbf{r} + \frac{\lambda}{2}\int_\Omega |\nabla u(\mathbf{r})|^2 d\mathbf{r} + \int_\Omega \varepsilon_{xc}(u^2(\mathbf{r}))u^2(\mathbf{r})d\mathbf{r} \\ - \frac{1}{8\pi}\int_{\mathbb{R}^3} |\nabla\phi(\mathbf{r})|^2 d\mathbf{r} + \int_{\mathbb{R}^3} (u^2(\mathbf{r}) + b(\mathbf{r}))\phi(\mathbf{r})d\mathbf{r} \end{aligned} \tag{3.18}$$

and the energy

$$E(u,\mathbf{R}) = \sup_{\phi\in H^1(\mathbb{R}^3)} L(u,\mathbf{R},\phi). \tag{3.19}$$

With this representation, the minimum problem (3.15) becomes

$$\inf_{u\in X,\ \mathbf{R}\in\mathbb{R}^{3M}} E(u,\mathbf{R}) \tag{3.20a}$$

$$\text{subject to:} \qquad \int_\Omega u^2(\mathbf{r})d\mathbf{r} = N, \tag{3.20b}$$

and the saddle-point problem (3.16) becomes

$$\inf_{u\in X,\ \mathbf{R}\in\mathbb{R}^{3M}} \sup_{\phi\in H^1(\mathbb{R}^3)} L(u,\mathbf{R},\phi) \tag{3.21a}$$

$$\text{subject to:} \qquad \int_\Omega u^2(\mathbf{r})d\mathbf{r} = N, \tag{3.21b}$$

where X is a suitable space of solutions for the square-root electron-density, which will be made explicit in Chapter 4. The preceding *local* variational characterization of the ground-state electronic structure constitutes the basis of the finite-element approximation schemes described subsequently.

3.2 Finite-element approximation

We recall that finite-element bases are piecewise polynomial and are constructed from a representation of the domain of analysis as a cell complex, or *triangulation*, T_h (cf, e.g., Ciarlet (2002); Brenner & Scott (2002)). Often, the triangulation is chosen to be simplicial as a matter of convenience, but other types of cells, or *elements*, can be considered as well. Here and subsequently, h denotes the size of the triangulation, e. g., the largest circumdiameter of all of its faces. A basis–or *shape*–function is associated to every vertex–or *node*–of the triangulation. The shape functions are normalized to take the value 1 at the corresponding node and 0 at all remaining nodes. The support of each shape function extends to the simplices incident on the corresponding node, which confers the basis a local character. In order to ensure convergence as $h \to 0$, finite-element shape functions are also required to be continuous across all faces of the triangulation and to represent affine functions exactly. The interpolated fields $U^h(\mathbf{r})$ spanned by a finite-element basis are of the

form

$$U^h(\mathbf{r}) = \sum_i U_i N_i^h(\mathbf{r})\,, \tag{3.22}$$

where i indexes the nodes of the triangulation, $N_i^h(\mathbf{r})$ denotes the shape function corresponding to node i, and U_i is the value of $U^h(\mathbf{r})$ at node i.

We shall denote by X_h the finite-dimensional linear subspace of X of functions of the form (3.22), i. e., the *span* of the shape functions $N_i^h(\mathbf{r})$. In problems governed by a minimum principle, the Rayleigh-Ritz or *best approximation* corresponding to a given discretization is obtained by effecting a constrained minimization over X_h. This constrained minimization reduces the problem to the solution of a finite-dimensional system of—generally non-linear—algebraic equations and generates a sequence of approximations $U^h(\mathbf{r})$ indexed by the mesh size h. A central problem of approximation theory is to ascertain whether the energy of the sequence $U^h(\mathbf{r})$ converges the ground-state energy of the system as $h \to 0$ and, if the problem admits solutions, whether the sequence $U^h(\mathbf{r})$ itself converges to a ground-state of the system. In view of (3.20) and (3.21), in the present setting the constrained problem takes the form

$$\inf_{u^h \in X_h,\ \mathbf{R}\in\mathbb{R}^{3M}} E(u^h, \mathbf{R})\,, \tag{3.23a}$$

$$\text{subject to:} \qquad \int_\Omega (u^h(\mathbf{r}))^2 d\mathbf{r} = N \tag{3.23b}$$

$$E(u^h, \mathbf{R}) = \sup_{\phi^h \in X_h} L(u^h, \mathbf{R}, \phi^h) \tag{3.23c}$$

A full account of finite-element discretization with rigorous proofs of the convergence of the approximations is presented in Chapter 4.

3.3 Numerical implementation

We now turn to a numerical implementation of the variational formulation (3.21) described in Section 3.1. We discretize the variational problem using a finite-element method and use a nested sequence of iterative conjugate-gradient solvers to solve for the electrostatic potential, electron-density, and atomic positions. For a given set of atomic positions, we relax the electron-density, and for each electron-density, we relax the electrostatic potential. An effective implementation of this procedure requires care with two aspects.

First, the electrostatic potential has to be solved on all space $\mathbb{R}^3$, while the electron-density is solved only on a compact region Ω. Since all the charges are confined to Ω, the electrostatic potential will decay better than $1/r$, since we have charge neutrality. We take advantage of this, and compute the electrostatic potential on a larger domain Ω' satisfying $\Omega^{'} \supset\supset \Omega$, and impose zero Dirichlet boundary conditions on the boundary of the larger domain. Typically, we use $dia(\Omega^{'}) \approx 10^2 dia(\Omega)$ in our calculations. Further, we coarsen our mesh as we go away from Ω to keep the computations efficient and accurate.

Second, we anticipate that the electron-density and the electrostatic potential will be localized near the atomic cores, and will be convected along with the cores as the atomic positions change. In other words, we anticipate that the spatial perturbation of the electron-density will be large as the atomic positions change, but the perturbation to be small in a coordinate system that is convected with the atomic position. Therefore, with each update of the atomic position we convect the finite-element grid, as well as the old electron-density and electrostatic potential, and use this convected electron-density and potential as an initial guess for the subsequent iteration.

We implement these two aspects in the following way by using two triangulations. We

first construct a coarse or atomistic triangulation $\mathtt{T}$ of the large domain $\Omega^{'}$ with K nodal points located at $\{\mathbf{x}_i\}_{i=1}^{K}$. This triangulation contains each initial atomic position as a node so that it has atomic resolution in the small region Ω, and coarsens away from it. We use a coarsening rate of $r^{6/5}$, which is estimated to be optimal for a $1/r$ decay with linear interpolation. The triangulation is generated automatically from Delaunay triangulation of a set of points. This is shown in Figure 3.1. We now introduce a second triangulation $\mathtt{T}'$ which is a uniform subdivision of $\mathtt{T}$ repeated a certain number of times by using the Freudenthal's algorithm for a 3-simplex (Bey, 2000). This triangulation is sufficiently fine to resolve the electronic charges and the electrostatic field, and is shown in Figures 3.2 and 3.3. At any step in the iteration, suppose $\varphi^i : \mathbb{R}^3 \to \mathbb{R}^3$ denote the deformation of

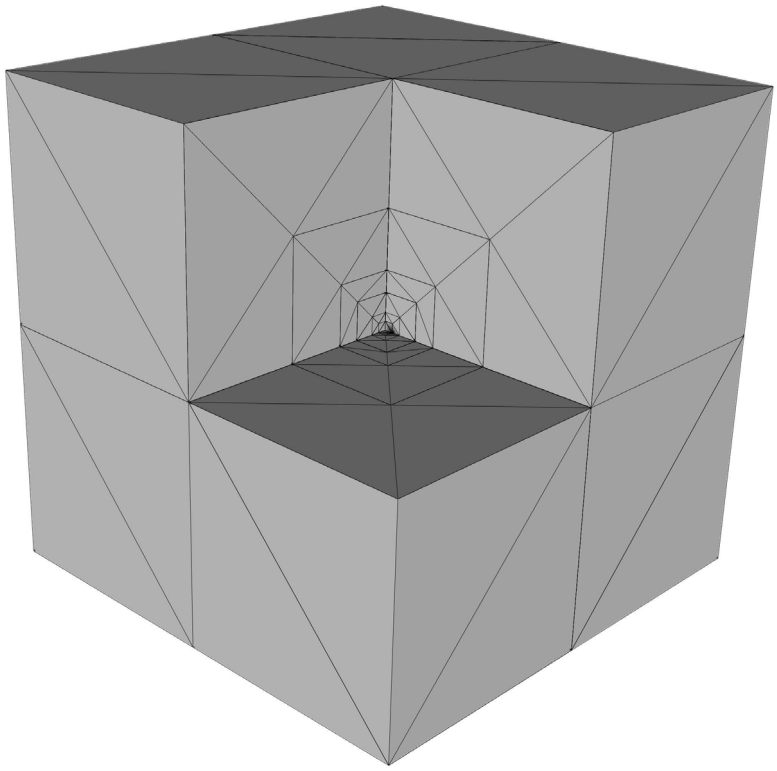

Figure 3.1: Surface mesh of a sliced cubical domain corresponding to the triangulation $\mathtt{T}$

the ith atom. We extend this deformation mapping to all nodes of the triangulation $\mathtt{T}$ by

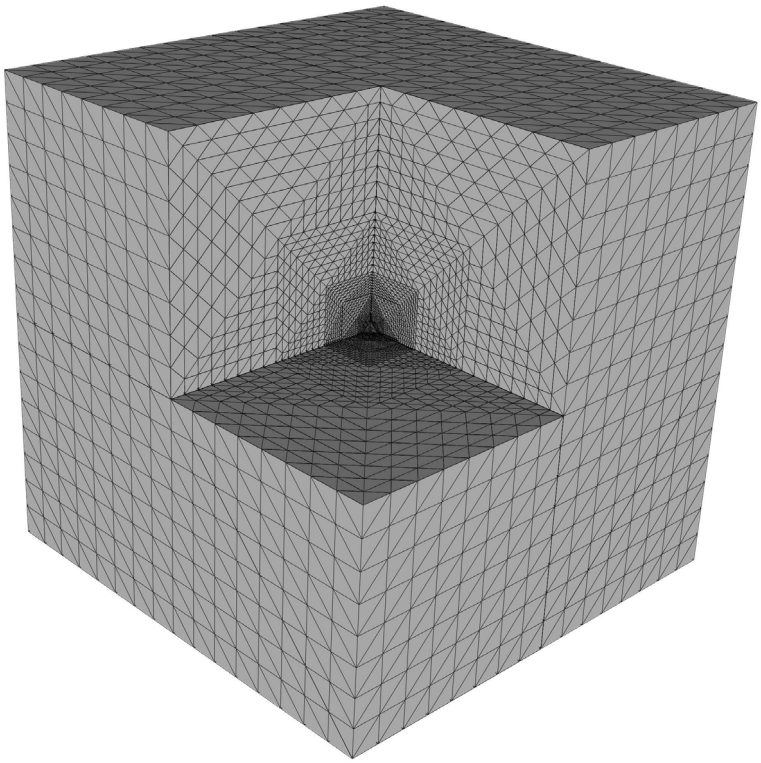

Figure 3.2: Surface mesh of a sliced cubical domain corresponding to the triangulation $\mathtt{T}'$

setting it to zero for nodes that do not coincide with atomic positions, and then use a linear interpolation to extend this deformation to Ω':

$$\varphi(\mathbf{x}) = \sum_{i=1}^{n} \varphi^i N_i(\mathbf{x}) \tag{3.24}$$

where N_i is the shape-function associated with the ith node and n is the number of vertices in the simplex associated with triangulation $\mathtt{T}$. We use this deformation to deform the fine mesh $\mathtt{T}'$. Specifically, we define a new mesh $\mathtt{T}'^{\varphi}$ with nodes

$$\mathbf{x}_a^{\varphi} = \varphi(\mathbf{x}_a) = \sum_{i=1}^{n} \varphi^i N_i(\mathbf{x}_a) \qquad a = 1, \ldots, L \tag{3.25}$$

where $\mathbf{x}_a$ are the position of the nodes of the original triangulation $\mathtt{T}'$ and L is the number

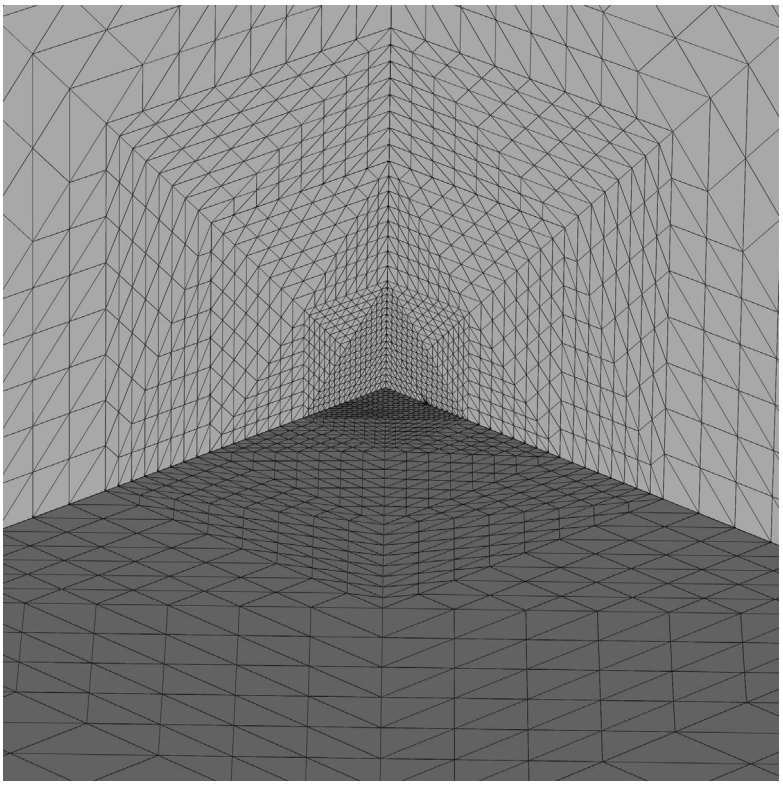

Figure 3.3: Close up of Figure 3.2

of such nodes.

We use this mesh, $\mathtt{T}'^{\varphi}$, to discretize the electron-density and electrostatic potential. It consists of 4-node tetrahedral elements and the interpolating shape functions are linear. We use a 4-point Gaussian quadrature, which is second-order accurate. We solve the finite-element equations using non-linear conjugate gradients with secant method for line search. However, since the mesh is adapted to the updated atomic positions, and the electron-density convected from the previous atomic position (by keeping the nodal values constant while the mesh deforms) is used as an initial guess, the convergence is rapid. Finally, we implement the computation in parallel using domain decomposition.

It is possible that the quality of the triangulation could deteriorate and the aspect ratio of the elements become very small as the mesh deforms. To work around this, with each

update of $\mathtt{T}'^{\varphi}$, we evaluate the minimum value of the aspect ratio (defined as ratio of the radii of inscribed sphere to the circumsphere) amongst all elements, and re-mesh the region with the nodes fixed if it is below a prescribed value.

3.4 Examples

The approach presented is demonstrated and tested by means of simulations performed on atoms, molecules, and clusters of aluminum.

3.4.1 Atoms

The first test case is the hydrogen atom, for which theoretical results are available. We use a value of $\lambda = \frac{1}{3}$, since it gives the best results. Figure 3.4 demonstrates the convergence of our finite-element approach. We use $N_0 \approx 100$ elements for the initial mesh and have $N_0 8^n$ elements after the n^{th} subdivision. It shows that the ground-state energy converges rapidly as the number of subdivisions (i.e., the fineness of the triangulation) is increased. It also shows that the ground-state energy of the hydrogen atom is computed to be -0.495 Hartree, as against the theoretical value of -0.5 Hartree. Figure 3.5 shows the radial distribution of the electron-density around the hydrogen nucleus. It is compared with the theoretical solution obtained by solving the Schrödinger equation. The comparison is very good except at the regions very close to the nucleus, where the simulations predict a slightly higher electron-density. Figure 3.6 shows the radial probability distribution of finding the electron as a function of the distance from the nucleus. We observe that the probability of finding the electron is maximum at a distance of 1 Bohr from the nucleus, which agrees with the theoretical solution.

To simulate atoms heavier than hydrogen atom, $\lambda = \frac{1}{9}$—the conventional gradient cor-

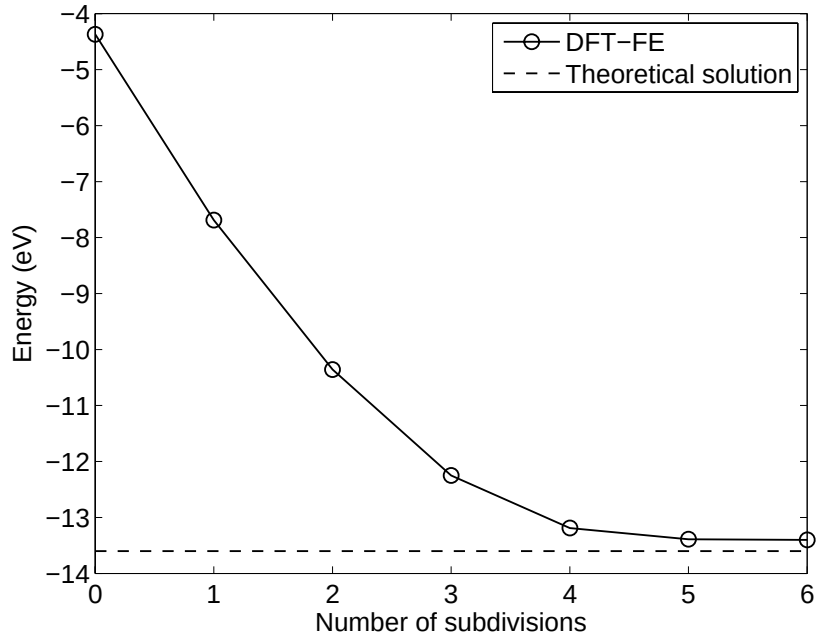

Figure 3.4: Energy of hydrogen atom as a function of number of uniform subdivisions of triangulation T

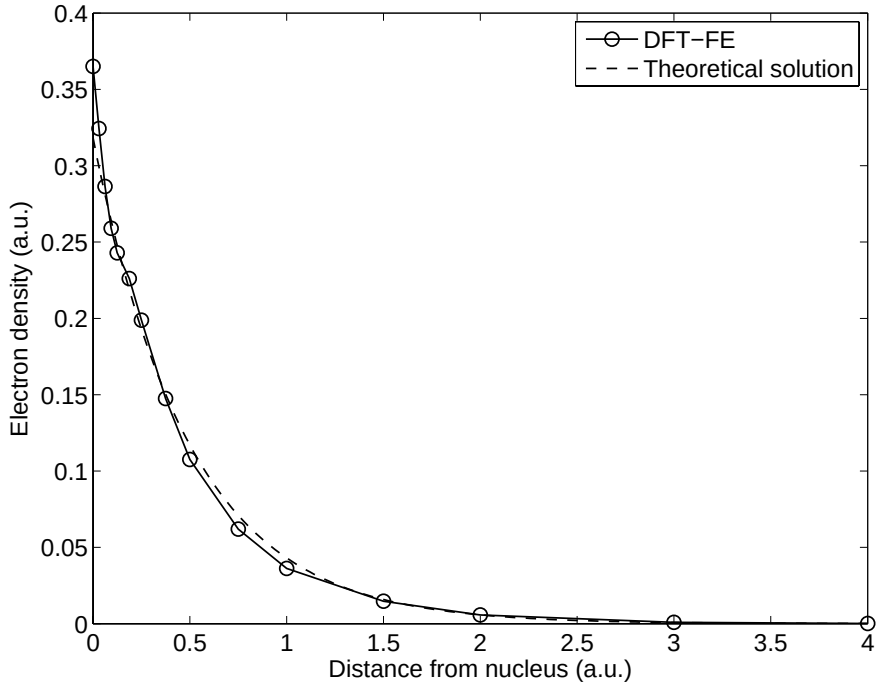

Figure 3.5: Radial distribution of electron-density for hydrogen atom

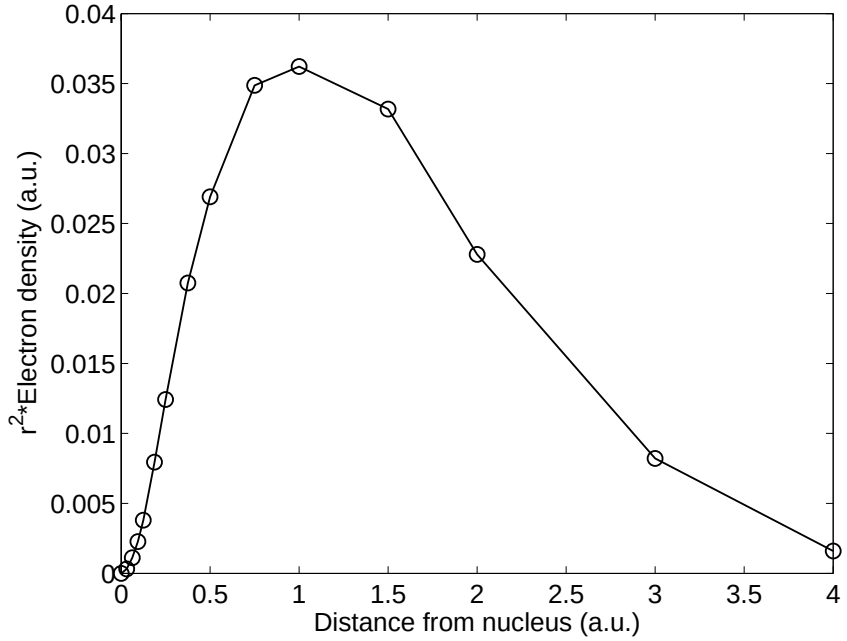

Figure 3.6: Radial probability distribution of finding an electron around the hydrogen nucleus, computed using OFDFT-FE

rection to Thomas-Fermi kinetic energy functional—is used. The ground-state energies of various other atoms estimated from our simulations are tabulated in Table 3.1 under OFDFT-FE, which denotes orbital-free density functional calculation using a finite-element basis. The results obtained are compared with other electronic structure calculations (Tong & Sham, 1966; Clementi et al., 1962), which include the Hartree-Fock approach and the Kohn-Sham approach of density-functional theory using local density approximation for exchange correlation functionals (KS-LDA). The ground-state energies are found to be in good agreement with other electronic structure calculations and experiments.

3.4.2 Molecules

The next set of examples we consider are N_2 and CO molecules. The ground-state energies of these molecules are evaluated at various values of interatomic distances. Using this data,

Table 3.1: Energies of atoms, computed by various techniques, in atomic units

Element	OFDFT-FE	KS-LDA (Tong & Sham, 1966)	Hartree-Fock (Clementi et al., 1962)	Experiments (Tong & Sham, 1966)
He	-2.91	-2.83	-2.86	-2.9
Li	-7.36	-7.33	-7.43	-7.48
Ne	-123.02	-128.12	-128.55	-128.94

Table 3.2: Binding energy and bond length of N_2 molecule, computed by various techniques

Property	OFDFT-FE	KS-LDA (Gunnarsson et al., 1977)	Hartree-Fock (Cade et al., 1973)	Experiments (Huber, 1972)
Binding energy (eV)	-11.9	-7.8	-5.3	-9.8
Bond length (a.u.)	2.7	2.16	2.01	2.07

the binding energies and bond lengths of the molecules are determined. Figure 3.7 shows the binding energy for N_2 molecule as a function of the interatomic distance. The interatomic potential energy has the same form as other popular interatomic potentials like Lennard-Jones and Morse potentials. Tables 3.2 and 3.3 show the comparison of binding energies and bond lengths of N_2 and CO molecules predicted from our simulations with those from other electronic structure calculations and experiments (Gunnarsson et al., 1977; Cade et al., 1973; Hou, 1965; Huber, 1972). Binding energies are calculated using the standard expression, binding energy $= E_{AB} - E_A - E_B$, where E_{AB} is the energy of the molecule AB, E_A, and E_B are the energies of a single atoms A and B respectively.

There is reasonable agreement of our simulations with experiments in terms of the binding energies. But there is a considerable deviation in the values of predicted bond lengths in comparison to other calculations and experiments. We believe that this is due to the well-understood limitation of the orbital-free kinetic energy functionals in the presence of strong covalent bonds (Parr & Yang, 1989).

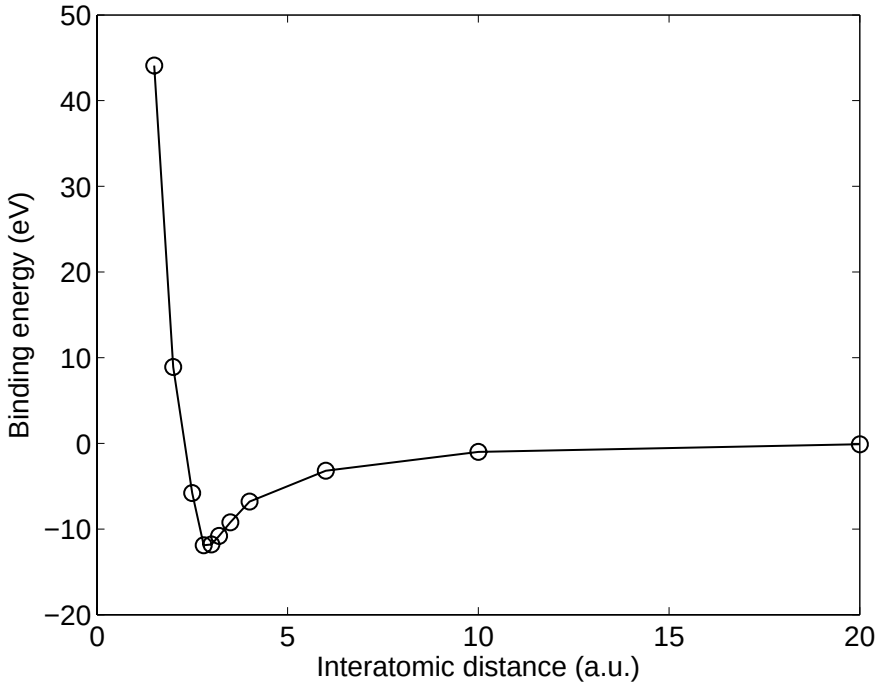

Figure 3.7: Binding energy of N_2 molecule as a function of interatomic distance, computed using OFDFT-FE

Table 3.3: Binding energy and bond length of CO molecule, computed by various techniques

Property	OFDFT-FE	KS-LDA (Gunnarsson et al., 1977)	Hartree-Fock (Hou, 1965)	Experiments (Huber, 1972)
Binding energy (eV)	-12.6	-9.6	-7.9	-11.2
Bond length (a.u.)	2.75	2.22	2.08	2.13

3.4.3 Aluminum clusters

The final set of examples we consider are aluminum clusters. We choose $\lambda = \frac{1}{6}$, which was found to yield good results. The simulations are performed using a modified form of Heine-Abarenkov pseudopotential for aluminum (Goodwin et al., 1990), which in real-space has the form,

$$V_{ext} = \begin{cases} -\frac{Z_v}{r}, & \text{if } r \geq r_c; \\ -A, & \text{if } r < r_c; \end{cases} \tag{3.26}$$

where Z_v is the number of valence electrons, r_c the cut-off radius, and A is a constant. For aluminum, $Z_v = 3$, $r_c = 1.16$ a.u., $A = 0.11$ a.u.. Simulations are performed on clusters consisting of $1 \times 1 \times 1$, $3 \times 3 \times 3$, $5 \times 5 \times 5$, and $9 \times 9 \times 9$ face-centered-cubic (fcc) unit cells. The number of atoms in the cluster consisting of $9 \times 9 \times 9$ fcc unit cells is 3730, and close to 6 million finite-elements are used in this simulation. It took more than 10,000 CPU hours on 2.4 GHz Opteron processors for each simulation on the cluster with $9 \times 9 \times 9$ fcc unit cells to converge. Figures 3.8 and 3.9 show the contours of electron-density for a cluster consisting of $3 \times 3 \times 3$ fcc unit cells. Figure 3.10 shows the binding energy per atom as a function of the lattice constant (size of the fcc cell) for the various cluster sizes, along with cubic polynomial fits of the simulated points. We calculate the binding energy using the standard approach; E_{bind}(per atom) $= (E(n) - nE_0)/n$, where $E(n)$ is the energy of the cluster/unit cell containing n atoms and E_0 is the energy of a single atom. An important observation from these figures is the anharmonic nature of the binding energy.

The binding energies evaluated in these simulations include, along with the bulk cohesive energy, the effects of surfaces, edges, and corners. A classical interpretation of these energies

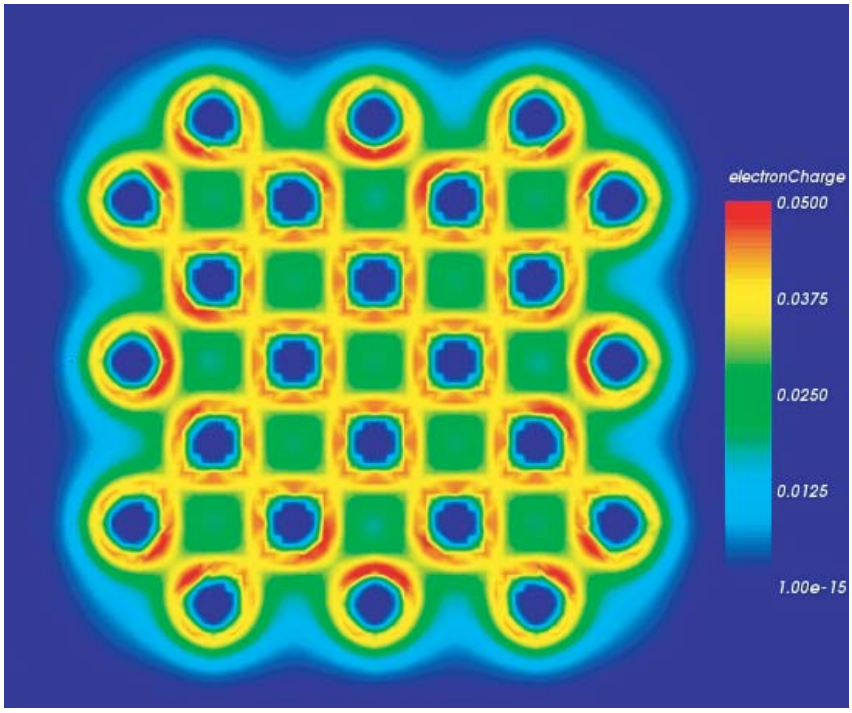

Figure 3.8: Contours of electron-density on the mid plane of an aluminum cluster with 3x3x3 fcc unit cells

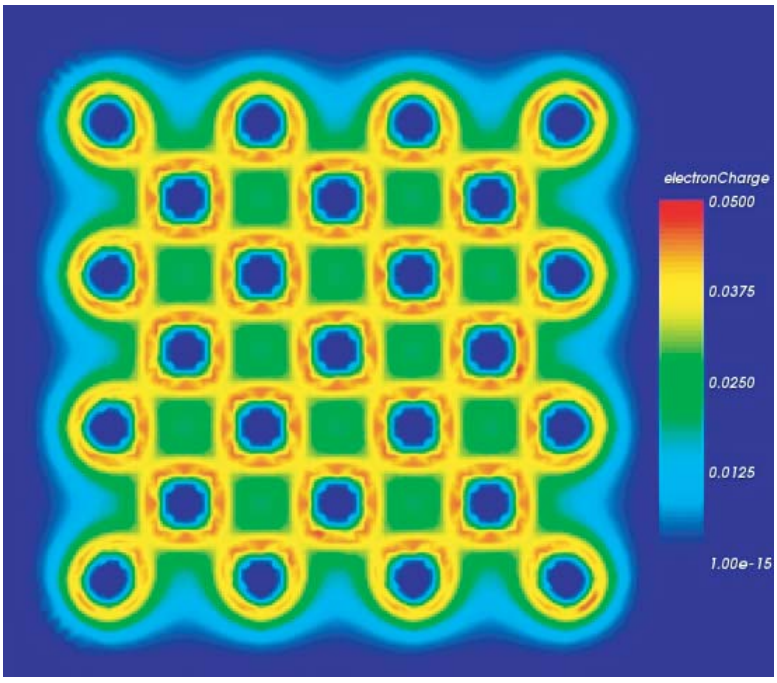

Figure 3.9: Contours of electron-density on the face of an aluminum cluster with 3x3x3 fcc unit cells

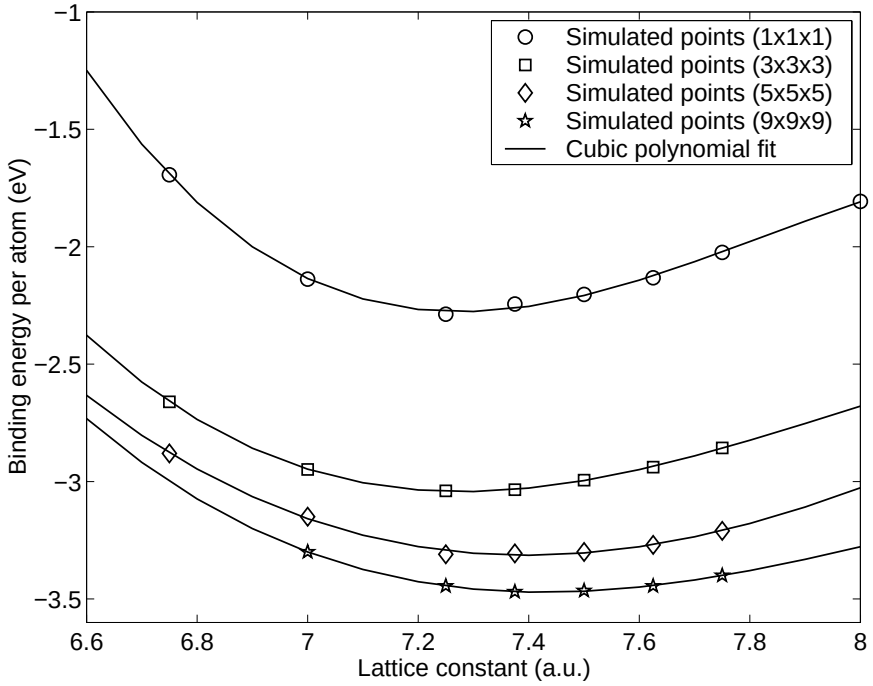

Figure 3.10: Binding energy per atom as a function of lattice constant in a fcc cluster with $1 \times 1 \times 1$, $3 \times 3 \times 3$, $5 \times 5 \times 5$ and $9 \times 9 \times 9$ unit cells of aluminum atoms, computed using OFDFT-FE

would suggest a scaling of the form

$$\epsilon_n = \epsilon_{coh} + n^{-1/3}\epsilon_{surf} + n^{-2/3}\epsilon_{edge} + n^{-1}\epsilon_{corn}, \tag{3.27}$$

where n represents the number of atoms, ϵ_{coh} the cohesive energy of the bulk, ϵ_{surf} the surface energy, ϵ_{edge} the energy contributed by presence of edges, and ϵ_{corn} the energy resulting from the corners. Figure 3.11 shows the plot of binding energy per atom of each cluster in the relaxed configuration as a function of $n^{-1/3}$. The relationship is almost linear, which supports the scaling relation given in (3.27). Further, it shows that cohesive and surface energies dominate edge and corners even for relatively small clusters. Finally, this scaling allows us to extract the bulk cohesive energy of aluminum from the binding energies of the clusters.

The values of the bulk modulus of these clusters are evaluated from the binding energy calculations. Figure 3.12 shows the linear dependence of bulk modulus on $n^{-1/3}$, implying that bulk modulus can also be expressed as a scaling relation suggested by (3.27).

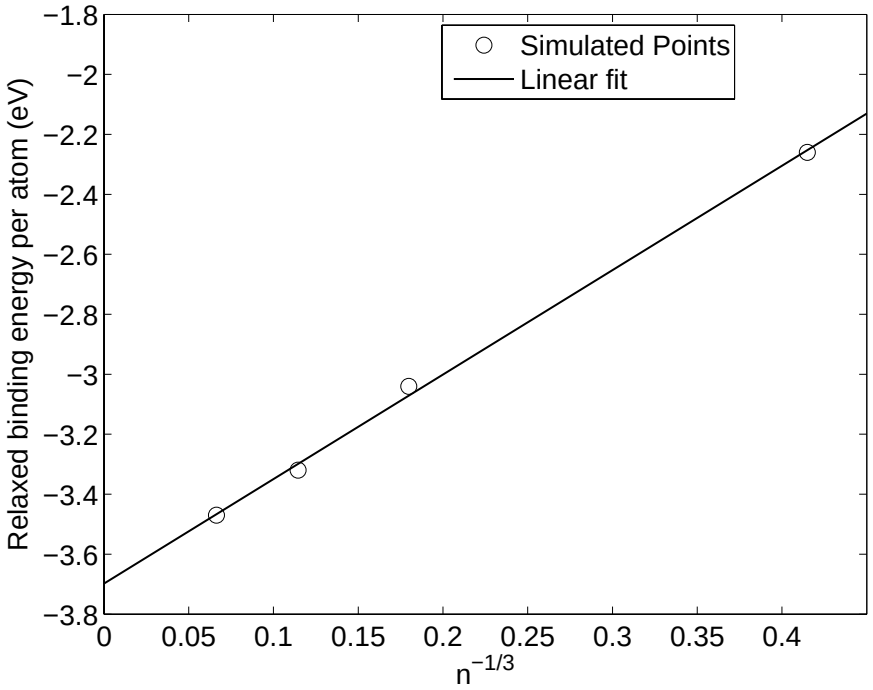

Figure 3.11: Relaxed binding energies per atom of aluminum clusters against $n^{-1/3}$

Table 3.4 shows the variation of the lattice constant with the cluster size. We do not find significant dependence or a clear trend in the dependence of lattice constant on cluster size. Table 3.5 shows a comparison of the bulk properties of aluminum obtained from our simulations with other electronic structure calculations (Goodwin et al., 1990) and experiments (Brewer, 1977; Gschneider, 1964). We have very good quantitative agreement in terms of both cohesive energies and bulk modulus. The lattice constant of $9 \times 9 \times 9$ cluster is 7.42, which is very close to that predicted by KS-LDA (7.44).

In all the simulations discussed so far, the ground-state energy calculations were performed for fixed atomic positions. However, the formulation developed is capable of equili-

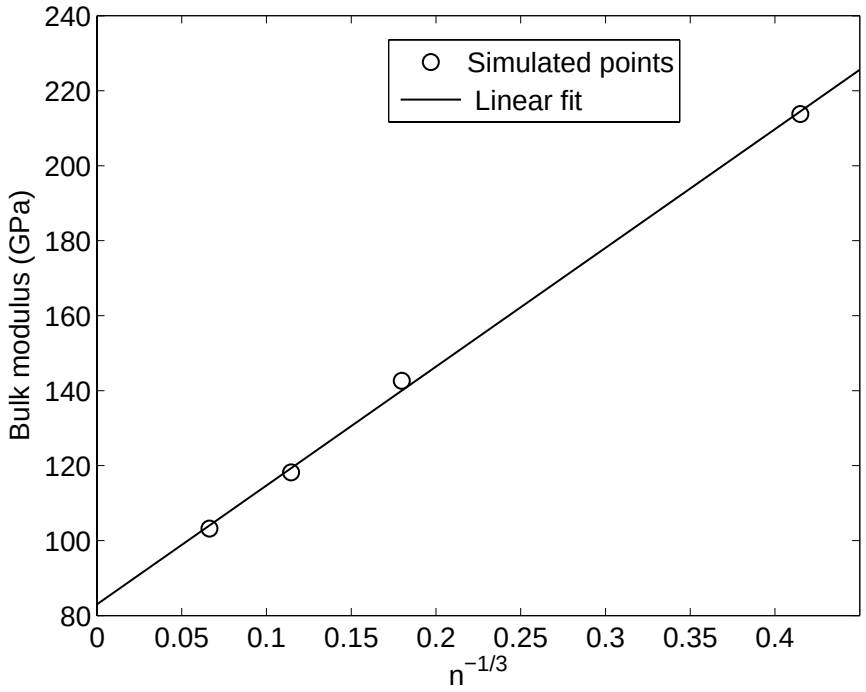

Figure 3.12: Bulk modulus of aluminum clusters against $n^{-1/3}$

Table 3.4: Relaxed lattice constants of various cluster sizes, computed using OFDFT-FE

Cluster size	$1 \times 1 \times 1$	$3 \times 3 \times 3$	$5 \times 5 \times 5$	$9 \times 9 \times 9$
Relaxed lattice constant (a.u.)	7.26	7.27	7.39	7.42

Table 3.5: Bulk properties of aluminum, computed using various techniques

Bulk Property	OFDFT-FE	KS-LDA (Goodwin et al., 1990)	Experiments (Brewer, 1977; Gschneider, 1964)
Cohesive energy (eV)	3.69	3.67	3.4
Bulk modulus (GPa)	83.1	79.0	74.0

Table 3.6: Comparison of properties of aluminum clusters Al_n, $n = 2, 3, 4$, obtained from OFDFT-FE calculations with other DFT calculations; G denotes the symmetry group, E_b denotes the binding energy per atom (eV), R_e denotes equilibrium distances (a.u.)

n	G	OFDFT-FE		AE (Ahlrichs & Elliot, 1999)	
		E_b	R_e/angle	E_b	R_e/angle
2	$D_{\infty h}$	-0.86	4.97	-0.78	4.72
3	D_{3h}	-1.24	5.06	-1.29	4.77
3	C_{2v}	-1.16	5.14	-1.22	4.91
4	D_{2h}	-1.38	$5.22/71^o$	-1.5	$4.85/68^o$
4	C_{3v}	-1.31		-1.39	

brating the nuclear positions and predicting the various stable configurations of atoms. To this end, we perform simulations on small aluminum clusters to predict the binding energies and the equilibrated structures of these clusters. Since the energy is non-convex with respect to the positions of the nuclei, we start our simulations from various initial configurations to predict the stable configurations of these clusters. We performed simulations on small aluminum clusters consisting of two, three, and four atoms. Table 3.6 shows the results of our simulations and a comparison with other DFT calculations (Ahlrichs & Elliot, 1999). We successfully predict the various stable configurations of these clusters, and the binding energies of these clusters are in good agreement with other calculations. However, there is some deviation in the predicted geometry. This deviation could be attributed to the fact that the bonding in these small aluminum clusters is covalent in nature and orbital-free kinetic functionals are not very appropriate for systems with covalent bonds.

3.5 Summary

We have developed a real-space finite-element formulation of density-functional calculations based on orbital-free kinetic energy functionals to perform ground-state energy calculations. This formulation addresses problems which are non-periodic in nature, like defects in solids, which can not be treated accurately with existing techniques employing periodic boundary conditions. The local structure of the finite-element basis aids parallel implementation, and enables us to solve large systems with thousands of atoms effectively, which has been demonstrated through simulations on large aluminum clusters.

The method was tested by carrying out simulations on atoms, molecules, and large clusters of aluminum in fcc structure. We have also predicted some stable structures in small aluminum clusters. The results from these simulations – which include energies of atoms, binding energies and bond lengths of molecules, bulk properties of aluminum, and stable configurations of small aluminum clusters along with their binding energies – are compared with other electronic structure calculations and experiments. In most cases the agreement has been very good, except in the case of molecules, where there is considerable deviation in the bond length predicted. This can be attributed to the inability of the orbital-free kinetic energy functionals to approximate the kinetic energy of non-interacting electrons well in systems with strong covalent bonding.

This framework is developed with a larger goal in mind, which is to coarse-grain orbital-free density-functional theory in a seamless atomistic-continuum formulation. This coarse-graining is the topic of discussion in Chapter 5. Such a formulation is necessary to accurately study defects in solids like vacancies, dislocations, and cracks, where the local structure and long range elastic fields interact in a non-trivial manner.

Chapter 4

Convergence analysis

Chapter 3 described the formulation of the ground-state energy of a system using orbital-free density-functional theory as a local variational problem in real-space. Further, this formulation was discretized and computed using a finite-element basis. As this real-space formulation has a variational structure, it is of interest and importance to understand the properties of this variational problem. In particular, one problem of importance is understanding whether the variational problem is well-posed: i.e., does there exist a minimizer for the energy functional described by orbital-free density-functional theory? If the variational problem is well-posed, then a subsequent question of great importance is: does the finite-element discretization converge for the class of functionals which describe orbital-free density-functional theory? This chapter probes into these questions. Section 4.1 proves the existence of minimizers for energy functionals which describe orbital-free density-functional theory. Section 4.2 establishes the convergence of the finite-element discretization rigorously, using the mathematical technique of $\Gamma-$convergence. This is a notion of convergence of functionals introduced by De Giorgi & Franzoni (1975) (also see Dal Maso (1993) for a detailed introduction) that has recently been used in a variety of multi-scale problems. In the present context, consider a sequence of finer and finer finite-element approximations. These generate a sequence of functionals, and we show that this sequence of functionals

$\Gamma-$converge to the exact functional associated with our real-space formulation. While the exact definition is technical, $\Gamma-$ convergence states in spirit that solutions of the sequence of approximate functionals converge to the solution of the exact functional. Further, Section 4.3 describes the convergence of the numerical quadratures introduced in the practical implementation of the finite-element method. The results presented in this chapter establish rigorously that the real-space variational problem described in Chapter 3 is mathematically well-posed, and the finite-element approximation used to discretize and compute the formulation converges.

4.1 Properties of the OFDFT variational problem

We begin by establishing certain properties of the OFDFT variational problem that play a fundamental role in the analysis of convergence presented in the sequel. To keep the analysis simple we treat the electrostatics on a large but bounded domain with compact support. To this end, we consider energy functionals $E : W^{1,p}(\Omega) \to \overline{\mathbb{R}}$ of the form

$$E(u) = \int_\Omega f(\nabla u) d\mathbf{r} + \int_\Omega g(u) d\mathbf{r} + J(u)$$
$$J(u) = -\inf_{\phi \in H_0^1(\Omega)} \{\frac{1}{2}\int_\Omega |\nabla \phi|^2 d\mathbf{r} - \int_\Omega (u^2 + b(\mathbf{r}))\phi d\mathbf{r}\},$$

where Ω is an open bounded subset of $\mathbb{R}^N$, with $\partial\Omega$ Lipschitz continuous. $b(\mathbf{r})$ is a smooth, bounded function in $\mathbb{R}^N$. We assume:

(i) f is convex and continuous on $\mathbb{R}^N$.

(ii) f satisfies the growth condition, $c_0|\psi|^p - a_0 \leq f(\psi) \leq c_1|\psi|^p - a_1$, $1 < p < \infty$, where $c_0, c_1 \in \mathbb{R}^+$, $a_0, a_1 \in \mathbb{R}$.

(iii) g is continuous on $\mathbb{R}$.

(iv) g satisfies the growth condition, $c_2|s|^q - a_2 \leq g(s) \leq c_3|s|^q - a_3$, $q \geq p$, where $c_2, c_3 \in \mathbb{R}^+$, $a_2, a_3 \in \mathbb{R}$.

Let $F : W^{1,p}(\Omega) \to \overline{\mathbb{R}}$ and $G : W^{1,p}(\Omega) \to \overline{\mathbb{R}}$ be functionals defined by,

$$F(u) = \int_\Omega f(\nabla u) d\mathbf{r} \qquad G(u) = \int_\Omega g(u) d\mathbf{r}.$$

We note that the growth conditions imply, $|f(\psi)| \leq c(1 + |\psi|^p)$ and $|g(s)| \leq c(1 + |s|^q)$. Hence, it follows that, $F(u)$ is continuous in $W^{1,p}(\Omega)$ and $G(u)$ is continuous in $L^q(\Omega)$ (cf, e. g., Remark 2.10, Braides (2002)).

Let $X = \{u | u \in W^{1,p}(\Omega), \|u\|_{L^2(\Omega)} = 1\}$ with norm induced from $W^{1,p}(\Omega)$. Let, $\frac{1}{p^*} = \frac{1}{p} - \frac{1}{N}$.

Lemma 4.1.1. *X is closed in the weak topology of $W^{1,p}(\Omega)$ if $p^* > 2$.*

Proof. We can rewrite X as $X = W^{1,p}(\Omega) \cap K$, where $K = \{u \in L^2(\Omega) | \|u\|_{L^2(\Omega)} = 1\}$. Let $(u_h) \in X$, $u_h \rightharpoonup u$ in $W^{1,p}(\Omega)$. If $p^* > 2$, then $W^{1,p}(\Omega)$ is a compact injection into $L^2(\Omega)$. Hence, $u_h \to u$ in $L^2(\Omega)$. Thus, $1 = \|u_h\|_{L^2(\Omega)} \to \|u\|_{L^2(\Omega)}$ Hence, $u \in K$ and it follows that X is closed in the weak topology of $W^{1,p}(\Omega)$. □

In this section we establish the existence of a minimum point of the energy functional $E(u)$ in X. Let,

$$I(\phi, u) = \frac{1}{2} \int_\Omega |\nabla \phi|^2 d\mathbf{r} - \int_\Omega (u^2 + b)\phi d\mathbf{r}, \quad \phi \in H_0^1(\Omega) \quad u \in W^{1,p}(\Omega).$$

Hence,

$$J(u) = -\inf_{\phi \in H_0^1(\Omega)} I(\phi, u).$$

For every $u \in L^4(\Omega)$, $I(., u)$ admits a minimum. This follows from Poincaré inequality and Lax-Milgram Lemma. Therefore,

$$J(u) = -\min_{\phi \in H_0^1(\Omega)} I(\phi, u).$$

Lemma 4.1.2. *J is continuous in $L^4(\Omega)$.*

Proof. If ϕ_u denotes the minimizer of $I(., u)$, then for every $u, v \in L^4(\Omega)$, we have,

$$\int_\Omega \nabla(\phi_u - \phi_v).\nabla\psi d\mathbf{r} = \int_\Omega (u^2 - v^2)\psi d\mathbf{r} \quad \forall \psi \in H_0^1(\Omega).$$

Hence, from Poincaré and Cauchy-Schwartz inequality, it is immediate that,

$$\|\phi_u - \phi_v\|_{H_0^1(\Omega)} \leq C\|u^2 - v^2\|_{L^2(\Omega)}.$$

Continuity of J thus follows. □

Let us denote by Hypothesis H, the condition, $p^* > \max\{q, 4\}$.

Lemma 4.1.3. *If the Hypothesis H is satisfied, then E is lower semi-continuous (l.s.c) in the weak topology of X.*

Proof. We noted previously that F is continuous in $W^{1,p}(\Omega)$. As F is convex, it follows that F is l.s.c in the weak topology of $W^{1,p}(\Omega)$ (cf, e. g. Prop. 1.18, Dal Maso (1993)). If the hypothesis H is satisfied, then $W^{1,p}(\Omega)$ is a compact injection into $L^q(\Omega)$ and $L^4(\Omega)$. G is continuous in $L^q(\Omega)$, as noted previously, and from Lemma 4.1.2, J is continuous in

$L^4(\Omega)$. Hence, it follows that, G and J are l.s.c and thus E is l.s.c in the weak topology of $W^{1,p}(\Omega)$. As X is a subset of $W^{1,p}(\Omega)$, it follows that E is l.s.c in the weak topology of X. □

Lemma 4.1.4. *E is coercive in the weak topology of X.*

Proof. If we establish the coercivity of E in the weak topology of $W^{1,p}(\Omega)$, the coercivity of E in the weak topology of X follows from Lemma 4.1.1. We note that $J(u)\geq 0$. Hence,

$$\begin{aligned} E(u) &\geq c_0\|\nabla u\|^p_{L^p(\Omega)} + c_2\|u\|^q_{L^q(\Omega)} - (a_0+a_2)\Omega \\ &\geq c_0\|\nabla u\|^p_{L^p(\Omega)} + \frac{c_1}{C^q_\Omega}\|u\|^q_{L^p(\Omega)} - C = K(u) \quad \text{as } p\leq q \end{aligned}$$

If the function K is bounded, then $\|u\|_{W^{1,p}(\Omega)}$ is bounded. As $W^{1,p}(\Omega)$ is reflexive ($1 < p < \infty$), it follows that K is coercive in the weak topology of $W^{1,p}(\Omega)$. Hence, E is coercive in the weak topology of $W^{1,p}(\Omega)$ and from Lemma 4.1.1, E is coercive in the weak topology of X. □

Theorem 4.1.1. *$E(u)$ has a minimum in X.*

Proof. It follows from Lemma 4.1.3, Lemma 4.1.4, and Theorem 1.15, Dal Maso (1993). □

The orbital-free density functional under consideration falls into the class of functionals being discussed with $J(u)$ representing the classical electrostatic interaction energy. The constraint on electron density is imposed explicitly through the space X. It is easy to check that the energy functional satisfies conditions (i)-(iv) with $p = 2$, $q = 10/3$. As $\Omega \subset \mathbb{R}^3$, we estimate $p^* = 6$. Hence, the hypothesis H is satisfied and all the results apply to the specific energy functional.

4.2 Γ-convergence of the finite-element approximation

Finite-element approximations to the solutions of the OFDFT variational problem are obtained by restricting minimization to a sequence of increasing finite-dimensional subspaces of X. Thus, let T_h be a sequence of triangulations of Ω of decreasing mesh size, and let X_h be the corresponding sequence of subspaces of X consisting of functions whose restriction to every cell in T_h is a polynomial function of degree $k \geq 1$. A standard result in approximation theory (cf, e. g., Ciarlet (2002)) shows that the sequence (X_h) is dense in X, i. e., for every $u \in X$ there is a sequence $u_h \in X_h$ such that $u_h \to u$. Let $X_{1_h} = \{\phi | \phi \in H_0^1(\Omega)$, ϕ is piece-wise polynomial function corresponding to triangulation $T_h\}$ denote a sequence of constrained spaces of the space $H_0^1(\Omega)$. The sequence of spaces (X_{1_h}) is such that $\cup_h X_{1_h}$ is dense in $H_0^1(\Omega)$. We now define a sequence of finite-element energy functionals:

$$E_h(u) = \begin{cases} F(u) + G(u) + J_h(u), & \text{if } u \in X_h; \\ +\infty, & \text{otherwise;} \end{cases}$$

where

$$J_h(u) = - \min_{\phi \in H_0^1(\Omega)} I_h(\phi, u)$$

and

$$I_h(\phi, u) = \begin{cases} I(\phi, u), & \text{if } \phi \in X_{1_h}, u \in X_h; \\ +\infty, & \text{otherwise;} \end{cases}$$

Then, we would like to establish convergence of the sequence of functionals E_h to E in a sense such that the corresponding convergence of minimizers is guaranteed. This natural notion of convergence of variational problems is provided by Γ-convergence (cf, e. g., Dal

Maso (1993) for comprehensive treatises on the subject). In the remainder of this section, we show the Γ-convergence of the finite-element approximation and attendant convergence of the minima. We also extend the analysis of convergence to approximations obtained using numerical quadrature.

To analyze the behavior of the sequence of functionals, E_h, it is important to understand the behavior of J_h. We first note some properties of J_h before analyzing E_h.

Lemma 4.2.1. *If $u_h \to u$ in $L^4(\Omega)$, then for any $\phi_h \rightharpoonup \phi$ in $H_0^1(\Omega)$, $\liminf_{h\to\infty} I(\phi_h, u_h) \geq I(\phi, u)$.*

Proof. $I(\phi, u) = \frac{1}{2}\int_\Omega |\nabla\phi|^2 d\mathbf{r} - \int_\Omega (u^2 + b)\phi d\mathbf{r}$. L.s.c of $\int_\Omega |\nabla\phi|^2 d\mathbf{r}$ in the weak topology of $H_0^1(\Omega)$ follows from Prop 2.1, Dal Maso (1993). As $u_h \to u$ in $L^4(\Omega)$, $\lim_{h\to\infty}\int_\Omega (u_h^2 + b)\phi_h d\mathbf{r} = \int_\Omega (u^2 + b)\phi d\mathbf{r}$. Putting both the terms together we get, $\liminf_{h\to\infty} I(\phi_h, u_h) \geq I(\phi, u)$. □

Lemma 4.2.2. *If $u_h \to u$ in $L^4(\Omega)$, then $(I_h(., u_h))$ is equi-coercive in the weak topology of $H_0^1(\Omega)$.*

Proof.

$$I(\phi, u) \geq C\|\phi\|^2_{H_0^1(\Omega)} - (\|u^2\|_{L^2(\Omega)} + \|b\|_{L^2(\Omega)})\|\phi\|_{L^2(\Omega)}. \tag{4.1}$$

$I_h(., u_h) \geq I(., u_h) \geq I^*$ where $I^*(\phi) = C\|\phi\|^2_{H_0^1(\Omega)} - K\|\phi\|_{L^2(\Omega)}$, $K = \sup_h \|{u_h}^2\|_{L^2(\Omega)} + \|b\|_{L^2(\Omega)}$. Since, $u_h \to u$ in $L^4(\Omega)$ and b is a bounded function, K is bounded. This implies, I^* is coercive in the weak topology of $H_0^1(\Omega)$. Thus it follows that, $(I_h(., u_h))$ is equi-coercive in the weak topology of $H_0^1(\Omega)$. □

Theorem 4.2.1. *If $(u_h) \in (X_h)$ is a sequence such that $u_h \to u$ in $L^4(\Omega)$, then $I_h(., u_h) \rightharpoonup^\Gamma I(., u)$ in weak topology of $H_0^1(\Omega)$.*

Proof. Let (ϕ_h) be any sequence $\ni \phi_h \rightharpoonup \phi$ in $H_0^1(\Omega)$. $I_h(\phi_h, u_h) \geq I(\phi_h, u_h)$. Hence, $\liminf_{h\to\infty} I_h(\phi_h, u_h) \geq \liminf_{h\to\infty} I(\phi_h, u_h)$. But from Lemma 4.2.1, $\liminf_{h\to\infty} I(\phi_h, u_h) \geq I(\phi, u)$. Hence, $\liminf_{h\to\infty} I_h(\phi_h, u_h) \geq I(\phi, u)$. Now we construct the recovery sequence from interpolated functions. Let (ϕ_h) be a sequence constructed from the interpolation functions of successive triangulations such that $\phi_h \to \phi$ in H_0^1. As $\phi_h \to \phi$ in $H_0^1(\Omega)$, $\|\nabla\phi_h\|_{L^2(\Omega)} \to \|\nabla\phi\|_{L^2(\Omega)}$. Also, as $u_h \to u$ in $L^4(\Omega)$, $\lim_{h\to\infty} \int_\Omega (u_h^2 + b)\phi_h d\mathbf{r} = \int_\Omega (u^2 + b)\phi d\mathbf{r}$. Hence, $\lim_{h\to\infty} I_h(\phi_h, u_h) = I(\phi, u)$. This shows that, $I_h(., u_h) \rightharpoonup^\Gamma I(., u)$ in weak topology of $H_0^1(\Omega)$. □

Theorem 4.2.2. *If $(u_h) \in (X_h)$ is a sequence such that $u_h \rightharpoonup u$ in $L^4(\Omega)$, then $\lim_{h\to\infty} J_h(u_h) = J(u)$.*

Proof. Follows from Lemma 4.2.2, Theorem 4.2.1, and Theorem 7.8, Dal Maso (1993). □

Lemma 4.2.3. *Let $u_h \rightharpoonup u$ in X, then $\liminf_{h\to\infty} E_h(u_h) \geq E(u)$ if the hypothesis H is satisfied.*

Proof. We need to consider 2 cases.

Case1: There is no sub-sequence (u_{h_k}) such that $(u_{h_k}) \in X_{h_k}$

$\liminf_{h\to\infty} E_h(u_h) = +\infty$. Hence, $\liminf_{h\to\infty} E_h(u_h) \geq E(u)$.

Case2:$\exists$ sub-sequence (u_{h_k}) such that $(u_{h_k}) \in X_{h_k}$

Using Theorem 4.2.2, the proof for this case follows on the same lines as Lemma 4.1.3. □

Theorem 4.2.3. *$E_h \rightharpoonup^\Gamma E$ in weak topology of X if the hypothesis H is satisfied.*

Proof. Let (u_h) be any sequence $\ni u_h \rightharpoonup u$ in X. From Lemma 4.2.3, it follows that $\liminf_{h\to\infty} E_h(u_h) \geq E(u)$.

Now let's construct the recovery sequence. Let (u_h) be a sequence constructed from the

interpolation functions of successive triangulations such that, $u_h \to u$ in X. From Theorem 4.2.2 and continuity of F and G, it follows that $\lim_{h\to\infty} E_h(u_h) = E(u)$. Thus, $E_h \rightharpoonup^{\Gamma} E$ in weak topology of X. □

Lemma 4.2.4. *(E_h) is equi-coercive in the weak topology of X if the hypothesis H is satisfied.*

Proof. Noting that $E_h(u) \geq F(u) + G(u) + J_h(u)$ and $J_h(u) \geq 0$ if $u \in X_h$, the proof follows on the same lines as Lemma 4.1.4. □

Theorem 4.2.4. *$\lim_{h\to\infty} \inf_X E_h = \min_X E$ if the hypothesis H is satisfied.*

Proof. Follows from Lemma 4.2.4, Theorem 4.2.3 and Theorem 7.8, Dal Maso (1993). □

4.3 Γ-convergence of the finite-element approximation with numerical quadratures

Let $f : \Omega \to \mathbb{R}$, $\Omega \subset \mathbb{R}^N$, Ω bounded, be a function in $W^{n+1,1}(\Omega)$ and $I = \int_\Omega f(\mathbf{r})d\mathbf{r}$. Define the quadrature of I to be

$$\tilde{I} = \sum_{i=1}^{P} C_i f(\mathbf{r}(\xi_i))$$

where P denotes the number of quadrature points and C and ξ denote the weights and quadrature points. If the quadrature rule is of n^{th} order, then the values of C and ξ are determined such that all polynomials up to degree n are integrated exactly. If the quadrature rule is n^{th} order, then the error due to the quadrature rule is given by

$$|\tilde{I} - I| \leq K C_\Omega^{(n+1)} \int_\Omega |f^{(n+1)}(\mathbf{r})| d\mathbf{r},$$

where $f^{(n+1)}$ denotes the $n+1^{th}$ derivative of f and C_Ω represents the size of the domain. Define $\tilde{I}_h$ as,

$$\tilde{I}_h(\phi,u) = \begin{cases} \tilde{I}(\phi,u), & \text{if } \phi \in X_{1_h}, u \in X_h; \\ +\infty, & \text{otherwise;} \end{cases}$$

We rewrite $\tilde{I}_h$ as

$$\tilde{I}_h(\phi,u) = I_h(\phi,u) + \Delta I_h(\phi,u),$$

where $\Delta I_h(\phi,u)$ is a perturbation of $I_h(\phi,u)$ introduced due to numerical quadrature and is given by

$$\Delta I_h(\phi,u) = \begin{cases} \tilde{I}(\phi,u) - I(\phi,u), & \text{if } \phi \in X_{1_h}, u \in X_h; \\ 0, & \text{otherwise;} \end{cases}$$

To estimate the error in the energy introduced due to the quadrature, we assume that the family of triangulations (T_h) are regular, affine and satisfy the inverse assumption (cf, e. g., Ciarlet (2002)). If the quadrature rule is n^{th} order, then the error due to the quadrature for $\phi \in X_{1_h}$ and $u \in X_h$ is given by

$$\begin{aligned} |\Delta I_h(\phi,u)| &\leq Ch_0^{n+1} \sum_i \int_{e_i} |D^{n+1}[\frac{1}{2}|\nabla\phi|^2 - (u^2+b)\phi]|d\mathbf{r} \\ &\leq Ch_0^{n+1} \sum_i \int_{e_i} \{|D^{n+1}|\nabla\phi|^2| + |D^{n+1}((u^2+b)\phi)|\}d\mathbf{r} \\ &\leq Ch_0^{n+1} \sum_i \int_{e_i} \{|D^{n+1}|\nabla\phi|^2| + C_1 h_0^{-n}|D(u^2\phi)| + C_2 h_0^{-n}|D(\phi)|\}d\mathbf{r}, \end{aligned} \tag{4.2}$$

where e_i denotes the i^{th} element and h_0 is characteristic of the size of the largest element in the finite-element mesh. The last inequality in (4.2) is obtained by using the inverse

inequality (Ciarlet, 2002). We note that, as $h \to \infty$, $h_0 \to 0$. Let k denote the degree of polynomials used for finite-element interpolation.

Lemma 4.3.1. *If $(u_h) \in (X_h)$ is a sequence such that $u_h \rightharpoonup u$ in X, $(n-2k+3) > 0$, $p \geq 2$ and the hypothesis H is satisfied, then $(\Delta I_h(., u_h))$ is continuously convergent to the zero function in $H_0^1(\Omega)$.*

Proof. If $\phi \notin X_{1_h}$, then by definition, $\Delta I_h(\phi, u_h) = 0$. Hence, we need to consider only the case where $\phi \in X_{1_h}$. If $\phi \in X_{1_h}$, then from (4.2),

$$|\Delta I_h(\phi, u_h)| \leq C h_0^{n+1} \sum_i \int_{e_i} \{|D^{n+1}|\nabla\phi|^2| + C_1 h_0^{-n} |D(u_h^2 \phi)| + C_2 h_0^{-n} |D(\phi)|\} d\mathbf{r}.$$

If $(n-2k+3) > 0$, then $D^{n+1}|\nabla\phi|^2 = 0$. Hence,

$$\begin{aligned} |\Delta I_h(\phi, u_h)| &\leq C h_0 \sum_i \int_{e_i} |D(u_h^2\phi)| d\mathbf{r} + C_1 h_0 \sum_i \int_{e_i} |D(\phi)| d\mathbf{r} \\ &\leq C h_0 \{\|\nabla u_h\|_{L^2(\Omega)} \|u_h \phi\|_{L^2(\Omega)} + \|\nabla\phi\|_{L^2(\Omega)} \|u_h\|^2_{L^4(\Omega)}\} + C_1 h_0 \|\nabla\phi\|_{L^1(\Omega)} \\ &\leq C h_0 \{\|\nabla u_h\|_{L^2(\Omega)} \|u_h\|_{L^4(\Omega)} \|\phi\|_{L^4(\Omega)} + \|\nabla\phi\|_{L^2(\Omega)} (\|u_h\|^2_{L^4(\Omega)} + C_2)\}. \end{aligned} \tag{4.3}$$

As the hypothesis H is satisfied, $H_0^1(\Omega)$ and $W^{1,p}(\Omega)$ are compact injections into $L^4(\Omega)$ and all the norms make sense. As, $u_h \rightharpoonup u$ in X, it follows that norms $\|\nabla u_h\|_{L^2(\Omega)}$ and $\|u_h\|_{L^4(\Omega)}$ are uniformly bounded. Hence, it follows that $(\Delta I_h(., u_h))$ is continuously convergent to the zero function. □

Theorem 4.3.1. *If $(u_h) \in (X_h)$ is a sequence such that $u_h \rightharpoonup u$ in X, $(n-2k+3) > 0$, $p \geq 2$ and the hypothesis H is satisfied, then $\tilde{I}_h(., u_h) \rightharpoonup^{\Gamma} I(., u)$ in weak topology of $H_0^1(\Omega)$.*

Proof. $\tilde{I}_h(.,u_h) = I_h(.,u_h) + \Delta I_h(.,u_h)$. From Lemma 4.3.1, it follows that $(\Delta I_h(.,u_h))$ is continuously convergent to zero. Hence, from Prop. 6.20, Dal Maso (1993), it follows that $\tilde{I}_h(.,u_h) \rightharpoonup^{\Gamma} I(.,u)$ in weak topology of $H_0^1(\Omega)$. □

Theorem 4.3.2. *If $(u_h) \in (X_h)$ is a sequence such that $u_h \rightharpoonup u$ in X, $(n-2k+3) > 0$, $p \geq 2$, $N < 4$ and the hypothesis H is satisfied, then $\lim_{h\to\infty} \inf_{H_0^1(\Omega)} \tilde{I}_h(.,u_h) = \min_{H_0^1(\Omega)} I(.,u)$, i.e. $\lim_{h\to\infty} \tilde{J}_h(u_h) = J(u)$.*

Proof. To show this we need to show that $\tilde{I}_h$ is equi-coercive in the weak topology of $H_0^1(\Omega)$. For $\phi \in X_{1_h}$, from (4.1) and (4.3),

$$\begin{aligned}\tilde{I}_h(\phi,u_h) &\geq I_h(\phi,u_h) - Ch_0\{\|\nabla u_h\|_{L^2(\Omega)}\|u_h\|_{L^4(\Omega)}\|\phi\|_{L^4(\Omega)} + \|\nabla\phi\|_{L^2(\Omega)}(\|u_h\|^2_{L^4(\Omega)} + C_2)\} \\ &\geq C_1\|\phi\|^2_{H_0^1(\Omega)} - C_2\|\phi\|_{L^2(\Omega)} - C_3h_0\|\nabla\phi\|_{L^2(\Omega)} - C_4h_0\|\phi\|_{L^4(\Omega)}.\end{aligned}$$

Using Inverse Inequality, $\|\phi\|_{L^4(\Omega)} \leq Ch_0^{-N/4}\|\phi\|_{L^2(\Omega)}$. Hence, we have,

$$\tilde{I}_h(\phi,u_h) \geq C_1\|\phi\|^2_{H_0^1(\Omega)} - C_2\|\phi\|_{L^2(\Omega)} - C_3h_0\|\nabla\phi\|_{L^2(\Omega)} - Ch_0^{1-N/4}\|\phi\|_{L^2(\Omega)} \quad (C_1 > 0).$$

If $\phi \notin X_{1_h}$, then $\tilde{I}_h(\phi,u_h) = \infty$. Hence, for any ϕ we have,

$$\tilde{I}_h(\phi,u_h) \geq C_1\|\phi\|^2_{H_0^1(\Omega)} - C_2\|\phi\|_{L^2(\Omega)} - C_3h_0\|\nabla\phi\|_{L^2(\Omega)} - Ch_0^{1-N/4}\|\phi\|_{L^2(\Omega)} \quad (C_1 > 0).$$

As all the terms appearing with a negative sign are lower order, it follows that $\tilde{I}_h$ is equi-coercive in the weak topology of $H_0^1(\Omega)$. Hence, the result follows from Theorem 4.3.1 and Theorem 7.8, Dal Maso (1993). □

Returning to the energy functional, lets define,

$$\tilde{E}_h(u) = \begin{cases} \tilde{F}(u) + \tilde{G}(u) + \tilde{J}_h(u), & \text{if } u \in X_h; \\ +\infty, & \text{otherwise;} \end{cases}$$

If f is a polynomial function of degree d which satisfies the condition $n - d(k-1) \geq 0$ and $g^{'}(u) \in L^2(\Omega)$, then for $u \in X_h$, we have the error estimate for a quadrature of n^{th} order as,

$$|\tilde{E}_h(u) - E_h(u)| \leq C h_0^{n+1} \sum_i \int_{e_i} |D^{n+1}[f(\nabla u) + g(u)]| d\mathbf{r} + |\tilde{J}_h(u) - J_h(u)| \,.$$

If f is a polynomial function of degree d which satisfies the condition $n - d(k-1) \geq 0$, then $D^{n+1}(f(\nabla u)) = 0$. Hence,

$$\begin{aligned} |\tilde{E}_h(u) - E_h(u)| &\leq C h_0^{n+1} \sum_i \int_{e_i} |D^{n+1}(g(u))| d\mathbf{r} + |\tilde{J}_h(u) - J_h(u)| \\ &\leq C h_0 \|g^{'}(u)\|_{L^2(\Omega)} \|\nabla u\|_{L^2(\Omega)} + |\tilde{J}_h(u) - J_h(u)| \;\; (Inverse\ Inequality). \end{aligned} \tag{4.4}$$

Lets denote by hypothesis $H2$ the following conditions,

1. f is a polynomial function of degree d which satisfies the condition $n - d(k-1) \geq 0$.

2. If $(u_h) \in (X_h)$ is a sequence such that $u_h \rightharpoonup u$ in X, then $\|g^{'}(u_h)\|_{L^2(\Omega)}$ is bounded uniformly.

3. $N < 4$.

4. $n - 2k + 3 > 0$.

5. $p \geq 2$.

Lemma 4.3.2. *If $(u_h) \in (X_h)$ is a sequence such that $u_h \rightharpoonup u$ in X, and hypothesis H and*

*H*2 *are satisfied, then* $\lim_{h\to\infty}\{\tilde{E}_h(u_h) - E_h(u_h)\} = 0$.

Proof. Follows from (4.4), Theorem 4.2.2, and Theorem 4.3.2. □

Theorem 4.3.3. *If the hypothesis H and H*2 *are satisfied, then* $\tilde{E}_h \rightharpoonup^{\Gamma} E$ *in the weak topology of X.*

Proof. Let (u_h) be a sequence such that $u_h \rightharpoonup u$ in X. We then have 2 cases.

Case1: There is no sub-sequence (u_{h_k}) such that $(u_{h_k})\in X_{h_k}$

$\liminf_{h\to\infty} \tilde{E}_h(u_h) = +\infty$. Hence, $\liminf_{h\to\infty} \tilde{E}_h(u_h) \geq E(u)$.

Case2: $\exists$ sub-sequence (u_{h_k}) such that $(u_{h_k})\in X_{h_k}$

$\liminf_{h\to\infty} \tilde{E}_h(u_h) \geq \liminf_{h_k\to\infty} E_{h_k}(u_{h_k}) + \liminf_{h\to\infty} (\tilde{E}_{h_k} - E_{h_k})(u_{h_k})$ and by using Lemma 4.3.2 we get, $\liminf_{h\to\infty} (\tilde{E}_{h_k} - E_{h_k})(u_{h_k}) = 0$.

Hence, $\liminf_{h\to\infty} \tilde{E}_h(u_h) \geq \liminf_{h_k\to\infty} E_{h_k}(u_{h_k}) \geq E(u)$ (from Theorem 4.2.3).

Now we construct the recovery sequence from interpolated functions. Let (u_h) be a sequence constructed from the interpolation functions of successive triangulations such that, $u_h \to u$ in X. $\lim_{h\to\infty} \tilde{E}_h(u_h) = \lim_{h\to\infty} E_h(u_h) + \lim_{h\to\infty}(\tilde{E}_h - E_h)(u_h)$. But $\lim_{h\to\infty}(\tilde{E}_h - E_h)(u_h) = 0$ from Lemma 4.3.2. Hence, $\lim_{h\to\infty} \tilde{E}_h(u_h) = \lim_{h\to\infty} E_h(u_h) = E(u)$. Hence, $\tilde{E}_h \rightharpoonup^{\Gamma} E$ in weak topology of X. □

Lemma 4.3.3. *If f is a polynomial function of degree d which satisfies the condition* $n - d(k-1) \geq 0$, $p \geq 2$ *and* $N(\max\{0, \frac{p-1}{p} - \frac{1}{2}\}) < 1$ *then,* $\tilde{E}_h$ *is equi-coercive in the weak topology of X.*

Proof. First we note the following property about quadratures. If $A(u) = \int f(u)$, $B(u) = \int g(u)$ and $f(u(\mathbf{r})) \geq g(u(\mathbf{r}))$ on Ω, then $\tilde{A}(u) \geq \tilde{B}(u)$. Hence, if $u\in X_h$, as $J_h(u) \geq 0$ and

$q \geq p$ we have,

$$E_h(u) \geq \int_\Omega \{f(\nabla u) + C_1|u|^p - C_2\} d\mathbf{r}$$
$$\tilde{E}_h(u) \geq Q\{\int_\Omega \{f(\nabla u) + C_1|u|^p - C_2\} d\mathbf{r}\}$$

where Q denotes the quadrature of the term inside the bracket. Hence,

$$\begin{aligned}
\tilde{E}_h(u) &\geq \int_\Omega \{f(\nabla u) + C_1|u|^p\} d\mathbf{r} - Ch_0 \|u\|^{p-1}_{L^{(2p-2)}(\Omega)} \|\nabla u\|_{L^2(\Omega)} - C_2 \\
&\geq c_0 \|\nabla u\|^p_{L^p(\Omega)} + C_1 \|u\|^p_{L^p(\Omega)} - Ch_0 \|u\|^{p-1}_{L^{(2p-2)}(\Omega)} \|\nabla u\|_{L^2(\Omega)} - C_2 \\
&\geq c_0 \|\nabla u\|^p_{L^p(\Omega)} + C_1 \|u\|^p_{L^p(\Omega)} - Ch_0^{1-N(\max\{0, \frac{p-1}{p} - \frac{1}{2}\})} \|u\|^{(p-1)}_{L^p(\Omega)} \|\nabla u\|_{L^2(\Omega)} - C_2 \,.
\end{aligned}$$

As $N(\max\{0, \frac{p-1}{p} - \frac{1}{2}\}) < 1$, $\exists$ a m such that $\forall h > m$,

$$\tilde{E}_h(u) \geq K_0 \|\nabla u\|^p_{L^p(\Omega)} + K_1 \|u\|^p_{L^p(\Omega)} - K_2$$

where $K_0 > 0$, $K_1 > 0$, K_2 are constants independent of h. If $u \notin X_h$, then $\tilde{E}_h(u) = +\infty$. Thus, the above expression is true for any u. It is now straightforward to show that $(\tilde{E}_h)$ is equi-coercive in the weak topology of $W^{1,p}(\Omega)$ and, from Lemma 4.1.1, equi-coercive in the weak topology of X. □

Theorem 4.3.4. *If the hypothesis H and H2 are satisfied, and* $N(\max\{0, \frac{p-1}{p} - \frac{1}{2}\}) < 1$, *then* $\lim_{h\to\infty} \inf_X \tilde{E}_h = \min_X E$.

Proof. Follows from Lemma 4.3.3, Theorem 4.3.3, and Theorem 7.8, Dal Maso (1993). □

For the orbital-free energy functional, it is easy to check that it satisfies the following conditions:

1. f is a polynomial function of degree 2.

2. If $(u_h) \in (X_h)$, $u_h \rightharpoonup u$ in X, then $\|g^{'}(u_h)\|_{L^2(\Omega)}$ is uniformly bounded, which follows from the continuity of $g^{'}$ and compact injection of X in $L^{2q-2}(\Omega)$.

3. $N(\max\{0, \frac{p-1}{p} - \frac{1}{2}\}) < 1$ (as $N = 3$, $p = 2$).

Hence, if we choose an appropriate quadrature rule, all the results in this section will carry over to the orbital-free energy functional under consideration. We note that for linear shape functions a zero-order quadrature rule is sufficient for all the results in this section to carry over. However for quadratic shape functions a second-order accurate quadrature rule is necessary.

In Section 3.3, we noted that the finite-element discretization of the formulation was implemented with linear shape functions using a second order accurate quadrature rule. This quadrature rule satisfies the hypothesis $H2$, and thus we have rigorously established the convergence of our discretization scheme.

Chapter 5

Quasi-continuum orbital-free density-functional theory

The real-space formulation of orbital-free density-functional theory and the finite-element discretization of the formulation described in Chapter 3 is attractive, as it gives freedom from periodicity, which is important in modelling defects in materials. However, simulations on 9x9x9 aluminum cluster containing 3730 atoms took 10,000 CPU hours of computing. This fact is very disappointing, but not surprising. Not surprising, because this is the computational complexity of all electronic structure calculations. However it is disappointing, because materials properties are influenced by defects—vacancies, dopants, dislocations, cracks, free surfaces—in small concentrations (parts per million). An accurate understanding of such defects must not only include the electronic structure of the core of the defect, but also the elastic and electrostatic effects on the macro-scale. This in turn requires calculations involving millions of atoms well beyond the current capability. This chapter describes a seamless multi-scale scheme to overcome this significant hurdle.

We present a method for *seamlessly* coarse-graining OFDFT that effectively overcomes the present limitations without the introduction of spurious physics and at no significant loss of accuracy. We refer to the approximation scheme as *Quasi-Continuum Orbital-Free Density-Functional Theory (QC-OFDFT)*. It is similar in spirit to the quasi-continuum ap-

proach developed in the context of interatomic potentials (cf, e. g., Tadmor et al. (1996); Knap & Ortiz (2001)) as a scheme to seamlessly bridge the atomistic and continuum length scales. This bridging is achieved by adaptively selecting representative atoms and interpolating the positions of other atoms using finite-element shape functions. The energy thus becomes a function of the representative atom-coordinates only. As a further approximation, cluster summation rules are introduced in order to avoid full lattice sums when computing the effective forces on the representative atoms. With increasing number of representative nodes and cluster sizes, the scheme converges at the expected theoretical convergence rate of finite-element approximation (Knap & Ortiz, 2001).

A local version of the quasi-continuum approach based on the Cauchy-Born hypothesis has recently been developed for density-functional theory (Fago et al., 2004). The Cauchy-Born hypothesis finds formal justification in a theorem of Blanc et al. (2002) for deformation fields that slowly vary with respect to the length scale of the lattice parameter, but breaks down close to defect cores. In the context of DFT, the conventional QC reduction scheme can be applied *mutatis mutandis* to describe the positions of the nuclei. However, the electron-density and electrostatic potential exhibit subatomic structure as well as lattice scale modulation, and therefore require an altogether different type of representation.

The QC-OFDFT method we introduce here has three important elements. First, we formulate the OFDFT including all the electrostatic interactions in real-space, as described in Chapter 3. Second, we implement this formulation using a finite-element method with two nested discretizations, an atomistic mesh that describes the atomic degrees of freedom and an electronic mesh that describes the electronic degrees of freedom. Importantly, information about subatomic electronic states are preserved either implicitly or explicitly at each point in the material. Third, we adaptively refine the discretization where we need

more resolution, while retaining a coarse description where that suffices. This refinement is completely unstructured and guided solely by the problem with no *a priori* restrictions (like periodicity).

We demonstrate our method by studying mono-vacancies and di-vacancies in aluminum crystals consisting of a million atoms. We restrict our treatment of the orbital-free kinetic energy functionals to the Thomas-Fermi-Weizsacker functionals (Parr & Yang, 1989). We demonstrate in the Appendix that our approach may be extended to the more recent and accurate non-local kernel functionals (Wang et al., 1998, 1999; Smargiassi & Madden, 1994; Wang & Teter, 1992).

For a mono-vacancy, we show by a convergence analysis that the electron-density field can be obtained everywhere with negligible error and through modest computational means. Our results are close to the experimentally observed values, and provide insights into the electronic structure at the core. At the same time, our results show that atomistic displacement fields decay over very large distances, underscoring the long-range nature of the underlying physics. This is significant for two reasons. First, it shows that long-range interactions beyond those considered in previous calculations (Wang et al., 1998, 1999; Gillian, 1989; Mehl & Klein, 1991; Chetty et al., 1995; Turner et al., 1997) are important. Second, it shows that errors previously attributed to the approximations of OFDFT may in fact be an artifact of small periodic computational cells.

The remainder of the chapter is organized as follows. Section 5.1 describes the key ideas associated with the quasi-continuum reduction and coarse-graining of orbital-free density-functional theory. The expressions for the generalized forces corresponding to the formulation are derived in Section 5.2. Section 5.3 describes the details of numerical implementation, and Section 5.4 reports studies on a mono-vacancy in aluminum.

5.1 Quasi-continuum reduction

The problem of determining the ground-state electron-density and the equilibrium positions of the nuclei using a finite-element discretization was described in Chapter 3 by (3.23) as,

$$\inf_{u^h \in X_h,\ \mathbf{R}\in\mathbb{R}^{3M}} E(u^h, \mathbf{R}) \tag{5.1a}$$

$$\text{subject to:} \qquad \int_\Omega (u^h(\mathbf{r}))^2 d\mathbf{r} = N \tag{5.1b}$$

$$E(u^h, \mathbf{R}) = \sup_{\phi^h \in X_h} L(u^h, \mathbf{R}, \phi^h). \tag{5.1c}$$

We introduce three unstructured triangulations of the domain, as shown in Figure 5.1, to provide a complete description of the discrete fields: i) a triangulation T_{h_1} of selected representative atoms in the usual manner of QC, which we refer to as the *atomic-mesh*; ii) an everywhere subatomic triangulation T_{h_2} of the domain that captures the subatomic oscillations in the electron-density and potential, which we refer to as the *fine-mesh*; and iii) a triangulation T_{h_3} subatomic close to lattice defects and increasingly coarser away from the defects, which we refer to as the *electronic-mesh*. We restrict the triangulations in such a way that T_{h_3} is a sub-grid of T_{h_1} and T_{h_2} a sub-grid of T_{h_3}. We additionally denote by X_{h_1}, X_{h_2}, and X_{h_3} the corresponding finite-element approximation spaces.

The full square-root electron-density and electrostatic potential are written as

$$u^h = u_0^h + u_c^h\,, \tag{5.2a}$$

$$\phi^h = \phi_0^h + \phi_c^h\,, \tag{5.2b}$$

where $u_0^h \in X_{h_2}$ and $\phi_0^h \in X_{h_2}$ are the predictors for square-root electron-density and

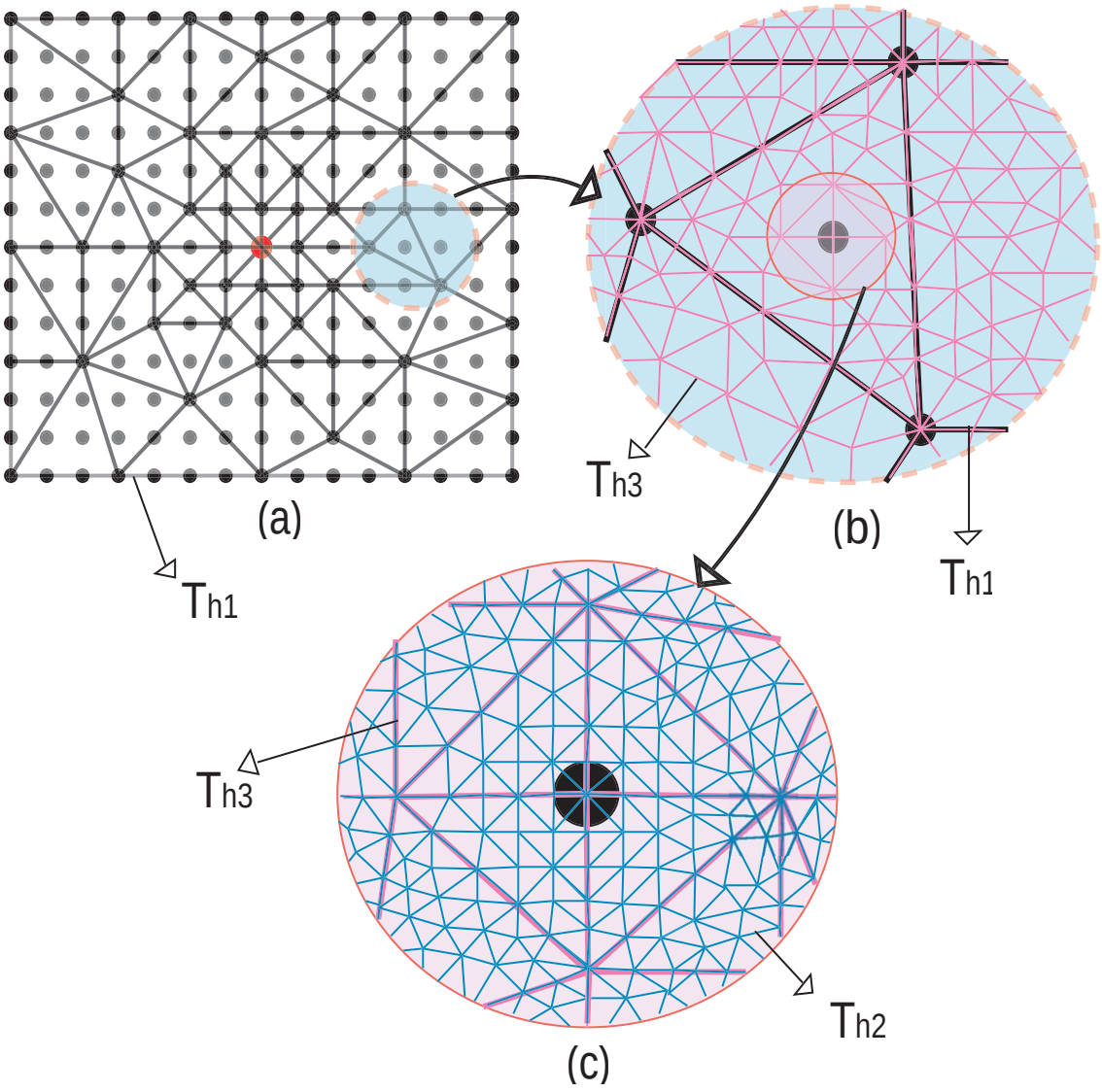

Figure 5.1: Schematic sketch of meshes: (a) shows the triangulation of the lattice sites, T_{h_1} (*atomic-mesh*), where the mesh coarse-grains away from the vacancy (depicted by the red dot); (b) shows the triangulation, T_{h_3} (*electronic-mesh*), which is used to solve for the corrections to the predictor of electronic fields; (c) shows the triangulation, T_{h_2} (*fine-mesh*), on which the predictor for electronic fields is computed. Both triangulations T_{h_1} and T_{h_3} coarse-grain away from vacancy, whereas T_{h_2} is a uniform triangulation.

electrostatic potential obtained by performing a local periodic calculation in every element of T_{h_1}. $u_c^h \in X_{h_3}$ and $\phi_c^h \in X_{h_3}$ are the *non-local* corrections to be solved for. The predictor for the electronic fields is expected to be accurate away from defect cores, in regions where the deformation field is slowly varying (Blanc et al., 2002). Hence, the non-local corrections may be accurately represented by means of a finite-element triangulation such as T_{h_3}, namely, a triangulation that has subatomic resolution close to the defect and coarsens away from the defect to become superatomic.

The minimization problem given by (5.1) now reduces to a minimization problem for the non-local corrections and takes the form

$$\inf_{u_c^h \in X_{h_3},\ \mathbf{R} \in X_{h_1}} E(u_0^h + u_c^h, \mathbf{R}) \tag{5.3a}$$

$$\text{subject to:} \qquad \int_\Omega (u_0^h(\mathbf{r}) + u_c^h(\mathbf{r}))^2 d\mathbf{r} = N \tag{5.3b}$$

$$E(u_0^h + u_c^h, \mathbf{R}) = \sup_{\phi_c^h \in X_{h_3}} L(u_0^h + u_c^h, \mathbf{R}, \phi_0^h + \phi_c^h). \tag{5.3c}$$

In order to compute the predictor for electronic fields, we begin by performing a periodic calculation in every element of T_{h_1}. The resulting fields are not necessarily continuous at the boundaries of the elements of T_{h_1}. We overcome this deficiency and obtain conforming (continuous) fields u_0^h and ϕ_0^h over T_{h_2} by performing an $L^2 \to H^1$ map. To define this mapping, denote by $\sigma_{0,k}$ the k^{th} node of the triangulation T_{h_2}. As T_{h_2} is a sub-grid of T_{h_1}, define an index set I_k which collects the element numbers of triangulation T_{h_1} to which the node $\sigma_{0,k}$ belongs. The map can now be defined as

$$U_0^k = \frac{1}{\#I_k} \sum_{j \in I_k} \tilde{U}_j(\mathbf{r}_k) \qquad k = 1, \ldots, n_2 \tag{5.4}$$

where n_2 denotes the total number of nodes in T_{h_2}, U_0^k is the value of the conforming field at the k^{th} node, $\#I_k$ denotes the cardinality of the index set, and $\tilde{U}_j(\mathbf{r}_k)$ is the value of the field at the k^{th} node computed from a periodic calculation in element $e_j \in T_{h_1}$. Note that this is simply the average value at a node of fields obtained from periodic calculations in the different elements.

Since the predictor for electronic fields is defined on the uniformly subatomic mesh T_{h_2}, it would appear that the computation of the system corresponding to the reduced problem (5.3) has complexity commensurate with the size of T_{h_2}, which would render the scheme infeasible. In the spirit of quadrature rules in finite-elements (e.g., Ciarlet (2002); Brenner & Scott (2002)), or summation rules in QC (Knap & Ortiz, 2001), we proceed to introduce integration rules that reduce all computations to the complexity of T_{h_3}. The precise form of the integration rule for an element e in the triangulation T_{h_3} is

$$\int_e f(\mathbf{r})d\mathbf{r} \approx |e|\langle f\rangle_{D_e} \tag{5.5}$$

where $|e|$ is the volume of element e, D_e is the unit cell of an atom if such cell is contained in e or e otherwise, and $\langle f\rangle_{D_e}$ is the average of f over D_e. Using (5.5), integration over the entire domain can be written as,

$$\int_\Omega f(\mathbf{r})d\mathbf{r} = \sum_{e\in T_{h_3}} \int_e f(\mathbf{r})d\mathbf{r} \approx \sum_{e\in T_{h_3}} |e|\langle f\rangle_{D_e} \ , \tag{5.6}$$

reducing all computations to a complexity commensurate with the size of T_{h_3}.

The integration rule (5.5) is designed to exploit the nature of the solution. As mentioned previously, the predictor for electronic fields is expected to be accurate away from defect cores where the deformation field is slowly varying. By way of construction of the meshes,

this region also corresponds to large, superatomic elements of T_{h_3}, where the computed non-local corrections are very small compared to the predictor. Thus, the integrand of equation (5.5) is a rapidly oscillating function with a very gradual modulation on the scale of the element. Hence, equation (5.5), for regions away from the core of a defect, denotes the zero-order quadrature rule for rapidly oscillating functions. For regions close to a defect, the computed corrections to the predictor are large and thus the integration must be performed exactly. The integration rule (5.5) is consistent with this requirement, as the elements of T_{h_3} close to a defect are subatomic and the integration rule is exact for these elements.

Equations (5.3)-(5.5) describe the QC-OFDFT method.

5.2 Forces

We solve the variational problem (5.3) using conjugate gradients. This requires the calculation of generalized nodal forces, defined as the variation of the total energy with respect to ϕ_c^h (correction to electrostatic potential), u_c^h (correction to electron-density), as well as the configurational forces defined as the variation of the total energy with respect to the nodal positions. The nodal forces associated with ϕ_c^h and u_c^h are defined on triangulation T_{h_3} and the configurational forces of the nuclei are defined on T_{h_1}.

The energy functional corresponding to orbital-free density-functional theory can be succinctly represented as

$$E(u^h, \mathbf{R}, \phi^h) = \int_\Omega f(u^h, \nabla u^h) d\Omega + \int_\Omega ((u^h)^2 + \sum_i Z_i b_i)\phi^h \, d\Omega - \frac{1}{8\pi} \int_\Omega |\nabla \phi^h|^2 \, d\Omega \,, \quad (5.7)$$

where b_i denotes a regularized nuclear charge with charge Z_i on the i^{th} node. The nodal forces f_ϕ^k and f_u^k corresponding to ϕ_c^h and u_c^h respectively at the k^{th} node of triangulation

T_{h_3} are given by

$$f_\phi^k(u^h, \mathbf{R}, \phi^h) = \frac{\delta E(u^h, \mathbf{R}, \phi^h)}{\delta \phi^h_{c_k}} \tag{5.8a}$$

$$f_u^k(u^h, \mathbf{R}, \phi^h) = \frac{\delta E(u^h, \mathbf{R}, \phi^h)}{\delta u^h_{c_k}}\,. \tag{5.8b}$$

Though these are defined on the nodes of triangulation T_{h_3}, they have to be evaluated using quantities defined on the finer mesh T_{h_2} by taking advantage of the fact that T_{h_2} is a sub-grid of T_{h_3}, and the finite-element shape-functions are linear. By definition,

$$f_\phi^k(u^h, \mathbf{R}, \phi^h) = \int_\Omega ((u^h)^2 + \sum_i Z_i b_i) N_k^{h_3}\, d\Omega - \frac{1}{4\pi}\int_\Omega \nabla\phi^h.\nabla N_k^{h_3}\, d\Omega \tag{5.9}$$

where $N_k^{h_3}$ denotes the shape function associated with node k of triangulation T_{h_3}. As the shape functions are linear and T_{h_2} is a sub-grid of T_{h_3}, $N_k^{h_3}(\mathbf{r}) = \sum_{a\in T_{h_2}} N_k^{h_3}(\mathbf{a}) N_a^{h_2}(\mathbf{r})$, where a denotes a node in T_{h_2} and $N_a^{h_2}$ denotes the shape function associated with node a of triangulation T_{h_2}. Hence the expression for the nodal force given in equation (5.9) can be rewritten as

$$\begin{aligned} f_\phi^k(u^h, \mathbf{R}, \phi^h) &= \sum_{a\in T_{h_2}} N_k^{h_3}(\mathbf{a})\{\int_\Omega ((u^h)^2 + \sum_i Z_i b_i) N_a^{h_2}\, d\Omega - \frac{1}{4\pi}\int_\Omega \nabla\phi^h.\nabla N_a^{h_2}\, d\Omega\} \\ &= \sum_{a\in T_{h_2}} N_k^{h_3}(\mathbf{a}) f_\phi^{0^a}(u^h, \mathbf{R}, \phi^h)\,, \end{aligned} \tag{5.10}$$

where $f_\phi^{0^a}$ denotes the nodal force associated with ϕ^h on node a of triangulation T_{h_2}. We proceed similarly for f_ϕ^u.

Taking into account the cluster rules, defined by equation (5.5), we obtain the expressions

for the generalized nodal forces:

$$f_\phi^k(u^h, \mathbf{R}, \phi^h) = \sum_{e \in T_{h_3}} \{C_e \sum_{a \in D_e}{}' f_\phi^{0^a}(u^h, \mathbf{R}, \phi^h) N_k^{h_3}(\mathbf{a})\} \qquad k = 1, \ldots, n_3\,, \tag{5.11a}$$

$$f_u^k(u^h, \mathbf{R}, \phi^h) = \sum_{e \in T_{h_3}} \{C_e \sum_{a \in D_e}{}' f_u^{0^a}(u^h, \mathbf{R}, \phi^h) N_k^{h_3}(\mathbf{a})\} \qquad k = 1, \ldots, n_3, \tag{5.11b}$$

where $f_\phi^{0^a}$ and $f_u^{0^a}$ are the nodal forces associated with ϕ^h and u^h on node a of triangulation T_{h_2}; $N_k^{h_3}(\mathbf{a})$ denotes the value of the shape function associated with node k of T_{h_3} at the position of node a; C_e is a constant whose value is 1 if $D_e = e$, $\frac{|e|}{|D_e|}$ otherwise; n_3 denotes the total number of nodes in T_{h_3}; and $'$ over summation avoids double counting. Forces f_ϕ^0 and f_u^0 corresponding to ϕ^h and u^h, which are defined on T_{h_2}, are computed using standard routines for force calculations with finite-element basis.

We now turn to the configurational forces associated with the positions of the nuclei. Though these appear to be non-local at first glance, we show that they can in fact be evaluated locally. The derivation closely follows Thoutireddy (2002) and is based on ideas widely used in Mechanics following Eshelby's formulation of force on a defect (Eshelby, 1951).

For clarity of presentation, we begin with a single finite element triangulation (rather than the three considered here). In this situation, the total energy is $I_1^h + I_2^h + I_3^h$ where

$$\begin{aligned} I_1^h &= \int_\Omega f(u^h, \nabla u^h) d\Omega, \\ I_2^h &= \int_\Omega ((u^h)^2 + \sum_i Z_i b_i)\phi^h d\Omega, \\ I_3^h &= -\frac{1}{8\pi} \int_\Omega |\nabla \phi^h|^2 \, d\Omega, \end{aligned}$$

and $u^h, \phi^h \in X_h$. Note that

$$I_1^h = \int_\Omega f(u^h, \nabla u^h) d\Omega = \sum_{e \in T_h} \int_{\hat{\Omega}} f(u^h, \nabla u^h) \det \left(\frac{\partial X_M}{\partial \hat{X}_N} \right) d\hat{\Omega}$$

where $\hat{\Omega}$ is the reference volume in isoparametric formulation and $\frac{\partial X_M}{\partial \hat{X}_N}$ is the jacobian of transformation. Taking variations of I_1 with respect to X_h, we have

$$\begin{aligned}
\delta I_1^h &= \sum_{e \in T_h} \int_{\hat{\Omega}} \left\{ -\frac{\delta f}{\delta u_{,J}} \left[\sum_{a=1}^n u_a \hat{N}_{a,A} \frac{\partial \hat{X}_A}{\partial X_K} (\sum_{b=1}^n \delta X_{bK}^e \hat{N}_{b,B}) \frac{\partial \hat{X}_B}{\partial X_J} \right] \right. \\
&\qquad \left. + f(u^h, \nabla u^h) (\sum_{b=1}^n \delta X_{bK}^e \hat{N}_{b,B}) \frac{\partial \hat{X}_B}{\partial X_K} \right\} \det \left(\frac{\partial X_M}{\partial \hat{X}_N} \right) d\hat{\Omega} \\
&= \sum_{e \in T_h} \int_{\Omega^e} \left\{ -\frac{\delta f}{\delta u_{,J}} \left[\sum_{a=1}^n u_a N_{a,K} \right] + f(u^h, \nabla u^h) \delta_{KJ} \right\} \left(\sum_{b=1}^n \delta X_{bK}^e N_{b,J} \right) d\Omega \\
&= \sum_{e \in T_h} \int_{\Omega^e} \left\{ -\frac{\delta f}{\delta u_{,J}} (u^h, \nabla u^h) u_{,K}^h + f(u^h, \nabla u^h) \delta_{KJ} \right\} \left(\sum_{b=1}^n \delta X_{bK}^e N_{b,J} \right) d\Omega \ .
\end{aligned}$$

Similarly, note that

$$I_2^h = \int_\Omega \left((u^h)^2 + \sum_i Z_i b_i \right) \phi^h d\Omega = \sum_{e \in T_h} \int_{\hat{\Omega}} \left((u^h)^2 + \sum_{b=1}^n Z_b b_b \right) \phi^h \det \left(\frac{\partial X_M}{\partial \hat{X}_N} \right) d\hat{\Omega} \ .$$

Taking variations, we find

$$\begin{aligned}
\delta I_2^h &= \sum_{e \in T_h} \int_{\hat{\Omega}} \left((u^h)^2 \phi^h + \sum_{i=1}^n Z_i b_i \phi^h \right) \left(\sum_{b=1}^n \delta X_{bK}^e \hat{N}_{b,B} \right) \frac{\partial \hat{X}_B}{\partial X_K} \det \left(\frac{\partial X_M}{\partial \hat{X}_N} \right) d\hat{\Omega} \\
&\quad + \sum_{e \in T_h} \int_{\hat{\Omega}} \sum_{b=1}^n Z_b b_b (\delta \phi^h) \det \left(\frac{\partial X_M}{\partial \hat{X}_N} \right) d\hat{\Omega} \\
&= \sum_{e \in T_h} \int_{\Omega^e} \left((u^h)^2 \phi^h + \sum_{i=1}^n Z_i b_i \phi^h \right) \delta_{KJ} \left(\sum_{b=1}^n \delta X_{bK}^e N_{b,J} \right) d\Omega \\
&\quad + \sum_{e \in T_h} \int_{\Omega^e} \sum_{b=1}^n Z_b b_b \left(\sum_{a=1}^n \phi_a N_{a,K} \right) \delta X_{bK}^e d\Omega \ .
\end{aligned}$$

Similarly,

$$\delta I_3^h \;=\; -\frac{1}{8\pi}\sum_{e\in T_h}\int_{\Omega^e}\left\{|\nabla\phi^h|^2\delta_{KJ}-2\phi^h_{,J}\phi^h_{,K}\right\}\left(\sum_{b=1}^{n}\delta X^e_{bK}N_{b,J}\right)d\Omega\ .$$

Collecting all terms, the configurational force on node b along the K^{th} direction is given by

$$f_X^{bK}=\sum_{e\in T_h}\int_{\Omega^e}\mathrm{E}_{KJ}N_{b,J}d\Omega+\sum_{e\in T_h}\int_{\Omega^e}Z_b b_b\left(\sum_{a=1}^{n}\phi_a N_{a,K}\right)d\Omega\,, \tag{5.12}$$

where

$$\mathrm{E}_{KJ}=\left\{f+((u^h)^2+\sum_i Z_i b_i)\phi^h-\frac{1}{8\pi}|\nabla\phi^h|^2\right\}\delta_{KJ}-\frac{\delta f}{\delta u_{,J}}(u^h,\nabla u^h)u^h_{,K}+\frac{1}{4\pi}\phi^h_{,J}\phi^h_{,K}\}\,.$$

Note that this expression is *local*.

We can generalize these calculations to our situation with three nested triangulations and cluster rules. We find that the configurational forces on node j of triangulation T_{h_1} in the I^{th} direction is given by

$$f_X^{jI}(u^h,\mathbf{R},\phi^h)=\sum_{e_1\in T_{h_1}}\sum_{\substack{e_2\in e_1\\ e_2\in T_{h_3}}}\{C_{e_2}\sum_{a\in D_{e_2}}{}'\, f_X^{0^{aI}}(u^h,\mathbf{R},\phi^h)N_j^{h_1}(\mathbf{a})\}$$
$$j=1,\ldots,n_1,\quad I=1,2,3 \tag{5.13}$$

where $f_X^{0^{aI}}$ is the configurational forces on node a of triangulation T_{h_2} in the I^{th} direction given by (5.12), and $N_j^{h_1}(\mathbf{a})$ denotes the value of the shape function associated with node j of T_{h_1} at the position of node a. Once again, this expression is local.

5.3 Numerical implementation

We now turn to the numerical implementation of the QC-OFDFT scheme proposed. Triangulation T_{h_1} is obtained by a Delaunay triangulation of the lattice. The representative atoms are chosen *a priori* such that the triangulation is atomistic close to the region of interest and coarsens away as shown in Figure 5.2. Triangulations T_{h_2} and T_{h_3} are obtained from T_{h_1} using Fruedenthal's subdivision algorithm (Bey, 2000). This ensures that T_{h_2} and T_{h_3} are sub-grids of T_{h_1}. The subdivisions are performed such that T_{h_2} is subatomic everywhere but T_{h_3} is subatomic close to the region of interest and superatomic away from the region of interest, cf Figure 5.3. All triangulations consist of 4-node tetrahedral elements and the integrals are evaluated numerically using 4-point gaussian quadrature rules. The nodal forces and configurational forces computed in section (5.2) are equilibrated in a staggered scheme using non-linear conjugate gradients with secant method for line search. Finally, we implement the computation in parallel using domain decomposition.

5.4 Mono-vacancy in aluminum

We study a mono-vacancy in aluminum as the test case for the proposed method. Vacancies are an ideal test case as they often are dilute, and both the electronic core and long-range elastic interactions are important. Also, vacancy calculations are often treated as a benchmark to test various kinetic energy functionals (Wang et al., 1998, 1999). We use the QC-OFDFT approach to investigate into a mono-vacancy in aluminum. Thomas-Fermi-Weizsacker family of functionals with $\lambda = 1/6$ is used for the orbital-free kinetic energy functional. All simulations are performed using a modified form of Heine-Abarenkov pseudopotential for aluminum (Goodwin et al., 1990) and LDA treatment of exchange and

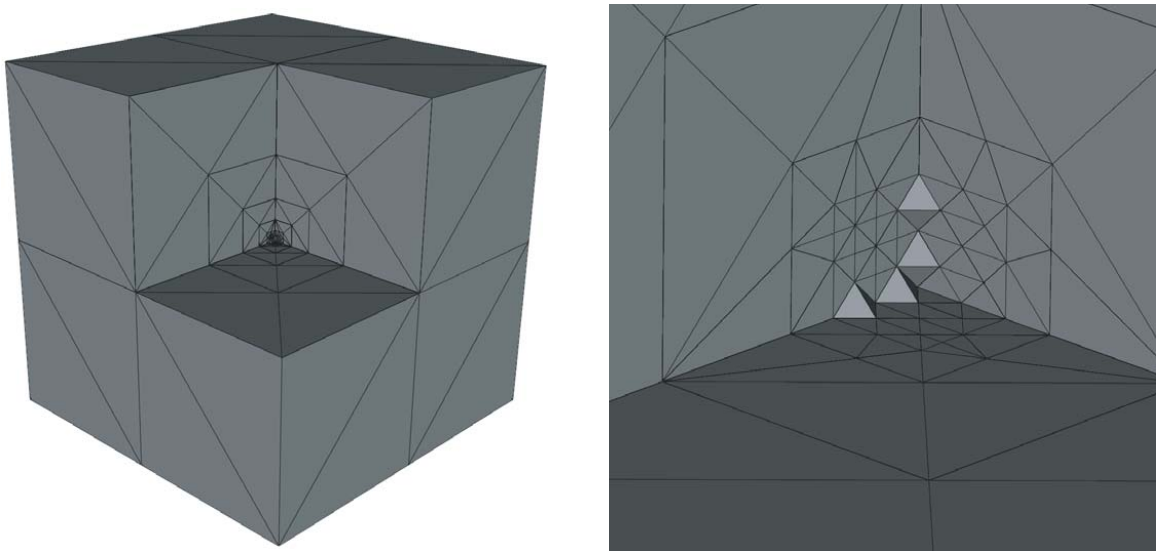

Figure 5.2: (a) Surface mesh of a sliced cubical domain corresponding to triangulation T_{h_1}; (b) Close up of (a)

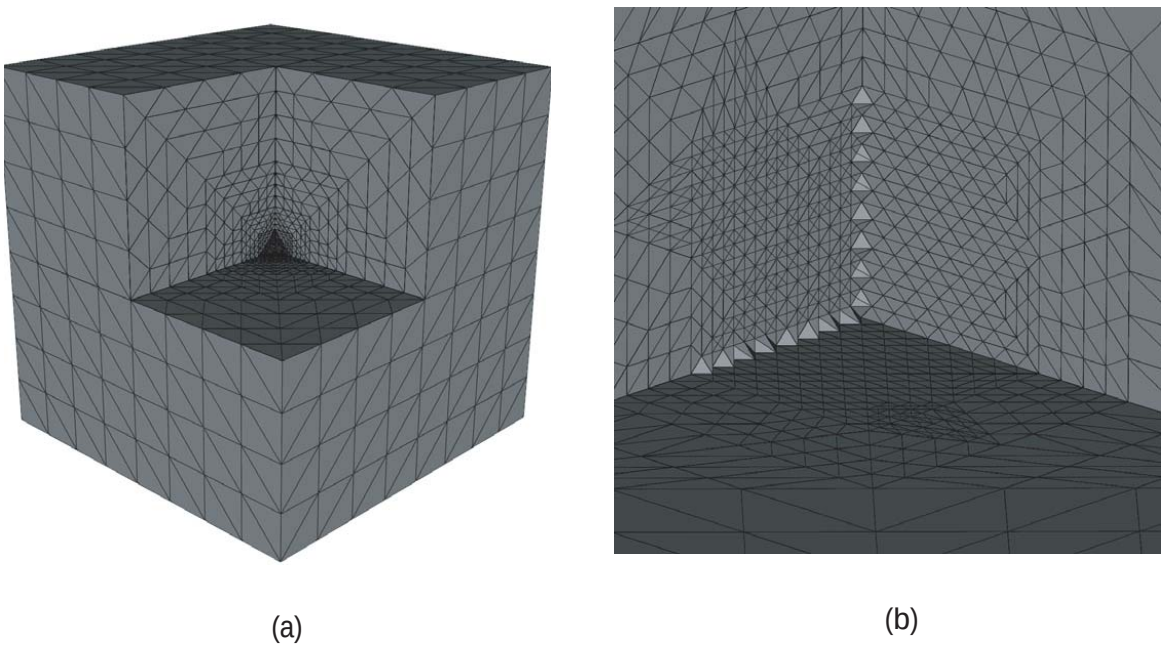

Figure 5.3: (a) Surface mesh of a sliced cubical domain corresponding to triangulation T_{h_3}; (b) Close up of (a)

correlation functionals (Ceperley & Alder, 1980; Perdew & Zunger, 1981).

We consider a sample with a single vacancy subjected to Dirichlet boundary conditions, which implies that all fields approach the bulk values at the boundary. We repeat our calculations for samples of varying sizes, namely, samples nominally containing 4, 32, 256, 2,048, 16,384, and one million (1048576) atoms.

The coarse-graining inherent in our approach means that we use far fewer representative atoms in the calculations. Figure 5.4 emphasizes the dramatic savings that this coarse-graining offers. It shows the vacancy formation energy of a sample containing 16,384 nominal atoms. As is evident from the figure, the calculations converge ostensibly beyond around 200 representative atoms, i.e., at an 80-fold computational savings. These savings improve with size and enable the consideration of large samples at modest computational expense.

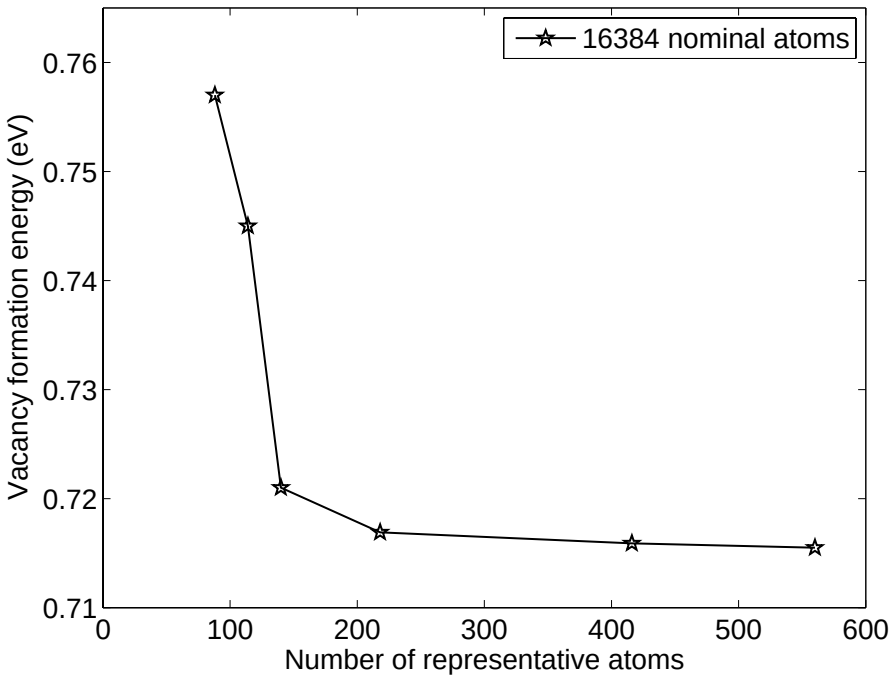

Figure 5.4: Convergence of the vacancy formation energy with number of representative atoms

We now describe the results of a simulation concerned with a million-atom sample performed with 1,017 representative atoms and in the order of 450,000 elements in the *electronic-mesh*. The calculations take about twelve hours on forty-eight 700 MHz Alpha processors. By an extrapolation of the convergence analysis just described, we estimate the error in vacancy formation energy due to coarse-graining to be less than 0.01 eV. Figures 5.5 and 5.6 show the contours of the ground-state electron-density around the vacancy, while Figures 5.7 - 5.10 show the contours of the electron-density correction (i. e., the difference between the ground-state electron-density and the predictor estimate). Compared to the predictor estimate, one sees a large correction close to the defect. As expected, there is a depletion in the electron-density at the vacancy, and a small augmentation in the atoms surrounding the vacancy is also evident, cf Figures 5.8 and 5.10. The vacancy formation energy is computed to be 0.72 eV, which compares well with the experimentally measured value of 0.66 eV (Triftshauser, 1975).

Figures 5.11 - 5.13 show the computed variation of the vacancy formation energy with sample size. This variation is reported for two sets of calculations: one where the atomic positions are held fixed (unrelaxed) in their nominal position, and a second where the atomic positions are relaxed. The vacancy formation energy is found to follow a power law close to $n^{-0.5}$ in the unrelaxed case and $n^{-0.55}$ in the relaxed case, where n is the nominal number of atoms in the sample. This power-law behavior is an indication of the long-range nature of the underlying physics. It is interesting to note that relaxation of the atomic positions reduces the vacancy formation energy by 0.06 eV.

Figures 5.14 - 5.16 shows the radial displacement fields along $\langle 100 \rangle$ and $\langle 110 \rangle$ directions. The fields have a long tail, another indication of the long-range nature of the field of the vacancy. The maximum displacement occurs in the $\langle 110 \rangle$ direction and amounts to 0.6% of

the nearest atom distance. This value is less than predicted in previous calculations using Kohn-Sham DFT with periodic boundary conditions, where the maximum displacement was estimated to be 1-2% of the nearest atom distance (Mehl & Klein, 1991; Chetty et al., 1995; Turner et al., 1997). At this point there is no basis to decide whether the discrepancy is due to the orbital-free formulation or the use of periodic boundary conditions.

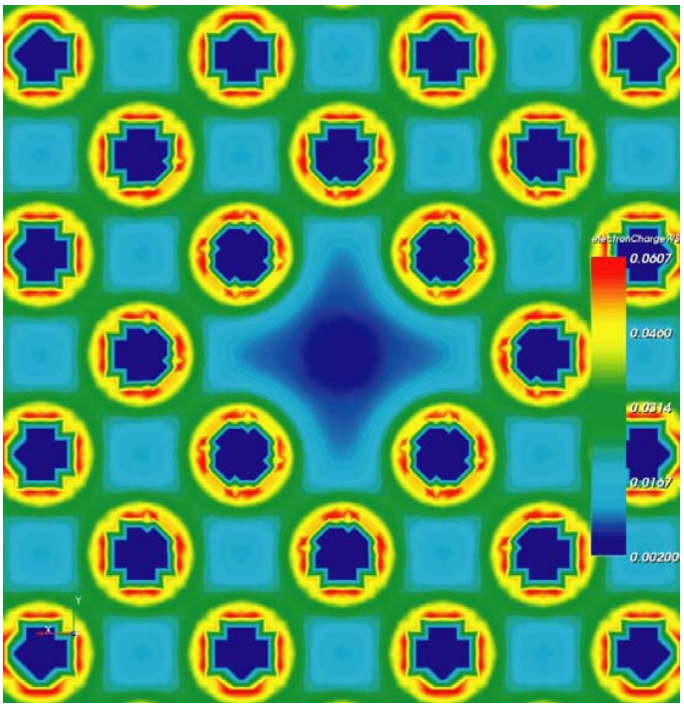

Figure 5.5: Contours of ground-state electron-density around the vacancy on (100) plane

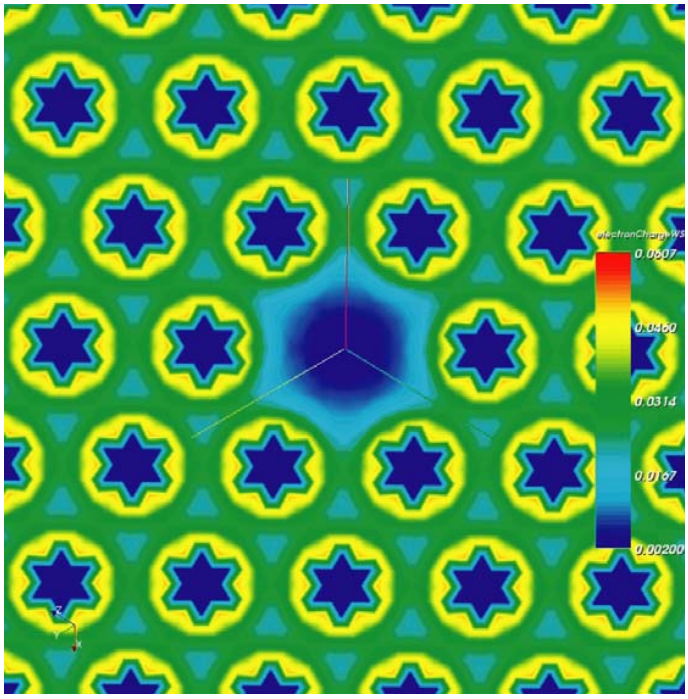

Figure 5.6: Contours of ground-state electron-density around the vacancy on (100) plane

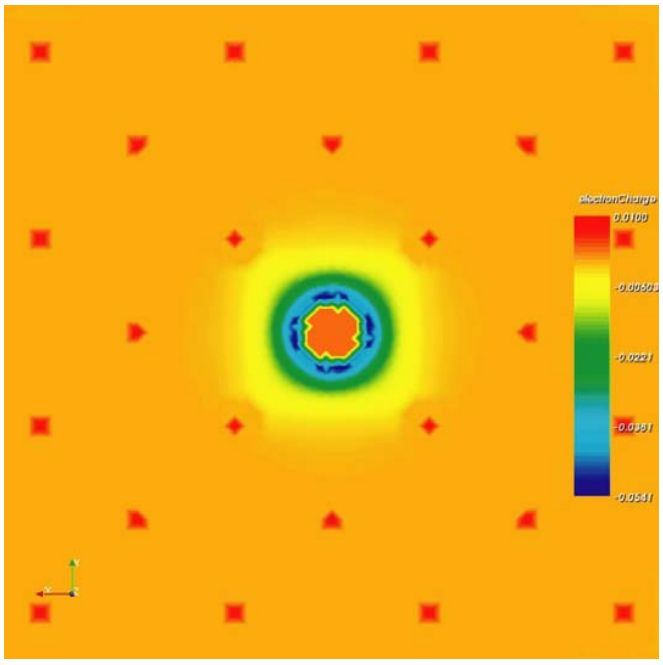

Figure 5.7: Contours of electron-density correction around the vacancy on (100) plane

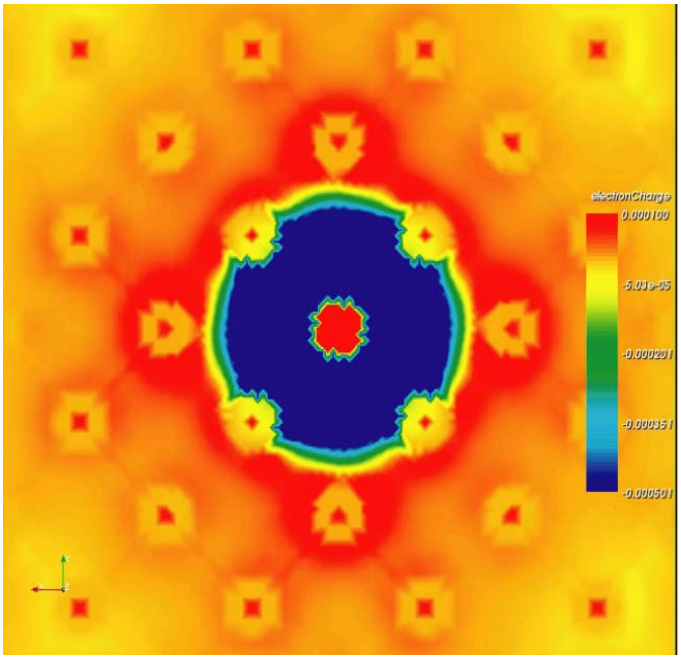

Figure 5.8: Contours of electron-density correction around the vacancy on (100) plane (smaller range)

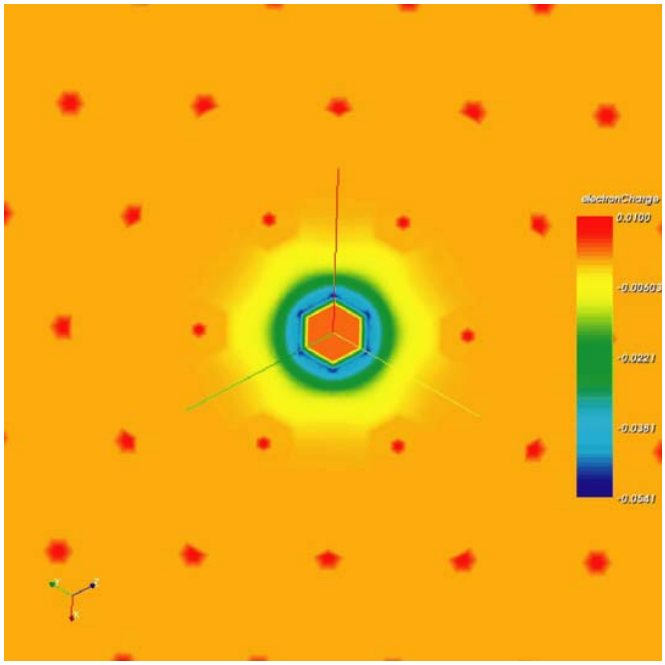

Figure 5.9: Contours of electron-density correction around the vacancy on (111) plane

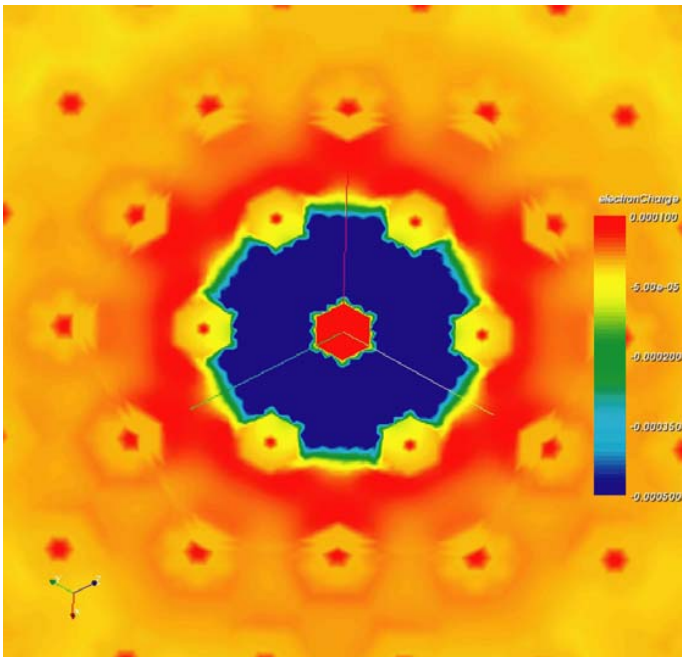

Figure 5.10: Contours of electron-density correction around the vacancy on (111) plane (smaller range)

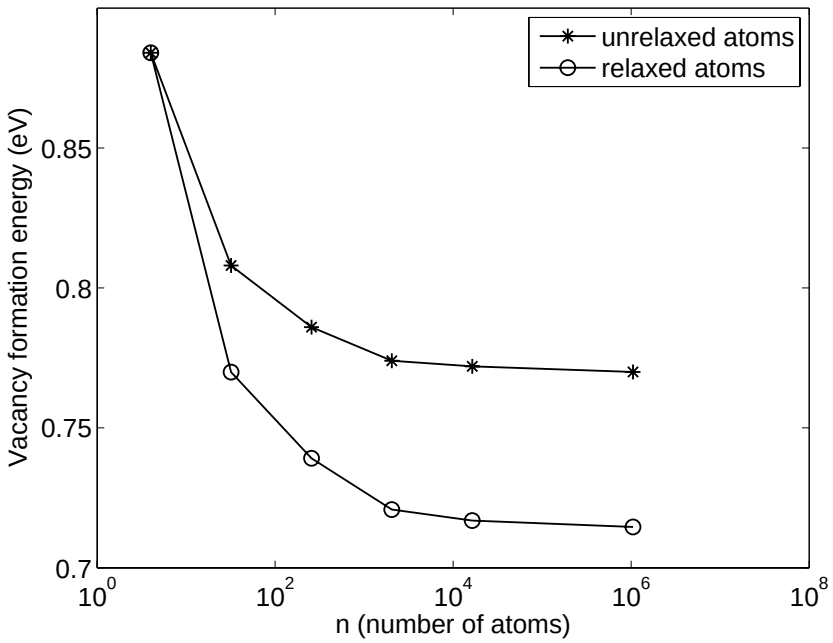

Figure 5.11: Convergence of vacancy formation energy with sample size

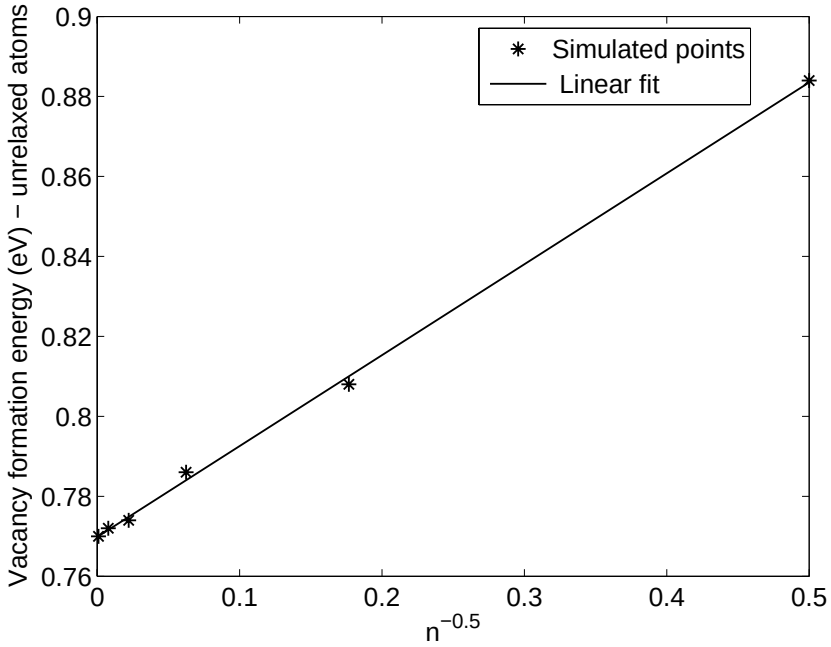

Figure 5.12: Scaling law for vacancy formation energy (unrelaxed atomic positions)

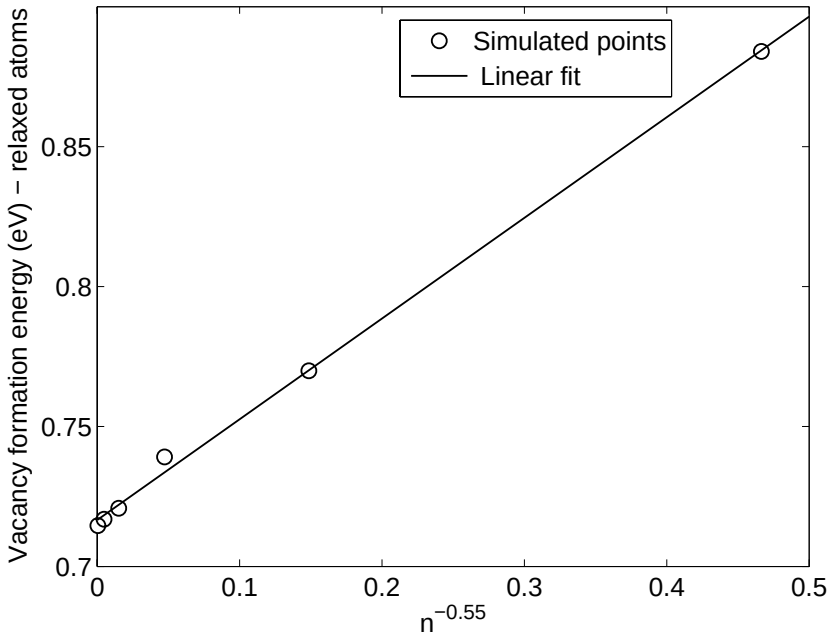

Figure 5.13: Scaling law for vacancy formation energy (relaxed atomic positions)

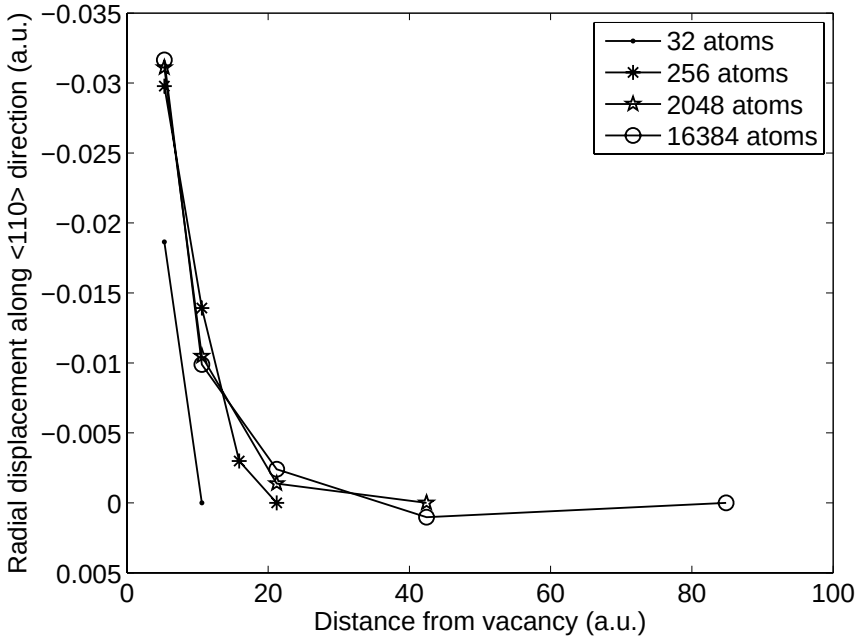

Figure 5.14: Radial displacement of atoms along $\langle 110 \rangle$ direction. The distance from vacancy is listed in atomic units.

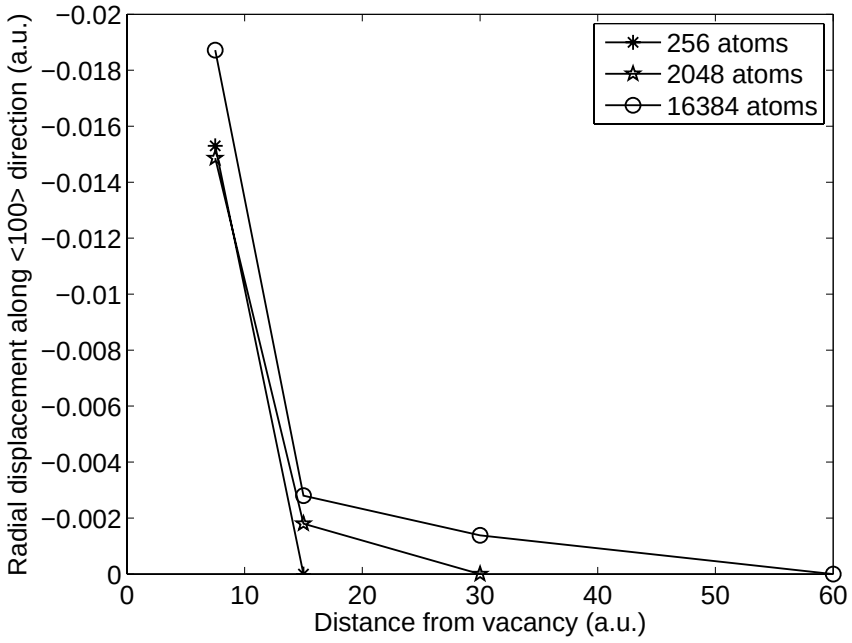

Figure 5.15: Radial displacement of atoms along $\langle 100 \rangle$ direction. The distance from vacancy is listed in atomic units.

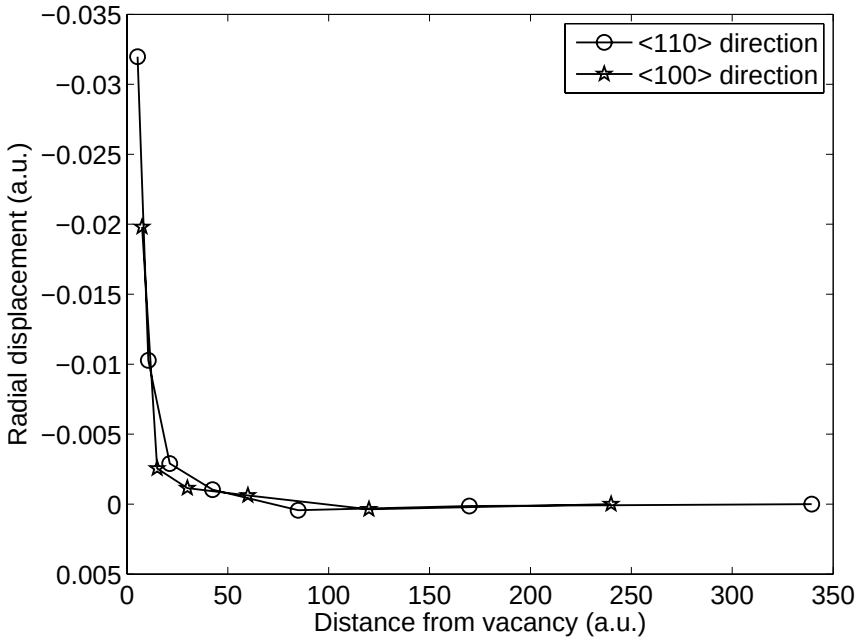

Figure 5.16: Radial displacement of atoms along $\langle 110 \rangle$ and $\langle 100 \rangle$ directions in a million atom sample. The distance from vacancy is listed in atomic units.

Chapter 6

Vacancy clustering in aluminum and nucleation of prismatic dislocation loops

The experimentally determined strength of materials is about one-thousandth their theoretical value. This huge discrepancy is explained by the presence of a high density of dislocations in materials, which is typically around $10^6 - 10^{10}\ cm/cm^3$ (Weertman & Weertman, 1992). Dislocations in materials usually form during the solidification process, but they are also nucleated due to ageing or irradiation. The embrittlement of metals subjected to radiation is a long-standing problem in various applications, including nuclear reactors. As the irradiation dose increases above a certain threshold, a significant population of prismatic dislocation loops (dislocation loops whose Burgers vector has a component normal to their plane) has been experimentally observed to arise in metals (Masters, 1965; Eyre & Bartlett, 1965, 1973; Bullough et al., 1991; Kawanishi & Kuramoto, 1986; Horton & Farrell, 1984). It is of considerable importance to study the mechanism by which these prismatic dislocation loops nucleate as the formation of such defects results in a rapid deterioration of material properties, especially fracture toughness. The embrittlement of metals subjected to radiation is a practical problem assuming significant importance due to renewed interest in nuclear energy.

6.1 Vacancy clustering: An unresolved puzzle

It has been widely believed that vacancy clustering is a mechanism by which prismatic loops are nucleated (Hirth & Lothe, 1968). Specifically, the vacancies diffuse and eventually cluster on specific planes. Once there is a large enough planar cluster, the atoms on the two faces collapse onto each other, leaving behind a prismatic dislocation loop. However, there is no direct experimental observation of this process, and the theoretical investigations are inconclusive. Recent molecular dynamics simulations (Marian et al., 2002) support the hypothesized mechanism for iron, but these calculations were performed using Finnis-Sinclair empirical atomistic potentials whose validity is uncertain in situations requiring breaking and making of atomic bonds (Ackland et al., 1997). However, in contrast, calculations for aluminum using density-functional theory (Carling & Wahnström, 2000; Uesugi et al., 2003) show that di-vacancies—a complex of two vacancies—are either energetically unfavorable if they are aligned along the $\langle 110 \rangle$ direction or barely favorable with negligible binding energy if aligned along $\langle 100 \rangle$. If two vacancies can barely bind, it seems doubtful that they can be stable and grow to form clusters that can turn into prismatic loops. However, on the other hand, experimental interpretations (Ehrhart et al., 1991; Hehenkamp, 1994) suggest a very high binding energy of di-vacancies and also indicate a high concentration of di-vacancies, especially at elevated temperatures. Thus, the question of vacancy clustering being a feasible process and a possible mechanism for prismatic dislocation loop formation has been a point of debate and an unresolved issue.

A challenge in studying defects in solids, and especially vacancies, is their extremely small concentrations. A typical concentration of vacancies in aluminum is a few parts per million (Fluss et al., 1984). Therefore, any realistic calculation of vacancies and their

interaction has to involve millions of atoms. Unfortunately, performing electronic structure calculations with such numbers of atoms remained beyond reach till the recent development of the Quasi-Continuum Orbital-Free Density-Functional Theory (QC-OFDFT) (Gavini et al., 2007) described in Chapter 5. Hence, all previous numerical studies had computed the di-vacancy binding energy in small periodic cells containing less than a hundred atoms. This corresponds to an unphysically high concentration of vacancies, which is rarely—if ever—realized in nature. There exists a possibility that the disagreement of previous numerical calculations with experiments is a result of this unphysically high concentration of defects considered in these calculations.

6.2 Di-vacancy: A QC-OFDFT study

We study di-vacancies in aluminum by performing electronic structure calculations using orbital-free density-functional theory. Specifically, the kinetic energy functional is modelled using the Thomas-Fermi-Weizsacker family of functionals with $\lambda = 1/6$. We use the modified form of Heine-Abarenkov pseudopotential (Goodwin et al., 1990) for aluminum to model the external field created by the nuclei and core electrons. The exchange-correlation effects are treated using a local density approximation (Ceperley & Alder, 1980; Perdew & Zunger, 1981). These kinetic energy, psuedopotential, and exchange-correlation functionals have been shown to correctly predict the bulk properties of aluminum (Gavini et al., 2007), as well as properties of a mono-vacancy (Gavini et al., 2007) as described in Chapters 3 & 5.

A di-vacancy consists of two vacancies at positions $\mathbf{a}_1$ and $\mathbf{a}_2$ within a crystal. We have conducted calculations with a million-atom specimen subjected to Dirichlet boundary conditions representing bulk values as before. The calculations use up to 2001 representative atoms (slightly smaller when the vacancies are close to each other), have 800,000 elements

in the *electronic-mesh* and require 16-18 hours on sixty-four 700 MHz Alpha processors. Figures 6.1 - 6.6 display representative results. Figures 6.1 and 6.2 show the contours of the ground-state electron-density on (100) plane around a di-vacancy complex along $\langle 100 \rangle$ and $\langle 110 \rangle$. Figures 6.3 - 6.6 show the contours of electron-density correction around a di-vacancy complex along $\langle 100 \rangle$ and $\langle 110 \rangle$. It is interesting to note that we observe oscillations in electron-density, which are clearly represented by Figures 6.4 and 6.6. These oscillations in the electron-density are physical, and are counterparts of Friedel oscillations for the Thomas-Fermi-Weizsacker kinetic energy functionals.

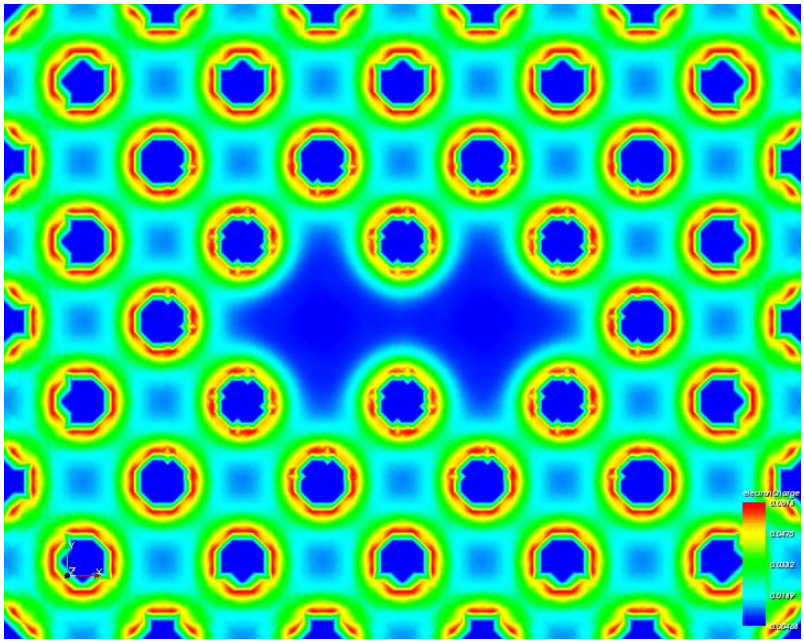

Figure 6.1: Contours of electron-density around a di-vacancy complex along $\langle 100 \rangle$

A property of primary interest in di-vacancy calculations is the di-vacancy binding energy. To understand the nature of this binding energy, we repeat the above calculations for various distances between the vacancies. Let $E_v^f(n)$ denote the mono-vacancy formation energy for a sample consisting of n nominal atoms. Similarly, let $E_{2v}^f(n; \mathbf{a}_1, \mathbf{a}_2)$ denote the di-vacancy

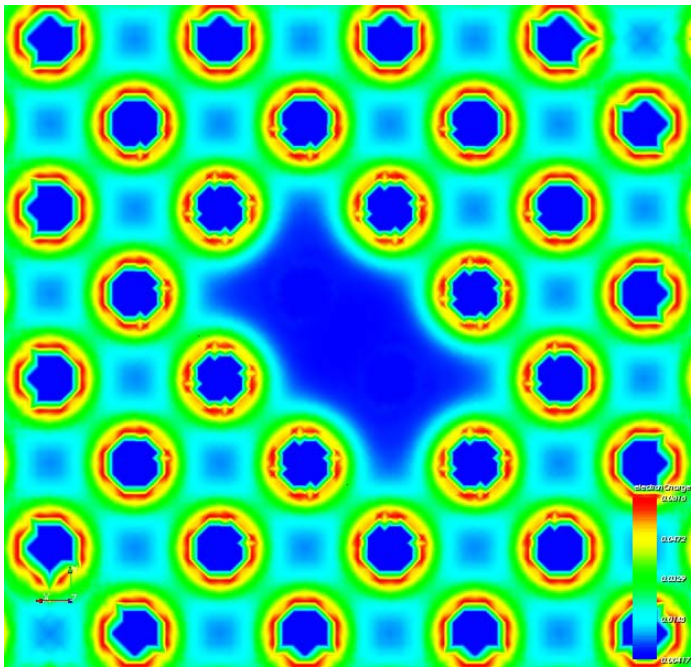

Figure 6.2: Contours of electron-density around a di-vacancy complex along ⟨110⟩

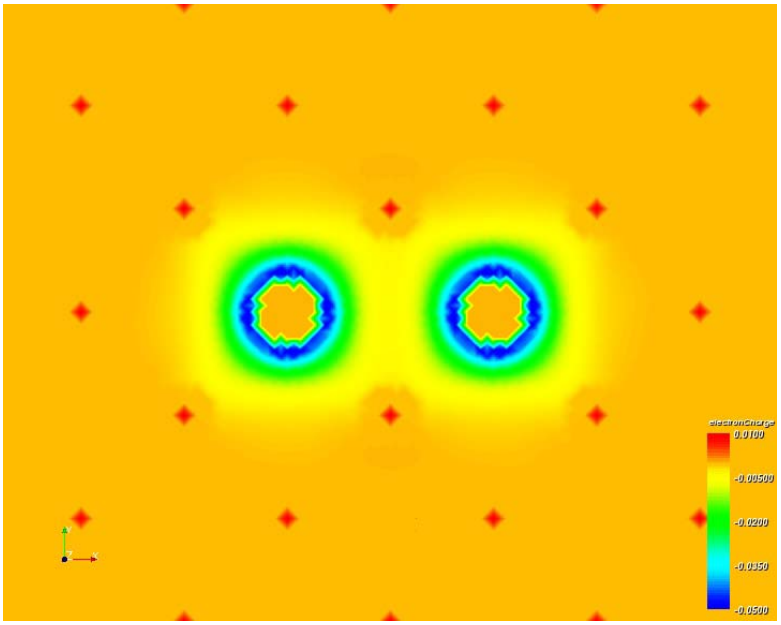

Figure 6.3: Contours of electron-density correction around a di-vacancy complex along ⟨100⟩

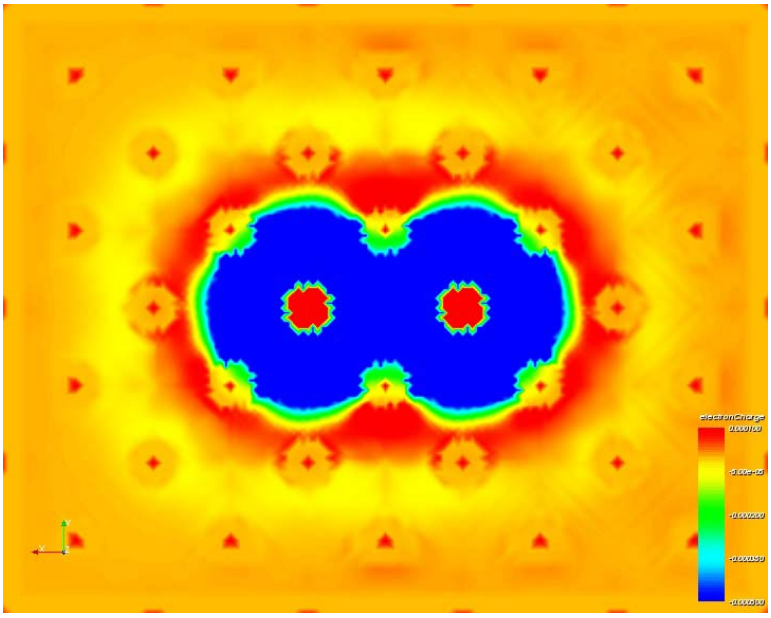

Figure 6.4: Contours of electron-density correction around a di-vacancy complex along ⟨100⟩ (smaller range)

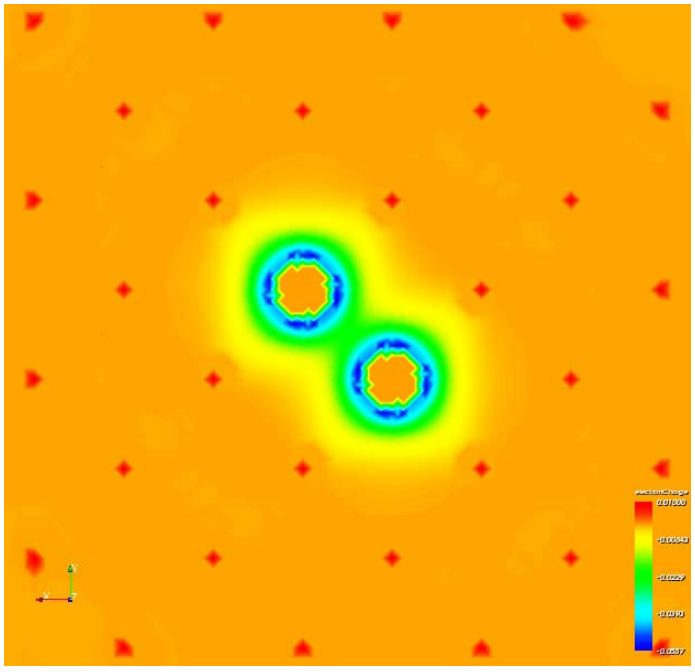

Figure 6.5: Contours of electron-density correction around a di-vacancy complex along ⟨110⟩

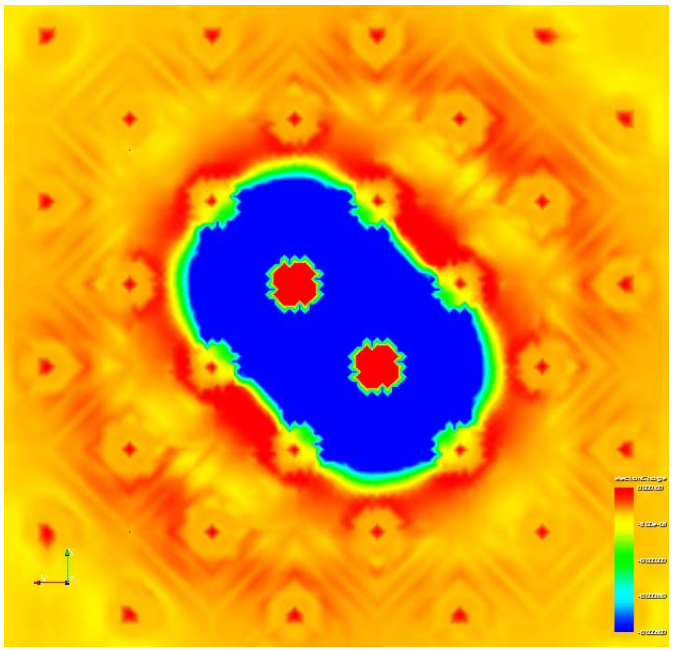

Figure 6.6: Contours of electron-density correction around a di-vacancy complex along ⟨110⟩ (smaller range)

formation energy of a system with two vacancies of sample size n positioned at $\mathbf{a}_1$ and $\mathbf{a}_2$. Then, the di-vacancy binding energy is defined as

$$E_{2v}^{bind}(n;\mathbf{a}_1,\mathbf{a}_2) = E_{2v}^{f}(n;\mathbf{a}_1,\mathbf{a}_2) - 2E_{v}^{f}(n). \tag{6.1}$$

Figure 6.7 shows the unrelaxed binding energy of di-vacancies along the ⟨100⟩ and ⟨110⟩ directions in a million-atom sample over a range of distances between the two vacancies. Figure 6.8 shows the corresponding relaxed energies. These energies are negative, signifying attractive interaction in both cases.

The binding energy for nearest-neighbor vacancies, or *di-vacancy complex*, is calculated to be -0.23 eV in the ⟨100⟩ direction and -0.19 eV in the ⟨110⟩ direction, i. e., *attractive* in both cases. This is in keeping with experimental estimates that place the binding energy of di-vacancy complexes between -0.2 and -0.3 eV (Ehrhart et al., 1991; Hehenkamp, 1994). By

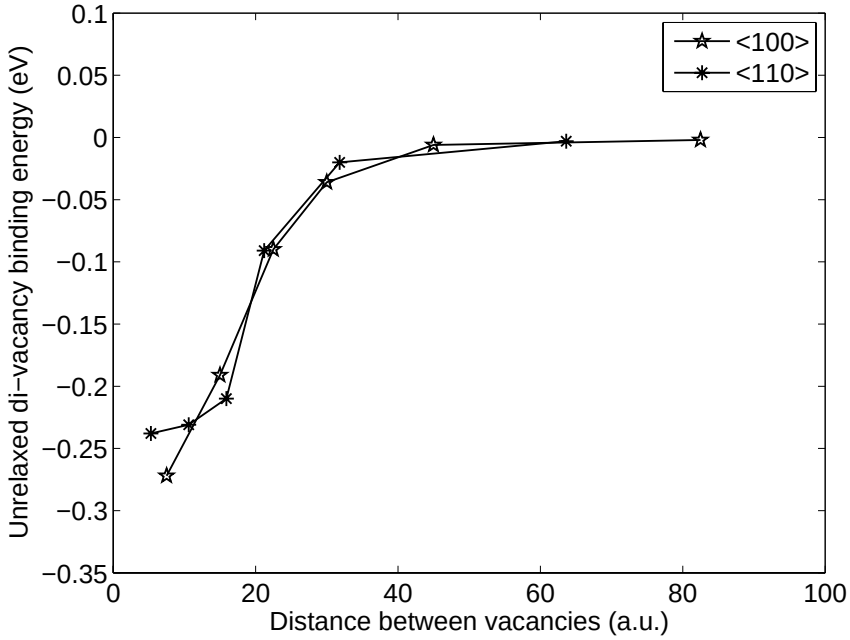

Figure 6.7: Unrelaxed di-vacancy binding energy as a function of the distance between the vacancies

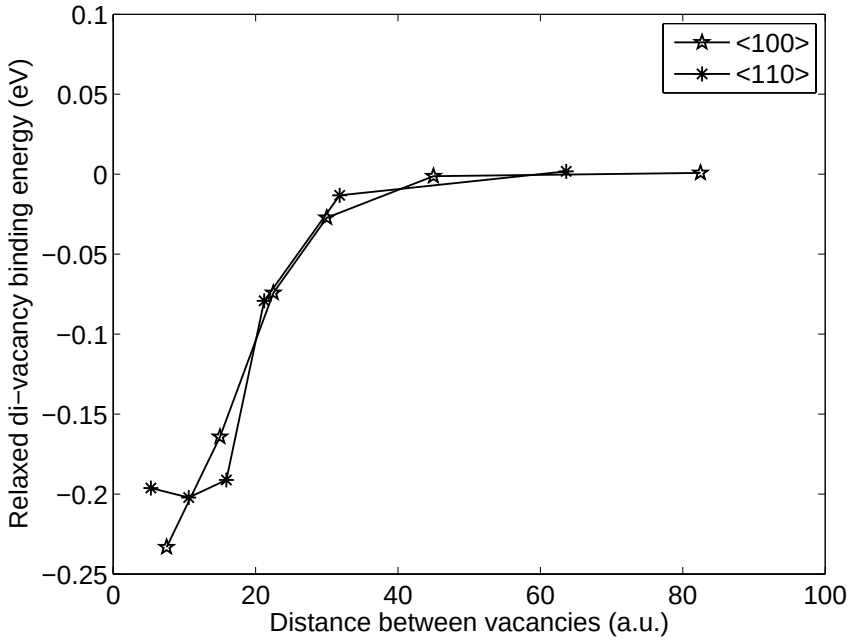

Figure 6.8: Relaxed di-vacancy binding energy as a function of the distance between the vacancies

contrast, recent computations, using periodic cells with less than hundred atoms (Carling & Wahnström, 2000; Uesugi et al., 2003), predict that vacancies repel in the ⟨110⟩ direction with a binding energy of 0.05 eV and attract in the ⟨100⟩ direction with a binding energy of -0.04 eV.

To understand whether these discrepancies are, in effect, a small cell-size effect, we consider samples of sizes n = 4, 32, 256, 2,048, 16,348, and one million atoms. Figure 6.9 shows the effect of cell-size on the binding energies of a di-vacancy complex along ⟨100⟩ and ⟨110⟩. It is observed from these results that there is indeed a strong cell-size effect on the di-vacancy binding energies, especially in the ⟨110⟩ direction. Strikingly, the binding energy changes sign from attractive for large cell-sizes to repulsive for small cell-sizes. This suggests that the repulsive binding energies computed in (Carling & Wahnström, 2000; Uesugi et al., 2003) are characteristic of small cell-sizes, and that in order to make contact with experimental measurements such as reported in (Ehrhart et al., 1991; Hehenkamp, 1994) much larger cell-sizes need to be analyzed.

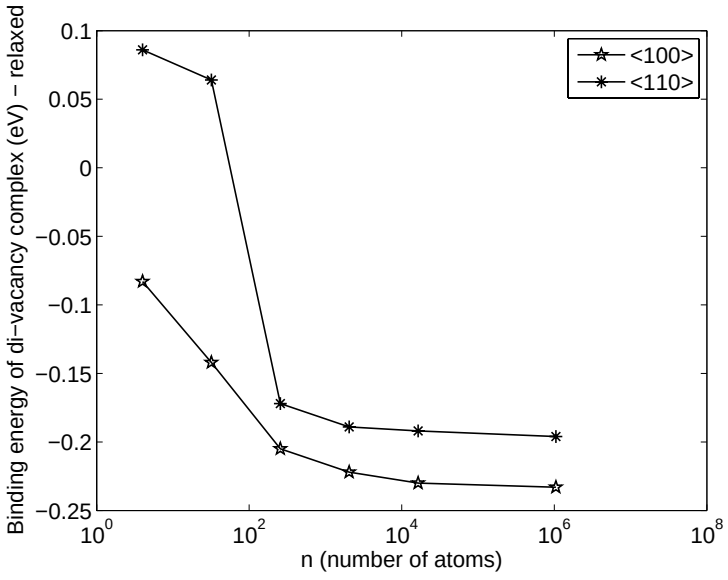

Figure 6.9: Binding energy of a di-vacancy complex(relaxed) as a function of cell-size

6.3 Vacancy clustering and prismatic dislocation loop nucleation

The QC-OFDFT calculations on di-vacancies in aluminum, presented in Section 6.2, are in agreement with experimental observations. Importantly, they indicate a strong cell-size (concentration) effect. Specifically, we found that $\langle 110 \rangle$ di-vacancies were repulsive for small cell-sizes, in agreement with previous calculations (Carling & Wahnström, 2000; Uesugi et al., 2003), and the same di-vacancies were attractive for larger cell-sizes corresponding to realistic concentrations, with binding energies of -0.19 eV in agreement with experimental measurements (Ehrhart et al., 1991; Hehenkamp, 1994). These results showed that electronic structure calculations do not rule out vacancy clustering in aluminum. Therefore, we examine this mechanism further.

We begin by examining the binding energies of various quad-vacancies formed from a pair of di-vacancies. The number of possible quad-vacancies that may be formed from a pair of di-vacancies is very large. Thus we restrict our analysis to configurations such that each vacancy has at least two other vacancies as nearest or second-nearest neighbors. We shall justify this choice subsequently. This criterion results in 9 distinct configurations (up to symmetry), 6 of which are planar vacancy clusters and 3 of which are non-planar. These configurations are listed in Table 6.1.

The *vacancy cluster binding energy* of a n-vacancy cluster is defined as

$$E_{nv}^{bind} = E_{nv}^{f} - nE_{v}^{f} \, ,$$

where E_{v}^{f} denotes the formation energy of a single vacancy and E_{nv}^{f} the formation energy of the n-vacancy cluster. In the convention adopted here, negative value for binding energy

Table 6.1: Vacancy binding energies for quad-vacancies formed from a pair of di-vacancies. All possible quad-vacancies such that each vacancy has two other vacancies as nearest or second nearest neighbors are considered. This table lists the structure of the quad-vacancy, the positions of the vacancies in terms of the lattice parameter and their corresponding vacancy binding energies.

	Structure	Positions of vacancies	Vacancy binding energy (eV)
1	planar {100}	(0,0,0), (a/2,a/2,0), (a,0,0), (a/2,-a/2,0)	-0.52
2	planar {100}	(0,0,0), (a/2,a/2,0), (a,0,0), (3a/2,a/2,0)	-0.50
3	planar {100}	(0,0,0), (a/2,a/2,0), (a,0,0), (a,a,0)	-0.48
4	planar {100}	(0,0,0), (a,0,0), (0,a,0), (a,a,0)	-0.48
5	planar {110}	(0,0,0), (0,a/2,a/2), (a,0,0), (a,a/2,a/2)	-0.56
6	planar {111}	(0,0,0), (0,a/2,a/2), (a/2,a/2,0), (a/2,a,a/2)	-0.55
7	non-planar	(0,0,0), (0,a/2,a/2), (a/2,0,a/2), (a/2,a/2,0)	-0.53
8	non-planar	(0,0,0), (a,0,0), (a/2,a/2,0), (a/2,0,a/2)	-0.51
9	non-planar	(0,0,0), (a,0,0), (a/2,a/2,0), (0,a/2,a/2)	-0.50

denotes attraction among vacancies and a positive value denotes repulsion. The vacancy cluster binding energies for the 9 configurations of quad-vacancies are given in Table 1. Figure 6.10 shows the contours of electron-density for the quad-vacancy cluster with the highest binding energy. This corresponds to configuration No. 5 in Table 6.1, which denotes a planar quad-vacancy on (110) plane. Binding energies of each of these vacancy clusters listed in Table 6.1 are computed using a computational cell consisting of a million atoms. This corresponds to realistic vacancy concentrations of a few parts per million (Fluss et al., 1984). The boundary conditions for all simulations are chosen such that the electronic fields decay to bulk values on the boundaries of the sample. Numerical parameters were chosen to keep the error in the formation energy due to discretization and coarse-graining less than 0.01 eV.

It is interesting to observe that all the quad-vacancies considered have negative binding energies, thus indicating that all these quad-vacancies formed from mono-vacancies are energetically favorable. Further, they also have binding energies larger (in absolute value)

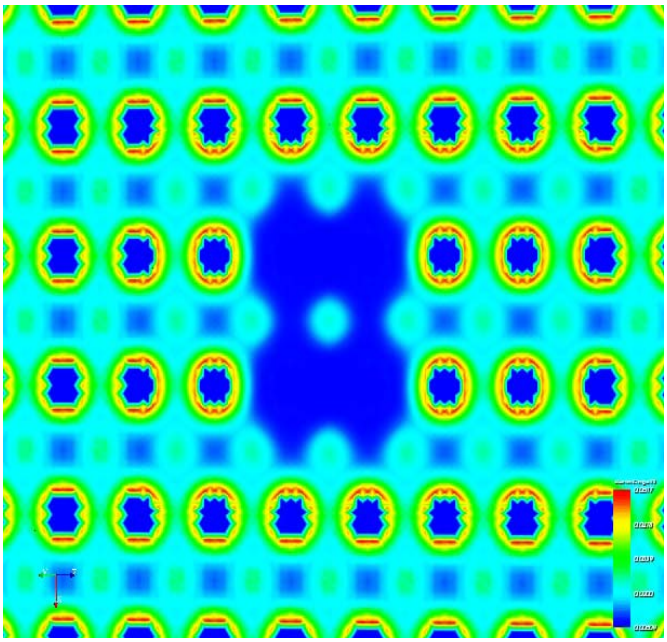

Figure 6.10: Contours of electron-density around a planar quad-vacancy (Configuration No. 5 in Table 6.1) on (110) plane in a million atom sample. This planar quad-vacancy has the highest binding energy among the various quad-vacancies considered.

than twice the computed di-vacancy binding energy of -0.19 and -0.23 eV for $< 110 >$ and $< 100 >$ di-vacancies respectively. This indicates that pairs of di-vacancies are attractive in all cases, and the quad-vacancies formed from a pair of di-vacancies are energetically favorable too. These results suggest that quad-vacancy formation is an energetically feasible process and that vacancies prefer to condense rather than split into mono- or di-vacancies. This observation also justifies our restriction to 9 quad-vacancy configurations.

The cell-size used to simulate defects effectively sets the concentration of the defects. To understand the effect of vacancy concentration on the feasibility of vacancy clustering, we study the cell-size effect on quad-vacancy binding energy for the first configuration in Table 6.1. This configuration represents a square shaped quad-vacancy on (100) plane, whose electronic structure is shown in Figure 6.11. Figure 6.12 shows a strong dependence of the vacancy binding energy on the cell-size. The quad-vacancy which is energetically favorable

for large cell-sizes becomes unstable for small cell-sizes. Thus the predicted physics changes not only quantitatively but also qualitatively with cell-size. This cell-size dependence shows that vacancy clustering which is feasible at low and realistic vacancy concentrations becomes unfavorable at high concentrations. Hence, in order to make contact with realistic material behavior it is necessary to use cell-sizes on the order of millions of atoms.

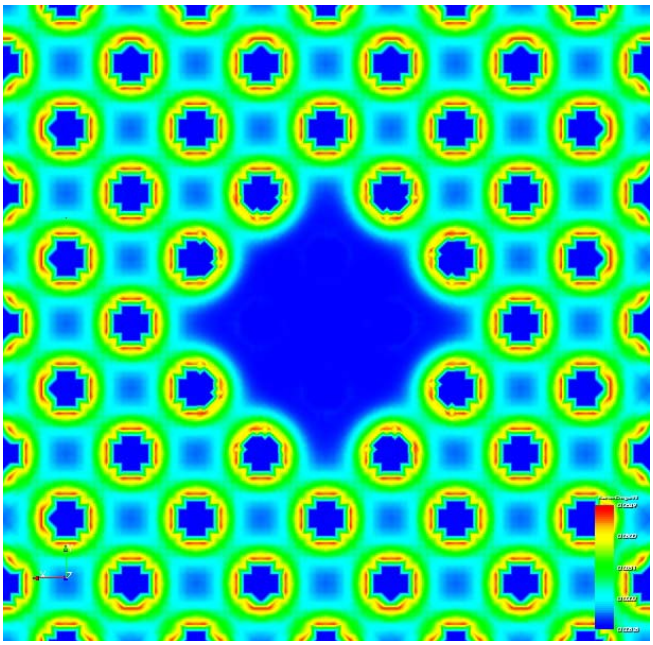

Figure 6.11: Contours of electron-density around a planar quad-vacancy (Configuration No. 1 in Table 6.1) on (100) plane in a million atom sample.

The results in Table 6.1 also show that the configurations with the highest binding energy (No. 5 and 6) are planar quad-vacancy clusters on {110} and {111} planes. Therefore, we performed simulations on larger vacancy clusters on {110} and {111} planes, again using cell-sizes with a million atoms. On the (111) plane, we studied a hexagonal cluster with 7 vacancies, and found two stable configurations. One of the stable configurations is a non-collapsed state with a vacancy cluster binding energy of -0.88 eV, with a maximum

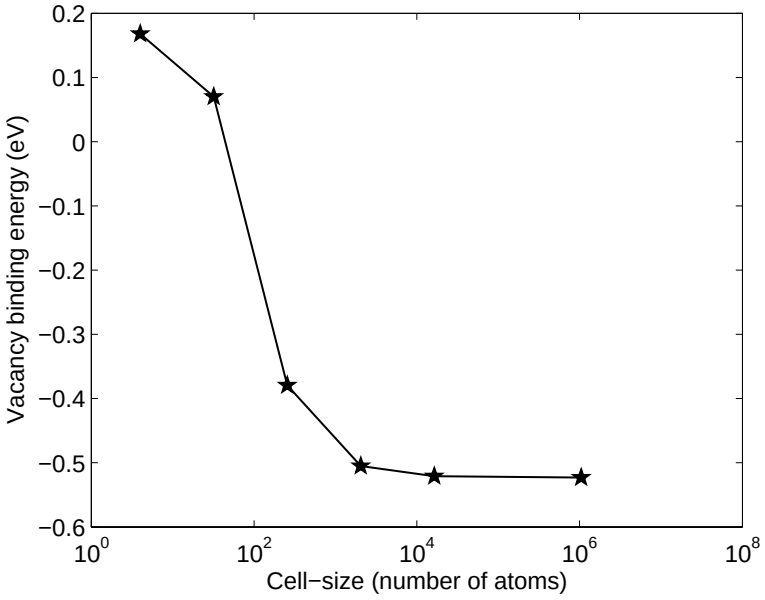

Figure 6.12: Cell-size dependence of vacancy binding energy for the quad-vacancy given by the first configuration in Table 6.1.

displacement of atoms on the order of 3.2% of the nearest-neighbor distance. Note that this is larger (in absolute value) than 7/2 times the di-vacancy binding energy (-0.19 or -0.23 eV depending on orientation). This means that the hexagonal cluster is stable against dissociation into di-vacancies.

The second configuration is a prismatic loop where the atoms above and below the hexagonal vacancy disc collapse or move towards each other, leaving a dislocation line at the boundary of the disc. Figures 6.13 and 6.14 show the atomic positions and the contours of the electron-density on (001) and (111) planes of the collapsed prismatic loop. In particular, the dotted lines in Figure 6.13 depict the collapse of the planes resulting in the prismatic dislocation loop. The maximum displacement of atoms is around 44% of the nearest neighbor distance, the Burgers vector is 0.44[110], and the dislocation plane is (111). These results are consistent with experiments (Kuhlmann-Wilsdorf & Wilsdorf, 1960; Takamura & Greenfield, 1961). Using transmission electron microscope (TEM) it was observed that

prismatic loops form predominantly on a {111} plane with a $1/2\langle 110\rangle$ Burgers vector. Further, in these experiments, prismatic loops whose size is as small as 50 $\mathring{A}$ in diameter were observed. While these are larger than our hexagonal prismatic loop formed from 7 vacancies, it is impossible to detect a loop as it nucleates. Thus, the nucleation size of a prismatic loops was hitherto unknown. The computed vacancy cluster binding energy for the prismatic loop is -1.55 eV which means that not only is this structure stable against dissociation of di-vacancies, but that it is even more stable than the uncollapsed configuration.

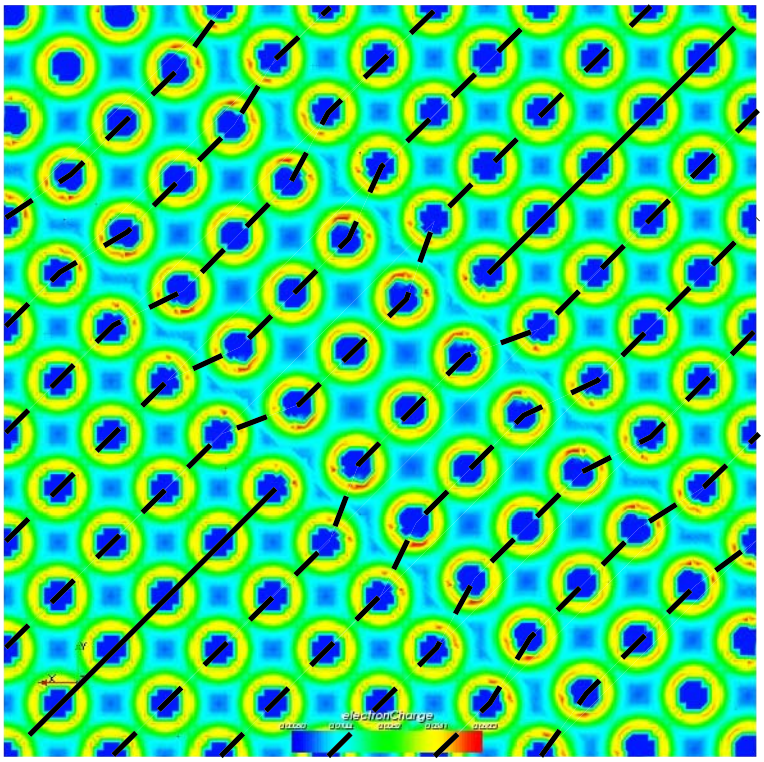

Figure 6.13: Contours of electron-density on the (001) plane around a collapsed vacancy prismatic loop with 0.44[110] Burgers vector and (111) habit plane. This prismatic loop is formed by the collapse of a hexagonal vacancy cluster with 7 vacancies on the (111) plane. The dotted lines represent the collapse of the adjacent planes around the vacancy cluster, thus forming the prismatic dislocation loop.

On the (110) plane, we studied rectangular vacancy clusters with 6 and 9 vacancies. The

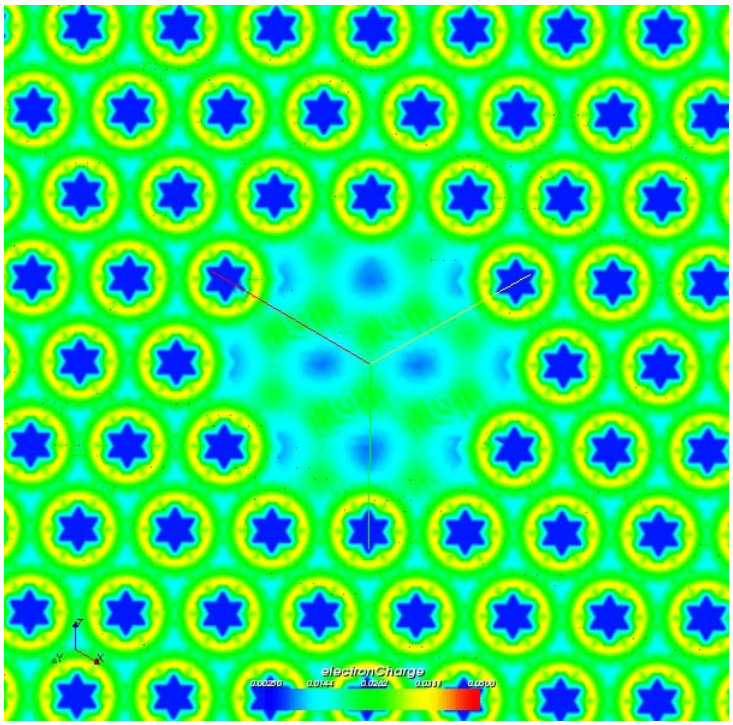

Figure 6.14: Contours of electron-density around the prismatic loop on (111) plane

computed binding energies for these vacancy clusters are -0.81 eV and -1.16 eV respectively. The maximum displacement of atoms in these vacancy clusters is around 4% of the nearest-neighbor distance. These clusters did not display any bi-stability, and collapse to prismatic loops.

These results point to four important facts:

- Firstly, the binding energy of vacancy clusters on {110} and {111} planes in aluminum increases with the size of the vacancy cluster. Also, considering mono-vacancies and di-vacancies as fundamental building blocks, these vacancy clusters are all stable, i.e., vacancies prefer to condense rather than split into mono- or di-vacancies. To the best of our knowledge, this is the first numerical confirmation from an electronic structure perspective that vacancy clustering is energetically favorable.

- Secondly, we observe from direct numerical simulation that the hexagonal vacancy cluster on (111) plane collapses to form a prismatic loop. This establishes from electronic structure calculations that vacancy clustering and collapse of the planes surrounding the vacancy cluster is a possible mechanism for the nucleation of prismatic dislocation loops.

- Thirdly, our results point to the fact that vacancy clusters as small as 7 vacancies can collapse to form stable prismatic loops on {111} planes.

- Finally, our results show the importance of studying defects in solids at realistic concentrations.

Chapter 7

Concluding remarks and future directions

7.1 Summary

The present thesis developed a method, *Quasi-Continuum Orbital-Free Density-Functional Theory* (QC-OFDFT), for systematically and adaptively coarse-graining *Orbital-Free Density-Functional Theory* (OFDFT) in a manner that enables electronic structure calculations of multi-million atom systems at no significant loss of accuracy and without the introduction of spurious physics or assumptions, such as linear response theory or the Cauchy-Born hypothesis. The method is seamless, i. e., OFDFT provides the sole input of the method and does not resort to any form of transition to—or embeddings within—simpler theories, such as empirical potentials or tight-binding models. Because finite element bases are used to describe all fields, no restrictions on boundary conditions limit the applicability of the method. In particular, non-periodic boundary conditions and general geometries can be analyzed using the method. The coarse-graining is completely unstructured and can be adapted to the solution, e. g., to provide full atomic resolution in the vicinity of a defect core, and to rapidly coarse-grain elsewhere.

The method is in the spirit of previous "quasi-continuum" (QC) approaches (cf, e. g.,

Tadmor et al. (1996); Knap & Ortiz (2001)) but differs from those earlier works in several notable respects. The conventional quasi-continuum was devised in order to coarse-grain the displacement field of an atomic lattice. By contrast, OFDFT requires the additional representation of the electron-density and electrostatic potential. Also, in the conventional QC formulations to date, the finite-element mesh is always coarser than the atomic lattice, whereas in the present setting the electron-density and electrostatic potential must be resolved on a sub-lattice length-scale. We effect these representations by carefully nesting three distinct finite-element interpolations spanning the sub-lattice and continuum length-scales. The coarsest of these meshes, or *atomic-mesh*, is equivalent to a conventional QC triangulation of *representative atoms* and coarse-grains the displacement field of the atomic lattice. The electronic fields which require subatomic resolution are decomposed into a predictor and a correction. The predictor for electronic fields, which requires subatomic resolution, is computed on the finest of the three meshes, or *fine-mesh*, using local periodic calculations in every element of the *atomic-mesh*. This predictor is known to be accurate in regions away from the defects, where the deformation field is slowly varying (Blanc et al., 2002). Thus, the corrections, which are non-local, are accurately represented by the *electronic-mesh* that has subatomic resolution close to defects and increasingly coarse-grains away from defect cores. The electronic fields are then determined by solving for the non-local corrections in a variational setting. In order to avoid computational complexities of the order of the entire model (*fine-mesh*), we exploit the conceptual framework of the theory of homogenization of periodic media to define quadrature rules of a complexity commensurate with that of the *electronic-mesh*.

The convergence of finite element approximations in OFDFT has been rigorously proven using the mathematical technique of $\Gamma-$convergence. Also, the convergence of QC-OFDFT,

with increasing number of representative atoms, is demonstrated by means of numerical tests. These tests show that the reduction in computational effort afforded by QC-OFDFT, at no essential loss of accuracy with respect to a full-atom calculation, is quite staggering. For instance, we have analyzed million-atom samples with modest computational resources, giving us access to cell-sizes (computational domain) never before analyzed using OFDFT.

The examples presented in this thesis showcase the importance of having access to such large cell-sizes. For instance, the mono-vacancy calculations in aluminum have determined scaling relations that are indicative of slow convergence with respect to cell size. This is significant for two reasons. First, it shows that long-range interactions beyond those considered in previous calculations (Wang et al., 1998, 1999; Gillian, 1989; Mehl & Klein, 1991; Chetty et al., 1995; Turner et al., 1997) are important. Second, it shows that errors previously attributed to the approximations of OFDFT may in fact be an artifact of small periodic computational cells. These issues are further highlighted by the di-vacancy calculations. We find that the vacancies are attractive along both the $\langle 100 \rangle$ and the $\langle 110 \rangle$ directions. Further, the binding energies we compute are in close agreement with those inferred from experimental observations. However, these results differ from recent calculations (Carling & Wahnström, 2000; Uesugi et al., 2003) which predict that vacancies repel along $\langle 110 \rangle$ direction. To understand this, we compute the di-vacancy interaction for various cell-sizes: We find that the interaction changes sign from attractive for physically realistic sizes to repulsive for unphysically small sizes. This demonstrates that unphysically small computations can lead to spurious results, and thus highlights the potential of the present method.

Finally, we demonstrated the physical insights that QC-OFDFT provides into materials behavior by studying the problem of vacancy clustering and prismatic dislocation loop nucleation in aluminum. We demonstrated, using large cell-sizes ($\sim 10^6$ atoms) describing

a physically realistic vacancy concentration, that vacancy clustering is an energetically favorable process. To the best of our knowledge, this is the first numerical confirmation from an electronic structure perspective that vacancies prefer to condense. We also observe from direct numerical simulations that vacancy clusters collapse to form stable prismatic dislocation loops. This establishes vacancy clustering and collapse of these clusters as a possible mechanism for prismatic dislocation loop nucleation. Also, we found prismatic loops as small as those formed from 7-vacancy clusters are stable. This sheds light on the nucleation size of these defects, which was hitherto unknown.

7.2 Discussion

The proposed multi-scale scheme, QC-OFDFT, which seamlessly transitions from a sub-atomic length-scale (describing the electronic structure of core of the defects) to a continuum length-scale (describing the elastic and electrostatic effects through the electronic structure at the macroscopic scale) has been built around the key-idea of *unstructured coarse-graining* of basis functions. An appropriate formulation and a suitable choice of basis functions – free of any structure – is required to realize this coarse-graining. The combination of a variational real-space formulation, and the choice of a finite-element basis, which confers a local structure to the formulation and is amenable to coarse-graining, are the key ingredients that are used to effect the unstructured coarse-graining. It is important to note that this is a significant departure from the existing implementations of electronic structure calculations using a plane-wave basis, which are not amenable to coarse-graining. Also an added advantage of a real-space finite-element formulation over a reciprocal-space plane-wave formulation, is the freedom to consider general complex domains with arbitrary boundary conditions and the ease of parallel implementation.

The computational complexity associated with electronic structure calculations has limited these calculations to small systems on the order of utmost a few thousands of atoms. However, most problems of interest, especially defects in materials, exhibit features on varying length-scales. The philosophy adopted thus far by most multi-scale schemes (Choly et al., 2005; Lu et al., 2006; Govind et al., 1999) in describing these multi-scale problems is to embed a more accurate and computationally expensive electronic structure calculation inside a coarse continuum theory. Specifically speaking of defects, the region around the defect ($\sim$ 200 atoms) is described by electronic structure calculations, which is embedded in a larger domain described by empirical potentials, which is further embedded in the continuum described by field-theories. Thus, these multi-scale schemes describe the physics on different length scales with disparate theories, and in effect introduce undesirable overlaps between regions of the model governed by heterogeneous and mathematically unrelated theories. Also, there is no clear notion of convergence. Another popular philosophy is to transfer the information across scales using upscaling methods (Rappe' et al., 1992; Goddard et al., 2002). In such methods, electronic structure calculations are used to fit interatomic potentials or force fields. These potentials are in turn used to compute materials properties on macroscopic scales. However, in such upscaling methods, vital information is lost as it is transferred to larger scales. Such schemes assume a clear separation of scales, the validity of which is difficult to verify.

The proposed multi-scale scheme, described by QC-OFDFT, adopts an altogether different philosophy. The whole domain of analysis is described by a single electronic structure theory (OFDFT in this case), and the rest is approximation theory effected using a novel quasi-continuum reduction of the resulting equations. The method is seamless, completely unstructured, and does not introduce any *ad hoc* assumptions or spurious physics. Im-

portantly, convergence of the quasi-continuum approximation is easily analyzed through numerical studies, which show that the reduction in the computational effort afforded by QC-OFDFT, at no significant loss of accuracy with respect to a full electronic structure calculation, is quite staggering. Hence, the present work has opened a new avenue in the field of computational materials science, where an accurate study of defects in materials is possible through electronic structure calculations at macroscopic scales – a feat heretofore not possible.

7.3 Future Directions

The work presented in this thesis opens up the possibility of studying a large range of defects using electronic structure theories, which include void formation, dislocation nucleation, surface reconstructions, phase transitions and stability of nano-structures. It also leaves a number of challenges and scope for future work.

- ***A posteriori mesh adaption***: There is scope to improve the QC-OFDFT method by introducing an *a posteriori* mesh adaption into this scheme, which is necessary to address issues like dislocation nucleation and emission, surface reconstructions, crack propagation in materials, and others, where an *a priori* knowledge of the displacement field and region of interest is lacking. A mathematical flavor to this work can include error estimation of the quasi-continuum approximation, which is by far an open issue and an important research problem.

- ***Evaluation of OFDFT functionals***: The present method applies quite generally regardless of the choice of OFDFT flavor, such as the particular choice of pseudopotential, kinetic energy functional, generalized approximations, and others. The par-

ticular choices made in the calculations presented here are mainly for purposes of illustration. A considerable investment has been made, which continues at present, concerning the development of versions of OFDFT that are increasingly accurate. The accuracy of the various flavors of OFDFT are evaluated using benchmark results from experiments, which include bulk properties like cohesive energies, elastic constants, crystallographic properties, as well as defect properties (vacancy formation energies, surface energies, etc.). Though bulk properties can be accurately computed using the existing plane-wave implementations of OFDFT, an accurate calculation of defect properties is beyond their reach. However, the present QC-OFDFT scheme, which can accurately capture bulk as well as defect properties, can be used to evaluate the accuracy of these various flavors of OFDFT. Such a study will have an important practical significance.

- ***Development of QC-KS-DFT***: Although OFDFT is computationally more tractable and less complex than the Kohn-Sham version of density-functional theory (KS-DFT, cf Chapter 2), its applicability is limited to metallic systems, whereas KS-DFT is widely accepted as the most reliable and computationally feasible tool to model materials. Also, OFDFT provides insights only into the structural properties of materials. The development of sophisticated active materials like ferroelectrics and a growing interest in understanding and modelling these materials, calls for the use of KS-DFT as the fundamental theory for modelling. Thus, the more important research direction lies along the lines of developing a multi-scale model, QC-KS-DFT, with similar features as QC-OFDFT but with KS-DFT as the input physics. Though the adaptive real-space character of QC-OFDFT should prove useful in this endeavor, it requires the computation of eigenvalues and eigenfunctions of large systems. Understanding

the behavior of the eigenvalues and eigenfunctions in the thermodynamic limit of a system with periodic potential will be a useful first step in this direction. Another aspect of such a study, which will be useful in constructing an effective multi-scale scheme with KS-DFT, is to understand how the eigenvalues and eigenfunctions change with local perturbations.

Appendix A

Kernel energies

In this appendix, we discuss briefly, how the variational real-space formulation of OFDFT discussed in Chapter 3 can be extended to the family of kinetic energy functionals with kernel energies. The functional form of kernel energies is given by

$$T_k(u) = \int\int f(u(\mathbf{r}))K(|\mathbf{r} - \mathbf{r}^{'}|)g(u(\mathbf{r}^{'}))d\mathbf{r}d\mathbf{r}' \,.$$

Different types of kernel energies differ through the functional forms of f and g. However, most of them have same functional forms for f and g. To keep the analysis simple we consider the case when f and g have the same functional form. Thus, the kernel energy can be written as,

$$T_k(u) = \int\int f(u(\mathbf{r}))K(|\mathbf{r} - \mathbf{r}^{'}|)f(u(\mathbf{r}^{'}))d\mathbf{r}d\mathbf{r}^{'} \,.$$

Choly & Kaxiras (2002) propose a real space approach to evaluate these integral by approximating the kernel in the reciprocal space by a rational function. Under this approximation,

the kernel energy has a local form, given by,

$$T_k(u) = \sum_{j=1}^{m} \frac{1}{2C_j} Z_j(u) + (\sum_{j=1}^{m} P_j) \int_\Omega f(u)^2 d\mathbf{r} \quad \text{(A.1a)}$$

$$Z_j(u) = \inf_{w_j \in H_0^1(\Omega)} \frac{C}{2} \int_\Omega |\nabla w_j|^2 d\Omega + \frac{Q_j}{2} \int_\Omega w_j^2 d\Omega + C_j \int_\Omega w_j f(u) d\Omega \quad j = 1, ...m \quad \text{(A.1b)}$$

where, C is a positive constant, C_j, Q_j are constants determined from a fitted rational function with degree $2m$. The minimization in (A.1) is well defined if $\frac{C}{C_\Omega} + Q_j > 0$, where C_Ω is the constant from Poincaré inequality. This can be easily verified using Poincaré inequality and Lax-Milgram Lemma.

The common functional form of f used in the kernel energy is $f = u^{2\alpha}$. For this functional form its easy to verify, following the same recipe used to treat the electrostatic interaction energy from Sections 4.1, 4.2 & 4.3, that all the previous mentioned results hold if $\alpha < 2$. Other functional forms of f must be treated on a more specific level.

Bibliography

Ackland, G. J., Bacon, D. J., Calder, A. F., Harry, T., 1997. Computer simulation of point defect properties in dilute Fe-Cu alloy using a many-body interatomic potential. Philos. Mag. A 75, 713.

Ahlrichs, R., Elliot, S.D., 1999. Clusters of aluminum, a density functional study. Phys. Chem. Chem. Phys. 1, 13.

Bey, J., 2000. Simplicial grid refinement: on Freudenthal's algorithm and the optimal number of congruence classes. Numer. Math. 85, 1.

Blanc, X., Le Bris, C., Lions, P.L., 2002. From molecular models to continuum mechanics. Arch. Rational Mech. Anal. 164, 341.

Bowler, D.R., Choudhury, R., Gillan, M.J., Miyazaki, T., 2006. Recent progress with large-scale ab initio calculations: the CONQUEST code. Physica Status Solidi B 243, 989.

Braides, A., 2002. Γ-convergence for beginners, Oxford University Press, New York.

Brenner, S.C., Scott, L.R., 2002. The mathematical theory of finite element methods, Springer-Verlag, New York.

Brewer, L., 1977. Lawrence Berkeley labaratory report No. 3720 (unpublished)

Bullough, T. J., English, C. A., Eyre, B. L., 1991. Low-energy heavy-ion irradiations of copper and molybdenum at low-temperatures. Proc. R. Soc. London A 435, 85.

Cade, P.E., Sales, K.D., Wahl, A.C., 1973. Electronic structure of diatomic molecules. III.A. Hartree-Fock wave functions and energy quantities for N_2 and N_2^+ molecular ions. J. Chem. Phys. 44, 1973.

Carling, K., Wahnström, G., 2000. Vacancies in metals: From first-principles calculations to experimental data. Phys. Rev. Lett. 85, 3862.

Ceperley, D.M., Alder, B.J., 1980. Ground state of the electron gas by a stochastic method. Phys. Rev. 45, 566.

Ciarlet, P.G., 2002. The finite element method for elliptic problems, SIAM, Philadelphia.

Clementi, E., Roothaan, C.C.J., Yoshimine, M., 1962. Accurate analytical self-consistent field functions for atoms. II. Lowest configurations of neutral first row atoms. Phys. Rev. 127, 1618.

Chetty, N., Weinert, M., Rahman, T.S., Davenport, J.W., 1995. Vacancies and impurities in aluminum and magnesium. Phys. Rev. B 52, 6313.

Choly, N., Kaxiras, E., 2002, Kinetic energy density functionals for non-periodic systems. Solid State Comm. 121, 281.

Choly, N., Lu, G., E., W., Kaxiras, E., 2005. Multiscale simulations in simple metals: A density-functional-based methodology. Phys. Rev. B 71, 094101.

Gianni Dal Maso, 1993. An introduction to Γ-convergence, Birkhäuser, Boston.

De Giorgi, E., Franzoni, T., 1975. Su un tipo di convergenza variazionale. Atti Acad. Naz. Linccei Rend. Cl. Sci. Mat. 58, 842.

Dirac, P. A. M., 1929. Quantum mechanics of many-electron systems. Proc. R. Soc. A. 123, 714.

Ehrhart, P., Jung, P., Schultz, H., Ullmaier, H., 1991. Atomic defects in metal. Landolt-Börnstein, New Series, Group 3, Vol. 25, Springer-Verlag, Berlin 1991.

Eshelby, J.D., 1951. The force on an elastic singularity. Phil. Trans. Royal Soc. Lond. A 244 (877): 87-112.

Eyre, B. L., Bartlett, A. F., 1965. An electron microscope study of neutron irradiation damage in alpha-iron. Philos. Mag. 12, 261.

Eyre, B. L., Bartlett, A. F., 1973. Damage structure formed in molybdenum by irradiation in a fast-reactor at 650 degrees C. J. Nucl. Mater. 47, 143.

Fago, M., Hayes, R.L., Carter, E.A., Ortiz, M., 2004. Density-functional-theory-based local quasicontinuum method: Prediction of dislocation nucleation. Phys. Rev. B 70, 100102(R).

Fermi, E., 1927. Un metodo statistice per la determinazione di alcune proprieta dell'atomo. Rend. Acad. Lincei 6, 602.

Finnis, M., 2003. Interatomic forces in condensed matter, Oxford University Press, New York.

Fluss, M. J., Berko, S., Chakraborthy, B., Hoffmann, K. R., Lippel, P., Siegel, R. W., 1984. Positron annhilation spectroscopy of the equlibrium vacancy ensemble in aluminum. J. Phys. F : Met. Phys. 14, 2831.

Friesecke, G., 2003. The multiconfiguration equations for atoms and molecules: Charge quantization and exisistence of solutions. Arch. Rational Mech. Anal. 169, 35.

Gavini, V., Bhattacharya, K., Ortiz, M., 2007. Quasi-continuum orbital-free density-functional theory: A route to multi-million atom non-periodic DFT calculation. J. Mech. Phys. Solids. in press; published online 21 Feb 2007 (doi:10.1016/j.jmps.2007.01.012).

Gavini, V., Knap, J., Bhattacharya, K., Ortiz, M., 2007. Non-periodic finite-element formulation of orbital-free density-functional thoery. J. Mech. Phys. Solids. in press; published online 28 Nov 2006 (doi:10.1016/j.jmps.2006.09.011).

Gillan, M.J., 1989. Calculation of vacancy formation energy in aluminum. J. Phys., Condens. Mat. 1, 689.

Goddard III, W. A., Zhang, Q., Uludogan, M., Strachan, A., Cagin, T., 2002. The ReaxFF Polarizable Reactive Force Fields for Molecular Dynamics Simulation of Ferroelectrics. Fundamental Physics of Ferroelectrics 2002, 45-55, edited by Cohen, R., E.,.

Goodwin, L., Needs, R.J., Heine, V., 1990. A pseudopotential total energy study of impurity promoted intergranular embrittlement. J. Phys. Condens. Matter 2, 351.

Govind, N., Wang, Y.A., Carter, E.A., 1999. Electronic-structure calculations by first-principles density-based embedding of explicitly correlated systems. J. Chem. Phys. 110, 7677.

Gschneider, K.A., 1964. Solid state physics, New York: Academic vol 16, 276.

Gunnarsson, O., Harris, J., Jones, R.O., 1977. Density functional theory and molecular bonding. I. First-row diatomic molecules. J. Chem. Phys. 67, 3970.

Hirth, J.P., Lothe, J., 1968, Thoery of Dislocations, McGraw-Hill, New York.

Hehenkamp, T., 1994. Absolute vacancy concentrations in nobel metals and some of their alloys. J. Phys. Chem. Solids 55, 907.

Hehre, W.J., Stewart, R.F., Pople J.A., 1969. Self-consistent molecular-orbital methods .I. use of gaussian expansions of slater-type atomic orbitals. J. Chem. Phys. 51, 2657.

Hohenberg, P., Kohn, W., 1964. Inhomogeneous electron gas. Phys. Rev. 136, B864.

Horton L. L., Farrell, K., 1984. The temperature-dependence of the damage microstructures in neutron-irradiated vanadium. J. Nucl. Mater. 122, 687.

Hou, W.M., 1965. Electronic structure of CO and BF. J. Chem. Phys. 43, 624.

Huber, K.P., 1972. Constants of diatomic molecules, in American institute of physics handbook, McGraw-Hill, New York.

Kawanishi, H., Kuramoto, E., 1986.14 MeV neutron-irradiation of vanadium alloy (V-1 atmospheric Percent-B). J. Nucl. Mater. 143, 899.

Knap, J., Ortiz, M., 2001. An analysis of the quasicontinuum method. J. Mech. Phys. Solids 49, 1899.

Koch, W., Holthausen, M.C., A Chemist's guide to denisty functional theory, Wiley-VCH.

Kohn, W., Sham, L.J., 1965. Self-consistent equations including exchange and correlation effects. Phys. Rev. 140, A1133.

Lewin, M., 2004. Solutions of the multiconfiguration equations in quantum chemistry. Arch. Rational Mech. Anal. 171, 83.

Lu, G., Tadmor, E.B., Kaxiras, E., 2006. From electrons to finite elements: A concurrent multiscale approach for metals. Phys. Rev. B 73, 024108.

Marian, J., Wirth, B. D., Perlado, J. M., 2002. Mechanism of formation and growth of ⟨100⟩ interstitial loops in ferritic materials. Phys. Rev. Lett. 88, 255507.

Martin, R., 2004. Electronic structure, basic theory and practical methods, Cambridge University Press, Cambridge.

Masters, B. C., 1965. Dislocation loops in irradiated iron. Philos. Mag. 11, 881.

Mehl, M.J., and Klein, B.M., 1991. All-electron first-principles supercell total-energy calculation of the vacancy formation energy in aluminum. Physica B 172, 211.

Parr, R.G., Yang, W., 1989. Density-functional theory of atoms and molecules, Oxford University Press, New York.

Pask, J.E., Klein, B.M., Fong, C.Y., Sterne, P.A., 1999. Real-space local polynomial basis for solid-state electronic structure calculations: A finite-element approach. Phys. Rev. B 59, 12352.

Perdew, J.P., Zunger, A., 1981. Self-interaction correction to density-functional approximation for many-electron systems. Phys. Rev. B 23, 5048.

Rappe' A. K., Casewit, C. J., Colwell, K. S., Goddard III, W. A., and Skiff, W. M., 1992. UFF, a Rule-Based Full Periodic Table Force Field for Molecular Mechanics and Molecular Dynamics Simulations. J. Am. Chem. Soc, 114, 10024.

Skylaris, C.K., Haynes, P.D., Mostofi, A.A., Payne, M.C., 2005. Linear-scaling density functional simulations on parallel computers. J. Chem. Phys. 122, 084119.

Smargiassi, E., Madden, P.A., 1994. Orbital-free kinetic-energy functionals for first-principle molecular dynamics. Phys. Rev. B 49, 5220.

Soler et al. 2002. The SIESTA method for ab initio order-N materials simulation. J. Phys. Condens. Mat. 14, 2745.

Szabo, A., Ostlund, N.S., 1982. Modern quantum chemistry: Introduction to advanced electronic structure theory, MacMillan Publishing Co., New York.

Tadmor, E.B., Ortiz, M., Phillips, R., 1996. Quasicontinuum analysis of defects in solids. Philos. Mag. A 73, 1529.

Takamura, J., Greenfield, I. G., 1961. Development of prismatic loops in quenched aluminum-0.5%magnesium. J. Appl. Phys. 33, 247.

Thomas, L.H., 1927. The calculation of atomic fields. Proc. Cambridge Phil. Soc. 23, 542.

Thoutireddy, P., 2002. Variational arbitrary Lagrangian-Eulerian method. Caltech Thesis etd-05292003-113845.

Tong, B.Y., Sham, L.J., 1966. Application to a self-consistent scheme including exchange and correlation effects to atoms. Phys. Rev. 144, 1.

Triftshäuser, M., 1975. Positron trapping in solid and liquid metals. Phys. Rev. B 12, 4634.

Turner, D.E., Zu, Z.Z., Chan, C.T., Ho, K.M., Energetics of vacancy and substitutional impurities in aluminum bulk and clusters. Phys. Rev. B 55, 13842.

Uesugi, T., Kohyama, M., Higashi, K., 2003. *Ab initio* study on divacancy binding energies in aluminum and magnesium. Phys. Rev. B 68, 184103.

Wang, L., Teter, M.P., 1992. Kinetic energy functional of electron density. Phys. Rev. B, 45, 13196.

Wang Y.A., Govind, N., Carter, E.A., 1998. Orbital-free kinetic-energy functionals for the nearly free electron gas. Phys. Rev. B 58, 13465.

Wang Y.A., Govind, N., Carter, E.A., 1999. Orbital-free kinetic-energy density functionals with a density-dependent kernel. Phys. Rev. B 60, 16350.

Weertman J., Weertman J. R., 1992. Elementary dislocation theory, Oxford University Press, New York.

Wills, J.M., Cooper, B.R., 1987. Synthesis of band and model hamiltonian theory for hybridizing cerium systems. Phys. Rev. B 36, 3809.

Kuhlmann-Wisdorf, D., Wilsdorf, H. G. F., 1960. On the behavior of thermal vacancies in pure aluminum. J. Appl. Phys. 31, 516.